Measurement of the Associated Production of Z Bosons and Jets in $p\bar{p}$ Collisions at the Tevatron

Dissertation an der Fakultät für Physik
der
Ludwig-Maximilians-Universität München

vorgelegt von

Britta Tiller

geboren in München

München, im Januar 2009

1. Gutachterin:	Prof. Dr. Dorothee Schaile
2. Gutachter:	Prof. Dr. Wolfgang Dünnweber

Tag der mündlichen Prüfung /
date of oral exam: 24.4.2009

Abstract

Higher order QCD corrections to W and Z boson production do not only manifest themselves in the generation of high transverse momenta of the weak bosons, but these QCD effects become directly visible in the production of jets in association with the weak bosons. Studying these processes is not only interesting from the perspective of testing perturbative QCD, but also to constrain a major background to many Standard Model (SM) or non-SM physics signals, e.g. top pair and single top production, searches for the Higgs boson, leptoquarks and supersymmetric particles. This thesis describes a measurement of Z/γ^*+ jets production in $p\bar{p}$ collisions at $\sqrt{s} = 1.96\,\text{TeV}$ in the decay channel $Z/\gamma^* \rightarrow \mu^+\mu^-$. An integrated luminosity of $\mathcal{L} \approx 1\,\text{fb}^{-1}$ collected by the DØ detector at the Tevatron between August 2002 and February 2006 has been used. Differential production cross sections as function of the transverse energy of the first, second and third leading jet are measured. The distributions are corrected for acceptance and migration effects back to hadron level using an iterative unfolding method. Comparisons of the measured cross sections to event generators, which include part of the higher order corrections are presented.

Zusammenfassung

Bei der Produktion von W und Z Bosonen können QCD Korrekturen große Boson Transversalimpulse verursachen. Direkt sichtbar werden diese Effekte bei der Erzeugung von Jets in Assoziation mit den schwach wechselwirkenden Bosonen. Ein Studium dieser Prozesse dient daher einerseits als Test der störungstheoretischen Beschreibung der QCD, hilft aber andererseits auch einen der Hauptuntergründe vieler Signale innerhalb und ausserhalb des Standartmodells abzuschätzen. So ist die assoziierte Produktion von W und Z Bosonen mit Jets ein wichtiger Untergrund bei der Erzeugung von einzelnen Topquarks oder Topquarkpaaren ebenso wie bei Suchen nach dem Higgsboson, Leptoquarks oder supersymmetrischen Teilchen. Diese Arbeit beschreibt die Messung der assoziierten Produktion von Z Bosonen und Jets in $p\bar{p}$ Kollisionen bei einer Schwerpunktsenergie von $\sqrt{s} = 1.96\,\mathrm{TeV}$ im Zerfallskanal $Z/\gamma^* \rightarrow \mu^+\mu^-$. Hierfür wird ein Datensatz mit einer integrierten Luminosität von $\mathcal{L} \approx 1\,\mathrm{fb}^{-1}$ verwendet, welcher im Zeitraum von August 2002 bis Februar 2006 mit dem DØ Detektor am Tevatron aufgezeichnet worden ist. Die differentiellen Wirkungsquerschnitte werden in Abhängigkeit der transversalen Energie der drei höchstenergetischsten Jets gemessen. Eine iterative Entfaltungsmethode wird angewandt, um die Verteilungen auf Akzeptanz und Migrationseffekte zurück auf Hadronniveau zu korrigieren. Die Ergebnisse der Messungen werden mit den Vorhersagen verschiedener Ereignisgeneratoren verglichen, welche Korrekturen höherer Ordnungen einschliessen.

Contents

1 Introduction

Since the discovery of the Z gauge boson at CERN (the European Organization for Nuclear Research) in 1983 [1, 2], the study of the associated production of electroweak gauge bosons with jets has been of increasing importance. The production of Z gauge bosons in association with jets provides a good opportunity to test predictions of pertubartive quantum chromodynamics (pQCD) at large momentum transfers. Furthermore it is also an important physics signal at hadron colliders, such as the Fermilab Tevatron and the Large Hadron Collider (LHC) at CERN. Studying these processes helps to constrain a major background to many Standard Model signals, e.g. top pair and single top production. In addition to that many of the searches for new particles like the Higgs boson or supersymmetric (SUSY) particles involve final states containing one ore more jets in the signature of the final state in addition to charged leptons or neutrinos. The production of the Z boson in association with jets thus has been an important process at hadron colliders not only for the dominant background of the most of precision measurements but also to probe new physics.

This analysis studies dilepton pair production in association with jets. The decay of the Z bosons into pairs of muons and anti-muons provides an efficient way to identify the final state with low background contamination. The measured cross sections corrected for detector and resolution effects are distributions at particle level, which can be compared directly to the predictions of event generators. The measured cross sections are compared to the predictions of event simulations which include some higher order corrections to the leading-order processes.

Chapter 2 of this thesis provides a short overview of the theoretical framework in which this analysis was performed and illustrates the used Monte Carlo (MC) event generators. A description of the experimental apparatus including the Fermilab accelerator chain and the DØ detector is given in Chapter 3. The event reconstruction and data selection including comparisons between data and event simulation is described in Chapter 4. Chapter 5 outlines the measurement of the $Z/\gamma^* \rightarrow \mu^+\mu^- +$ jets differential production cross section including sources for systematic uncertainties. A summary of the results is presented in Chapter 6 followed by a conclusion in Chapter 7.

2 Theory

2.1 The Standard Model of particle physics

Four fundamental forces acting between the particles describe the known interactions and processes. These forces are characterized by different ranges, magnitudes and behaviors.
The gravitational force is the weakest force. It acts between massive objects in accordance with the general theory of relativity and is the dominant force throughout the universe since the interaction is always attractive. Contrary to the gravitation the electromagnetic force can be attractive or repulsive and is much stronger than gravity. It exerts on electrically charged particles and binds e.g. electrons to atomic nuclei (consisting of protons and neutrons) to form atoms. The electromagnetic force explains electricity and magnetism. The physical theory that describes this force is called electrodynamics. Gravity as well as the electromagnetic force have an infinite range.
The strong force, the strongest of the four fundamental forces, is responsible for the cohesion of particles in the atomic nucleus (quarks stick together to form protons, neutrons and related particles and binds protons and neutrons in the nucleus). It has a very short range of about $10^{-15}\,\mathrm{m}$ (or one Fermi).
The last of the four fundamental forces is the weak force which governs the process of radioactivity, responsible e.g. for the beta decay, with an extremely short range in the order $10^{-18}\,\mathrm{m}$.

The theoretical aspects underlying this thesis can all be described by the Standard Model of particle physics. The Standard Model is a theoretical framework that describes three of the four fundamental interactions between the elementary particles, namely the strong, weak and electromagnetic fundamental forces. The interactions are described by using mediating gauge bosons. Gravity is not included in the Standard Model. Due to its weakness, its contribution can be neglected in particle physics. A detailed description of the Standard Model is given in [7, 8].
In the Standard Model the matter is represented in terms of twelve fundamental

particles with spin 1/2, called fermions. The fermions are the constituents of matter. Each particle is associated with an anti-particle, having the same mass and spin as the particle but carrying opposite charge. The fermions are divided into two groups, quarks (q) and leptons (l). As indicated in Table 2.1, the fermions are arranged in three families or generations, containing particles of similar properties but increasing masses.

The interactions between the fermions are mediated by the exchange of spin 1 particles, called intermediate vector bosons: photon (γ), gluon, $W^{\pm}$ and Z boson. The vector bosons transmit the force between one quark or lepton and another. The photon is the mediator of the electromagnetic force. The strong force is mediated by the gluons and the weak force is mediated by the W^{+}, W^{-} and Z boson.

The particles in the Standard Model are treated as excitations of relativistic quantum fields. The interactions between the fermion and boson fields are introduced through symmetry arguments, known as local gauge invariance. Within the Standard Model the forces can be described in terms of unitary groups of different dimensions, written as

	charge	1.Generation	2.Generation	3.Generation
Quarks	2/3	u	c	t
	-1/3	d	s	b
Leptons	0	ν_e	ν_μ	ν_τ
	-1	e	μ	τ

Table 2.1: The fermions of the Standard Model of elementary particle physics.

$$SU(3)_{Colour} \times SU(2)_L \times U(1)_Y$$

$SU(3)_{Colour}$ denotes the symmetry group of the strong force. The $SU(2)_L \times U(1)_Y$ gauge group describes the unification of electromagnetism and weak interaction into the electroweak force.

The Standard Model predicts also a spin-0 particle which is associated with the electroweak symmetry breaking, the Higgs boson, which has not been discovered yet. Nevertheless a lower limit on the mass of the Higgs boson has been set [9].

2.1.1 The electroweak interaction

In 1967 Glashow, Salam and Weinberg combined the electromagnetic and weak interaction and introduced the theory of the electroweak interaction (GWS theory [3]), which describes the electroweak part of the interaction between bosons and fermions, as well as between the bosons themselves. In this theory the electromagnetic and weak interactions appear as different manifestations of one fundamental electroweak interaction. Mathematically, the unification is accomplished under a $SU(2)_L \times U(1)_Y$ gauge group. $SU(2)_L$ refers to the weak isospin I[1] and $U(1)_Y$ refers to the weak hypercharge Y. The hypercharge Y is the conserved quantity of the $U(1)_Y$ group and is given by a combination of the electric charge Q and the third component of the weak isospin I_3:

$$Y = 2(Q - I_3)$$

The associated bosons of this gauge group are the W^+ and W^-, the W^0 and the B^0 boson. Three of them acquire mass by the *Higgs mechanism* through spontaneous symmetry breaking of the electroweak symmetry into the $U(1)_{em}$ gauge symmetry of the electromagnetic interaction and orthogonal combinations between the W^0 and B^0 lead to the massive Z and the massless photon.

2.1.2 The strong interaction

The strong interaction between quarks (q) and gluons (g) is described by the gauge invariant quantum field theory of quantum chromodynamics (QCD). A detailed description of QCD can be found in [7]. The massless gauge boson of this theory is known as the gluon. The non-abelian gauge theory based on $SU(3)$ has eight generators, which lead to eight types of gluons and to the conservation of 'colour' charge. Gluons and quarks themselves carry colour. They have not been observed as isolated particles, as only colourless particles can form isolated states in nature. Leptons are colourless and do not couple to the strong force.

The strongly interacting particles observed in nature are called hadrons, which can be classified into mesons (quark-antiquark states) and baryons (triplets of quarks) with neutral net colour. The strength of the interaction is parameterized by the strong coupling constant α_s. Due to the self-coupling between gluons this constant is in fact not constant, but depends on the energy scale Q^2 of the event (*running coupling*) and decreases with increasing Q^2 (whereas Q^2 is the absolute squared four-momentum transfer in the collision). This characteristic running of α_s is used to explain the observed behavior of the strong interaction. At very short distances (high momentum transfers) the effective coupling becomes very small, which causes a decoupling of quarks and gluons, which then behave like almost free, noninteracting particles. This phenomena is known as *asymptotic freedom*. At large distances (low energies) the strength of the colour field increases and due to the colour confinement quarks and gluons cannot exist individually but form colour-neutral hadrons, by a process called *hadronization*. Up to now, an explicit calculation of the hadronization

---

[1] The subscript L reminds that the symmetry group involves only left-handed states. Left handed means that spin and velocity of a spin $\frac{1}{2}$ particle are anti-parallel.

is not possible as the involved confinement cannot be described by means of perturbation theory. Instead the process of hadronization is implemented via complex phenomenological models.

2.2 Production of Z bosons at the Tevatron

This thesis focuses on the analysis of Z boson production in association with jets. The production of Z boson in proton-antiproton collisions at the Tevatron is dominated by leading-order quark-antiquark annihilation (the weak Drell-Yan process [10]) in a hard scattering process. This is shown in Figure 2.1. In this case, the Z boson is produced with small transverse momentum originating from the intrinsic transverse momentum k_T of the partons and soft gluon radiation. In higher order processes the boson is produced with contributions from qg and $q\bar{q}$ scattering and can recoil off additional decay products. The additional quark or gluon in the final state appears as a jet of hadrons. Next-to-leading-order diagrams for the Z production are shown in Figure 2.2.

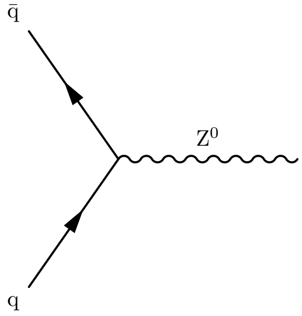

Figure 2.1: Feynman diagram showing the leading-order Z production mechanism in proton-antiproton collisions.

Any process (except $Z \rightarrow \nu\bar{\nu}$) that can be described by Z boson exchange may also be described by γ^* exchange (the electromagnetic Drell-Yan process). The two corresponding terms interfere. However, for the events in the region of the Z pole, studied in this analysis, the Z exchange is dominant.

Since the initial state consists of bound hadrons rather than of free quarks, the measured cross sections are sensitive to the quark distributions of the proton.

The cross section for the subprocess $q\bar{q} \rightarrow Z$ is given at leading-order by [14]:

$$\hat{\sigma}(q\bar{q} \rightarrow Z) = \frac{8\pi G_F}{\sqrt{2}}[(g_V^q)^2 + (g_A^q)^2]M_Z^2\delta(\hat{s} - M_Z^2). \tag{2.1}$$

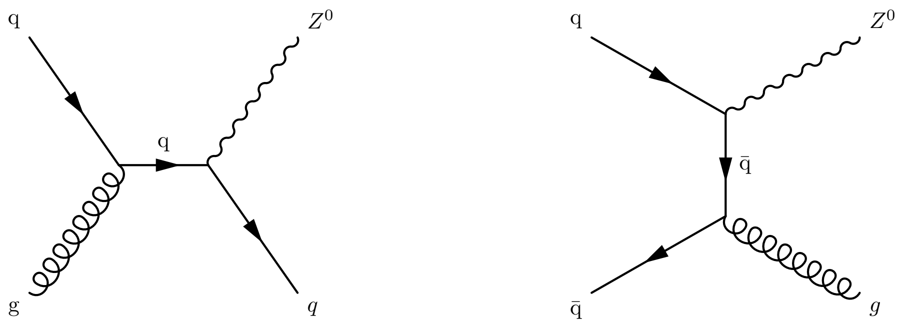

Figure 2.2: Feynman diagrams showing the next-to-leading-order Z boson production mechanisms in proton-antiproton collisions. Left: Compton scattering process. Right: Initial state gluon radiation.

In Equation 2.1 g_V^q and g_A^q denote the strenghts of the vector and axial-vector quark couplings, respectively, and G_F is the Fermi constant. $\hat{s}$ is the centre-of-mass energy of the parton-parton collision and M_Z denotes the mass of the Z boson. A Dirac Delta function is used as an approximation to a Breit-Wigner Z mass distribution (*zero-width approximation*). Convoluting the subprocess cross section with the appropriate parton distribution functions (PDFs) and summing over all possible quark-antiquark combinations in the hard interaction gives the total cross section [14]:

$$\sigma(p\bar{p} \to Z + X) = \frac{K(\alpha_s(Q^2))}{3} \int_0^1 dx_a \int_0^1 dx_b \sum_q f_q(x_a, Q^2) f_{\bar{q}}(x_b, Q^2) \hat{\sigma} \tag{2.2}$$

where $K(\alpha_s(Q^2))$ is a correction factor for higher order QCD processes. The colour factor 1/3 is required to take into account that the quarks must have the same colour. The parton distribution functions, $f_q(x_a, Q^2)$ and $f_{\bar{q}}(x_b, Q^2)$ describe the probability of obtaining a quark and antiquark with momentum fractions x_a and x_b of the proton or antiproton, respectively, at a momentum scale Q^2, where Q is set equal to the Z mass.

2.2.1 *Z* boson decay

The production of the Z boson is immediately followed by a subsequent leptonic or hadronic decay. The partial decay width of $Z \to f\bar{f}$ depends on the decay channel. Since the top quark mass is heavier than the mass of the Z boson, the decay is limited to 11 channels. The partial width of the Z boson into two leptons is given by [14]:

$$\Gamma(Z \to l\bar{l}) = \frac{G_F M_Z^3}{6\sqrt{2}\pi}(|g_A^l|^2 + |g_V^l|^2) \tag{2.3}$$

where g_A^l and g_V^l denote the couplings of the fermion to the Z boson. Some corrections are already absorbed in the measured physical values of M_Z and G_F. Thus, the branching fraction into $\mu^+\mu^-$ which is given by the ratio of the partial decay width to the total width Γ_z is found to be only $Br(Z \to \mu^+\mu^-) \approx 3.4\%$ [4].

2.2.2 Perturbative QCD corrections

The finite transverse momentum of the observed Z bosons can be attributed to multiple gluon radiation in the initial-state. Without any perturbative and nonperturbative corrections, the leading-order process $q\bar{q} \to Z/\gamma^*$ would result in the production of vector bosons with minimal transverse momentum.

In fixed-order perturbative QCD (pQCD) the partonic cross section is calculated by an expansion in powers of the strong coupling constant α_s. This procedure works well for large transverse momenta of the Z boson being equal to Q^2, $p_T^2 \sim Q^2$ with $Q = M_Z$, where M_Z is the mass of the Z boson. When the transverse momentum of the Z boson (p_T^Z) is much less than Q ($p_T^Z \ll Q$), correction terms that are proportional to $\alpha_s \ln(Q^2/p_T^2)$ become significant and the cross section therefore diverges at small p_T^Z. A technique called resummation extends the applicability of pQCD to lower values of p_T by reordering the perturbative series. This technique was originally proposed by Dokshitzer, Dyakonov and Troyan (DDT) [11] and further developed by Collins, Soper and Sterman (CSS) [12].

Large logarithms of the ratio M_Z/p_T are resummed. The differential cross section is given as a Fourier transform in the space of the impact parameter b, where b is the Fourier space conjugate to p_T. The resummation formalism gives a good theoretical description of the vector boson production in the low p_T^Z region. However a more fundamental barrier is encountered when p_{T} approaches the QCD scale $\Lambda_{QCD} \sim 200\,\mathrm{MeV}$[2] and α_s therefore becomes large, so that the perturbative calculation is no longer valid. A phenomenological form factor helps here which accounts for the nonperturbative contribution.

2.2.3 Production of Z bosons in association with jets

The finite transverse momentum of the Z boson is balanced by gluon radiation and quark-gluon processes of the colliding partons prior to their annihilation. A detailed

---

[2] Λ_{QCD} characterizes QCD processes and describes the only free parameter of the QCD.

description of the multijet production with Z bosons can be found in Reference [15]. The total Z cross section can be described by its multijet components:

$$\sigma_Z = \sigma_{Z+0j} + \sigma_{Z+1j} + \sigma_{Z+2j} + \sigma_{Z+3j} + ...$$

and the jet multiplicity cross sections can be perturbatively expanded in the following way:

$$\begin{aligned} \sigma_{Z+0j} &= a_0 + \alpha_s a_1 + \alpha_s^2 a_2 + \cdots \\ \sigma_{Z+1j} &= \alpha_s b_1 + \alpha_s^2 b_2 + \cdots \\ \sigma_{Z+2j} &= \alpha_s^2 c_2 + \cdots \\ & \cdots \end{aligned} \tag{2.4}$$

The coefficients $a_i, b_i, c_i \cdots$ are functions of the jet definition parameters (the size of the cone used to cluster the partons into jets, the transverse momentum, the rapidity and the separation cuts imposed on the jets). The leading-order contributions (a_0, b_1, c_2) can be described by the matrix elements for the parton process. Jet cross section calculations have been performed at next-to-leading-order which include virtual and real corrections to the leading-order process.

$$\sigma_{Z+n}^{NLO} = \sigma_{Z+n}^{virtual} + \sigma_{Z+n}^{real} \quad (n \leq 2)$$

Real corrections include diagrams with the radiation of an extra parton in the final state. Predictions at next-to-next-to-leading-order (NNLO) are only available for 0 jets since the number of diagrams increases rapidly with the order of the calculation.

2.3 Monte Carlo simulation methods

As mentioned before, complete perturbative calculations in QCD have been performed only to NLO in most cases, due to the fact, that the calculation is mathematically very demanding. An explicit calculation of a multi-parton final state would include all partons in a matrix element computation. Since higher order terms cannot be neglected to improve the convergence of the perturbative series, one has to rely on computer simulations (Monte Carlo methods), rather than on analytical methods for the study of the associated production of vector bosons with jets. Hence, several simplifications and approximations must be applied to describe QCD interactions. Nowadays two different approximations have been investigated to model the perturbative interaction: the matrix element (ME) method and the parton shower (PS) approach. Both approximations have their strengths in different kinematic regimes. The two mentioned approaches are implemented in computer simulations, so called Monte Carlo generator programs which will be described in Section 2.3.4.

2.3.1 Matrix Element (ME)

The first approach, the matrix element method calculates Feynman diagrams at leading-order and takes into account exact kinematics, full interference and helicity structure. However, the perturbative calculations of the ME become increasingly complex at higher orders. This sets a limit to its applicability at large parton multiplicities. The ME approach yields more reliable results for the well separated jets at the high energy region since the perturbative expansion of the ME approach behaves better at higher energy scales based upon the running of α_s.

2.3.2 Parton Shower (PS)

The second approach is an approximated result in which enhanced terms are taken into account to all orders by a random process. It serves two main purposes. Firstly, it provides an estimation of the higher order corrections and secondly, it generates high-multiplicity hadronic states which can be converted into the observed hadrons by a hadronization mechanism. The number of partons involved has no explicit upper limit. A $2 \rightarrow 2$ (e.g. $q\bar{q}(\rightarrow Z/\gamma^*) \rightarrow l^+l^-$) core process is generated. All other final state particles are described as being emitted from the core particles in a probabilistic manner using a parton shower approach. The PS method uses a leading-log approximation with simplified kinematics, interference and helicity structure and gives a good description for the substructure of jets. The simplification is valid in the regions where the emissions are soft[3] and collinear[4]. Nevertheless the PS approach yields less reliable results for well separated parton radiation with large momenta described in power series of α_s in the perturbative expansion. Thus the PS approach does not describe the full phase space for well-separated jets.

Since the kinematic domains of the parton shower evolution and the matrix element calculations are complementary the current technology relies on a matching of matrix element calculations with parton showering as described in Section 2.3.4.

2.3.3 Hadronization

Due to the colour confinement all quarks and gluons are not allowed to exist in isolation. Therefore the coloured partons need to be grouped into the observed colour-neutral hadrons using a phenomenological model which is called *hadronization*. An explicit calculation of the hadronization is not yet possible as the involved confinement cannot be described by means of perturbation theory since at low momentum

---

[3] soft means small transverse momentum

[4] collinear means that the angle between the radiating and the radiated particle is very small

scales the value of α_s is too large to allow a perturbative expansion. Two different frequently used models that describe the hadronization process are described below.

Lund string model

The Lund String model described in Reference [16] regards the colour charged particles as being connected by field lines which are attracted by the gluon self interaction. The string has a uniform energy per unit length of $\kappa \sim 1\frac{\mathrm{GeV}}{\mathrm{fm}}$. The colour string is stretched if the quark and antiquarks separate from each other and the potential energy stored in the string increases. If the energy is high enough, the string can break by the production of a new quark-antiquark pair. Further breaks may follow until the energy becomes insufficient. The PYTHIA Monte Carlo event generator described in Section 2.3.4 uses this model for the description of the hadronization. Figure 2.3 (left) shows a schematic view of the Lund String model. Contrary to the cluster model an additonal string is produced if a gluon splits into a quark antiquark pair during the evolution of a parton shower.

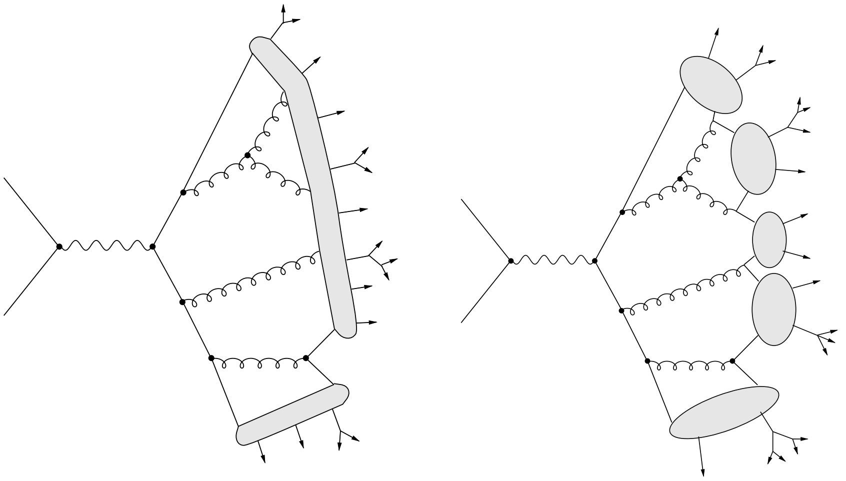

Figure 2.3: Parton shower with string hadronization model (left) and cluster hadronization model (right).

Cluster model

In this model, the remaining gluons at the end of the parton shower evolution are (nonperturbatively) split into quark-antiquark pairs. Neighboring quarks and antiquarks build singlet cluster which decay directly into two hadrons unless they are too heavy, when they decay, or too light in which case the cluster decays into a single hadron. A schematic picture of the cluster hadronization model is shown in Figure 2.3 (right). A detailed description can be found in Reference [17].

2.3.4 Event simulation

Monte Carlo generator programs can simulate high energy physics events. A simulation of the particle reactions is needed to describe the theoretical prediction of physics processes and to interpret the results of analyzed real data. In particle physics Monte Carlo simulations based on the use of random numbers and probability statistics are a commonly used technique in order to investigate particle physics processes. Event generators are based on the theory and models of physics processes including e.g. parton distributions functions, initial- and final-state parton showers and multiple interactions.
Monte Carlo simulations combine parton shower or matrix element hard scatter to nonperturbative hadronization, underlying event models and detector simulation.

Two different event generators programs PYTHIA [18] and ALPGEN [19] are used in this analysis to describe Z boson production processes. These two event generators are described in the following sections.

Pythia

PYTHIA [18] is a leading-order (LO) Monte Carlo generator which is commonly used for the simulation of hadronic processes. Contrary to ALPGEN it does not include a full matching scheme, but only matrix element corrections to the first parton shower branching. The hard scattering process is calculated in leading-order approximation. Higher corrections are approximated via the leading-log parton shower approach. Parton shower and hadronization are applied to the events. The parton shower is modified using weights obtained from the matrix element calculations to describe the vector boson production at hadron colliders. Since only the matrix element corrections for one additional parton are taken into account PYTHIA fails to give a good description of the emission of multiple hard jets (see also Section 4.7).

ALPGEN

ALPGEN [19] is a multi-purpose program which can calculate cross sections for up to six additional partons. It uses the Mangano (MLM) matching algorithm which implements a combination of the matrix element approach and the parton shower evolution and is therefore well suited for the simulation of vector boson production in association with jets. Leading-order matrix elements are calculated and different $2 \rightarrow N$ processes are generated. A reweighting of the matrix element and a veto of shower development in regions of the phase space which have already been sampled by a different parton-level configuration are included. The resulting partons are passed to a parton shower given by PYTHIA for hadronization, which populates the rest of the phase space. The particles are then clustered using a cone jet algorithm. To avoid double counting, a jet-parton matching of the partons from the matrix element with jets, found after applying the parton shower, is performed according to the MLM-matching scheme on parton level. An event is kept if and only if the number of hard well separated hadron level jets equals the number of matrix element partons in the event. For the highest parton multiplicity an inclusive matching is applied. This means that an event is kept if all matrix element partons are allocated to jets. If two partons match the same jet or if one parton does not match the event is rejected. For the exclusive[5] samples all partons have to match to jets. If an extra jet remains which can not be matched to any parton the event is discarded.

This procedure permits the generation of inclusive samples with any jet multiplicity. The hard and well separated jets are described by the matrix element, keeping interference terms, whereas the soft/collinear jets are described by the parton shower, avoiding all divergences.

---

[5] exclusive means that the jet multiplicity of the sample exactly corresponds to the number of partons from the matrix element

3 Experimental Overview

3.1 The Tevatron

The Tevatron accelerator, the main facility of the Fermi National Accelerator Laboratory (Fermilab) is located near Chicago and operates at a center of mass energy of $\sqrt{s} \sim 1.96\,\mathrm{TeV}$. Until the startup of the LHC it is one of the highest energy particle colliders in the world. The Tevatron accelerator is the final stage in a chain of 7 accelerators which produce and accelerate high energy beams of protons and antiprotons before injecting them into the Tevatron ring.
During the first major period of data taking (1991-1995) the production of top-antitop ($t\bar{t}$) events could be observed for the first time [20, 21].

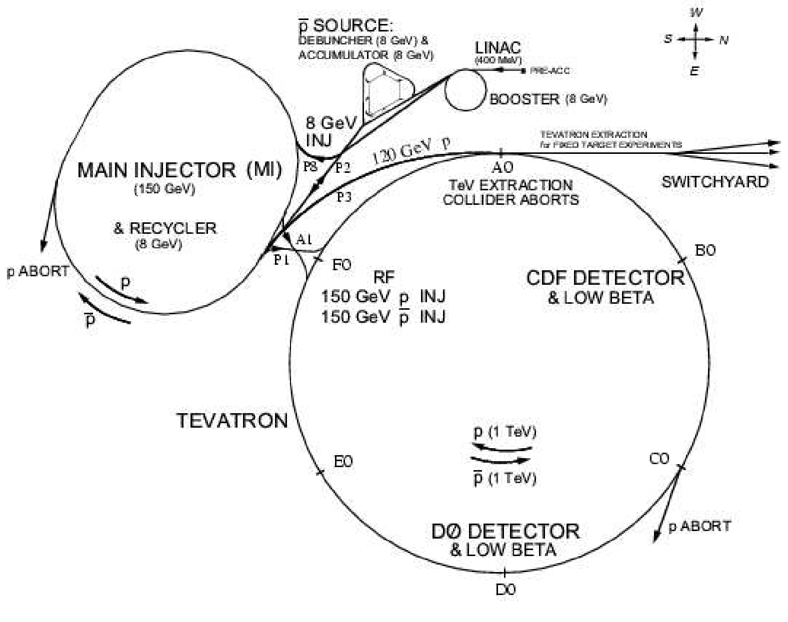

Figure 3.1: Schematic view of the Tevatron accelerator chain

This chapter gives the basics of the Tevatron operation. The design and operation of the accelerator chain is reviewed in some detail in [22]. Figure 3.1 shows the accelerator chain.

Collision experiments can be divided into three different steps: the initial production and injection of the particles, the chain of successive acceleration and finally the collision itself.
Fermilab uses a series of accelerators to create high energetic particle beams. In a first stage the proton beam begins as H^- ions, which are passed through a Cockcroft-Walton accelerator and a linear accelerator LINAC in a second stage, to reach energies of 400 MeV which corresponds to a velocity of $\sim 0.7\,c$. Before entering the third stage, the Booster, the ions pass through a carbon foil, which removes the electrons, leaving only the positively charged protons. The Booster itself, is a circular accelerator that uses magnets to bend the beam of protons in a circular path. The protons travel around the Booster about 20000 times, picking up more energy with each circulation and finally leave the Booster with an energy of 8 GeV. The protons are then transferred to the Main Injector, which is a larger synchrotron ring where they are accelerated from 8 GeV to 120 GeV for fix target operation or to 150 GeV for injection into the Tevatron. Finally, the Main Injector groups the protons and antiprotons from the Antiproton Source in three bunches and delivers them to the Tevatron ring, where each bunch is accelerated to 0.98 TeV.
The separation between the Tevatron and the Main Injector makes it possible to produce antiprotons simultaneously to the collisions in the main accelerator. The Antiproton Source consists of three parts: the Target, the Debuncher and the Accumulator. To produce antiprotons, protons with an energy of 120 GeV from the Main Injector are directed to the Antiproton Source, where the protons collide with a nickel/copper target. The collisions produce a wide range of secondary particles including many antiprotons with a range of momenta. The antiprotons are collected and moved to the Debuncher storage ring, where they are focused into a coherent beam and accelerated to 8 GeV, before being transferred to the Accumulator which is another storage ring. Once a sufficient number of antiprotons has been produced, they are sent to the Main Injector for acceleration and injection into the Tevatron, circulating in the opposite direction to the proton beam.

3.2 The DØ Detector

This section gives an overview of the DØ detector, followed by a short description of the trigger systems used to identify interesting collisions in Section 3.3. A detailed description of the DØ detector can be found in [23].

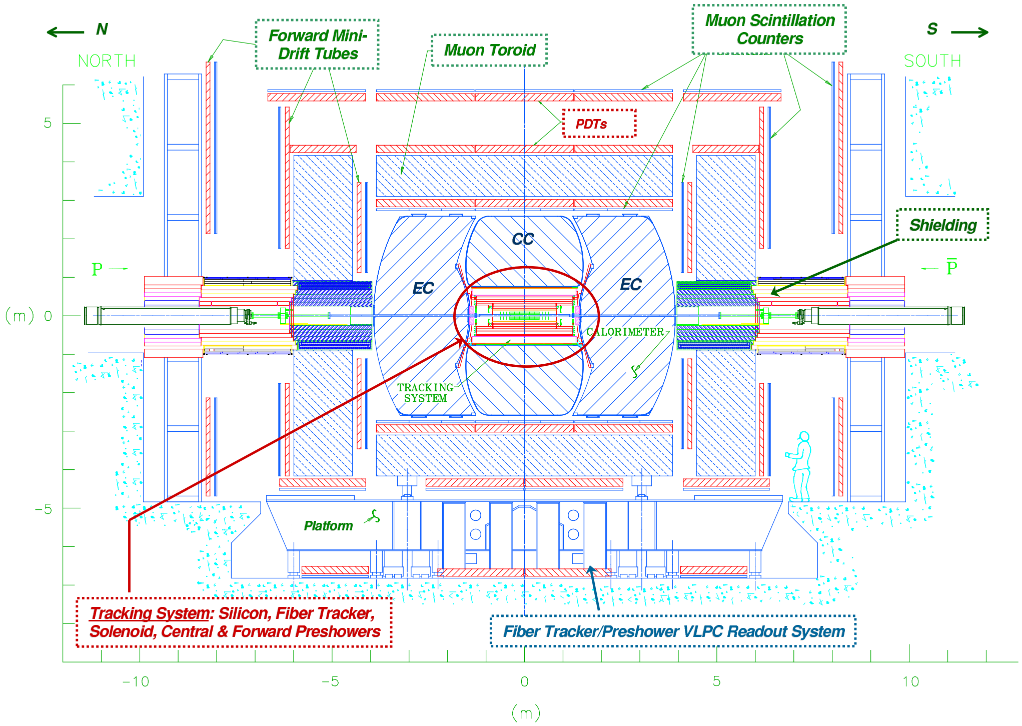

Figure 3.2: A cross section view of the DØ detector

The DØ experiment is located at one out of six possible $p\bar{p}$ collision points of the Tevatron. The DØ detector shown in Figure 3.2 is a multi-purpose particle detector designed to detect $p\bar{p}$ collisions of nearly the full solid angle of 4π at a collision energy of 1.96 GeV. It is a collection of sub-detectors working in tandem to identify and measure the momenta, energies and secondary vertices of particles produced in the collisions.

The Tracking System which recordes the paths of charged particles is described in Section 3.2.2 followed by a description of the DØ calorimetry system which delivers the signals for the jet reconstruction used in this analysis in Section 3.2.3. Another important ingredient for this analysis is the muon system reviewed in Section 3.2.4. It is not only essential for the identification of the muons but also used as a main ingredient for triggering the candidate events.

The DØ detector operates with small dead times for high instantaneous luminosities in the Tevatron collider and bunch crossing times of $\Delta t = 396\,\text{ns}$.

3.2.1 The DØ Coordinate System

DØ uses a right-handed coordinate system to measure directions and positions with the origin at the nominal interaction point. The z axis is defined by the direction of the proton beam, with the antiproton beam thus traveling in the negative z direction. The distribution of interaction points is Gaussian in z, centered around $z = 0$ with a RMS of around 25 cm. The x axis points towards the center of the Tevatron ring and the y axis points vertically upwards. The usual azimuth angle $\phi = tan(y/x)$ is used. Since DØ is not in the center of mass frame of each parton-parton collision, the polar angle θ is replaced by the *pseudorapidity* η, defined as:

$$\eta = -\ln\left(\tan(\theta/2)\right).$$

The pseudorapidity is derived from rapidity, defined by:

$$y = \frac{1}{2}\ln\left(\frac{E+p_z}{E-p_z}\right) = \tanh^{-1}\left(\frac{p_z}{E}\right)$$

where E is the energy and p_z the z momentum component of a particle. The pseudorapidity approximates the rapidity for relativistic particles.

3.2.2 The Central Tracking System

The inner-most apparatus of the DØ detector which is shown in Figure 3.3 is located near the beam pipe inside a solenoid magnet with a 2 Tesla magnetic field. It is a set of two tracking detectors, the inner Silicon Microstrip Tracker (SMT) and the outer

Central Fiber Tracker (CFT). The presence of the magnetic field within the tracking system allows accurate momentum measurements along the curved paths of charged particles. The particle momentum is perpendicular to the magnetic field and can be extracted by measuring the sign and radius of the induced curve. The amount of multiple scattering as well as the individual position measurements affect the accuracy of the measurement and places requirements on the design and construction of the central tracking system. The momentum resolution of the DØ tracking system can be parameterized for tracks at $\eta = 0$ in the following way [23]:

$$\Delta p_{\mathrm{T}}/p_{\mathrm{T}} = 0.02 + 0.002 \cdot p_{\mathrm{T}}$$

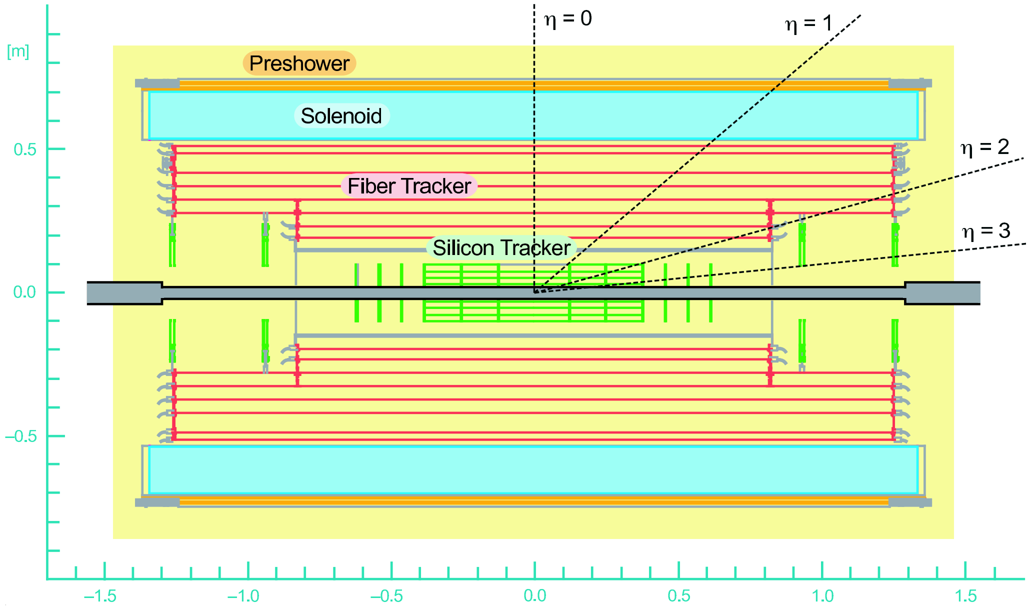

Figure 3.3: Side view of the inner tracker with its solenoid and the surrounding preshower detector.

The Silicon Microstrip Tracker (SMT)

The SMT detector surrounds the Tevatron beam pipe and is designed to provide the reconstruction of primary vertices. It is build by a collection of doped silicon detectors depleted of electric charge. Charged particles entering the depleted region ionize the silicon creating electron-hole pairs. The applied electric field forces the charged particles and holes to drift towards the sensors. The collected ionized charge is used to measure the position of the passing particles. A schematic view of the

SMT is shown in Figure 3.3.
Sixteen layers of wafers are placed perpendicular to the beam which improve tracking for particles with large $|\eta|$. Six cylindrical barrel detectors each containing 4 layers of silicon wafers are arranged in parallel to the beam direction and provide best tracking for particles with small $|\eta|$ and also good separation of primary vertices in multiple interaction events. The hit position resolution of the micro-strip detectors in $r\phi$ is about $10\,\mu$m. The SMT allows tracking in a pseudo-rapidity range of $|\eta| < 3$ and has a total of 793000 readout channels.

The Central Fiber Tracker (CFT)

The CFT is located outside the SMT. It is organized into 8 cylindrical layers of scintillating fibers on carbon support structure. The layers themselves consist of two double-layers of fibers. One set is aligned parallel with the beam axis, providing a measurement of ϕ and r and the other set is rotated by 3° with respect to the beam axis providing stereo information. The fibers themselves have a diameter of $835\,\mu$m, giving a position resolution of $100\,\mu$m per doublet. When a charged particle traverses the fibers, photons are produced which are carried out of the detector by wave guides. The travel distances of the wave guides are between 8 m and 11 m and are recorded on Visible Light Photon Counters (VLPCs), which convert the light into an electronic signal.

The Preshower Detectors

The central (CPS) and forward (FPS) preshower detectors are located outside the solenoid magnet. A combination of tracking and calorimetry is used to provide fast energy and position measurements and to enhance the photon or electron identification. This makes it possible to separate electromagnetic objects from hadrons. Both detectors are made of 3 concentric cylindrical layers of scintillating material. Thin layers of lead in front of the scintillators induce showering. Similar to the CFT the scintillation light is collected through waveguides and transmitted to the VLPC read out system located below the DØ detector. The position resolution for electrons of 10 GeV is better than 1.4 mm [23].

3.2.3 The Calorimeter

The next sub-detector of the DØ detector is the calorimeter, which measures the energy of the lightest electromagnetically interacting particles, such as electrons and photons, as well as strongly interacting particles, such as pions or neutrons. Figure 3.4 shows a three dimensional view of the whole calorimeter. The DØ calorimeter

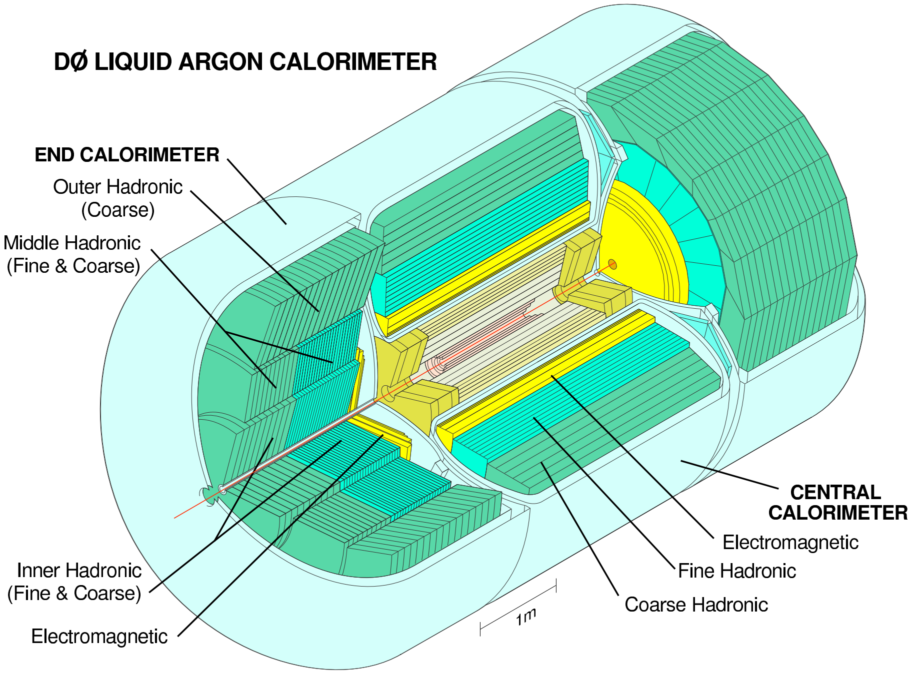

Figure 3.4: Three dimensional view of the liquid argon calorimeter

system uses a sampling approach to provide particle identification and energy measurements by completely absorbing the most particles. It uses liquid argon as the active medium and depleted uranium, copper and steel as absorber material. The DØ calorimeter covers a pseudo-rapidity range of $|\eta| < 4$.

The calorimeter can be divided into three sub-detectors: an inner detector called the EM calorimeter in the central region (CC) covering the pseudo-rapidity range of $|\eta| < 1.2$ and two outer detectors called hadronic calorimeters at the end-cab regions (EC) covering the pseudo-rapidity range of $1.4 < |\eta| < 4$. Each region is surrounded by its own cryostat. The region between the two cryostats is called the inter cryostat region (ICR) and is located in the pseudo-rapidity range of $0.7 < |\eta| < 1.4$. The ICR contains active scintillators to provide also a minimal energy measurement.

The energy is measured by inducing the incoming particles to produce an electromagnetic shower when they collide with a dense material. In the active region particles from the shower ionize the material and the ions move towards a sensor due to an applied bias voltage. The energy deposited by the ionizing particle is proportional to the charge collected. The EM calorimeter is made of alternating layers of depleted uranium, which acts as the shower inducing material and liquid argon acting as the active medium. It has four layers of cells representing nearly 21 radiation lengths.

The hadronic calorimeter consists of the fine hadronic calorimeter and the coarse hadronic calorimeter. This combination provides an additional number of 7 radiation lengths to the detector, which ensure that a particle deposits nearly all its energy inside the detector. The fine hadronic calorimeter employs uranium-nickel alloy as the shower inducing material. The coarse hadronic calorimeter uses plates of copper in the central region and stainless steel in the forward region. Liquid argon is used as the active material in both hadronic and fine hadronic calorimeters.

An excellent energy and position measurement of particles is provided by the fine radial segmentation of the cells. Figure 3.5 shows an octant of the DØ calorimeter including the fine segmentation. The energy resolution of the calorimeter for electrons and charged pions has been determined from test beam data to be [24]:

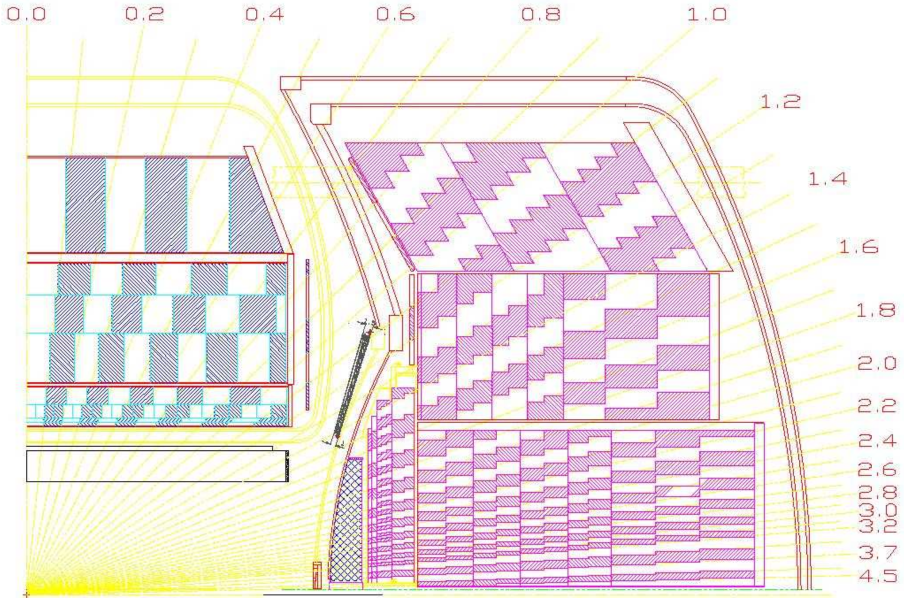

Figure 3.5: One Octant of the DØ calorimeter. The dark and light blocks represent cells in different calorimeter towers.

$$\text{electrons}: \frac{\sigma(E)}{E} = (\frac{15\%}{\sqrt{E}} \oplus 0.3\%)$$

$$\text{pions}: \frac{\sigma(E)}{E} = (\frac{45\%}{\sqrt{E}} \oplus 4\%).$$

3.2.4 The Muon System

The outer-most layer of the DØ detector is the muon detector which is located outside the calorimeter. A schematic view of the muon system is shown in Figure 3.6.

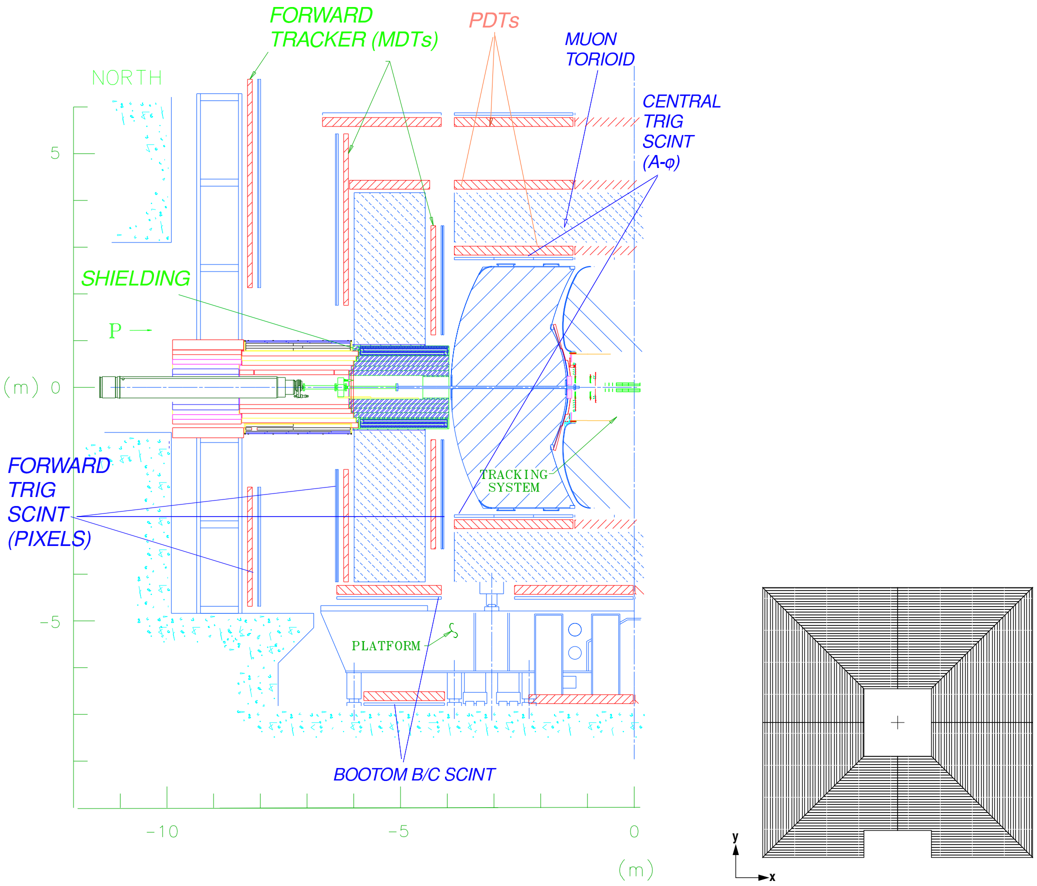

Figure 3.6: Left: Side view of the DØ muon system; Right: Schematic overview of the octant-like alignement of the MDT's

High energy muons penetrate the central tracker solenoid and calorimeter and are therefore identified in a second tracking system. The latter includes a toroid magnet, allowing additional momentum measurement. The muon detector consists of scintillator and drift tubes, with coverage of $|\eta| < 2$. The muon detector can be divided into two active regions called the central system for $|\eta| < 1$ and the forward system for $1 < |\eta| < 2$. Each has three layers (usually called A, B, C with A between the calorimeter and iron and the other two outside the iron) of drift tubes. A toroid iron magnet having a magnetic field of 1.8 T bends the muons from their original paths and helps to provide a local momentum measurement of the events. The drift tube chambers in the central region are called PDTs and MDTs in the forward regions. They differ in size with the PDTs being $5.7 \times 10\,\mathrm{cm}^2$ rectangles while the MDTs are $1\,\mathrm{cm}^2$ squares.
While the drift tube chambers allow precise position measurements, the scintillator counters are mostly used for muon identification, fast triggering and rejection of cosmic rays as well as other sources of background. The PDTs also provide a time division measurement. The light produced by the muons passing through the inner detector is collected by photo-multipliers.
An additional shielding surrounds the beam pipe near the forward muon detector. It reduces spurious beam effects, so that the amount of radiation is reduced.
The momentum resolution of the muon system is limited by multiple scattering at low muon momentum. For high muon momenta it is limited by the individual hit resolution and can be parameterized in the following way [25]:

$$\frac{\sigma_{\mathrm{p}}}{p} = 0.18 + 0.003 \cdot p.$$

A much better momentum measurement is provided by the central tracking detectors. However, in the forward region with SMT coverage only, the muon system measurement is comparable in resolution.

3.3 The DØ Trigger System

A proton antiproton collision occurs every 396 ns. Once a collision has been measured a complex set of trigger decisions must be satisfied before the event is recorded to tape for later analysis. As the total rate of data one can store to tape is limited, not every event is stored. With the increased luminosity and higher interaction rate delivered by the Tevatron, a significantly enhanced trigger system was necessary which tries to select the most “interesting” events and reduces the total rate to 50 Hz. This system is formed by three distinct stages called Level 1 (L1), Level 2 (L2) and Level 3 (L3).

- The first trigger level (L1) is designed to reduce the total event rate from 2.5 MHz to 1.4 kHz. It is a collection of hardware trigger elements and has to act fast to either accept or reject an event. Therefore the available tools for selecting events are limited. For trigger decision only the calorimeter trigger towers, signals in the muon drift chambers or scintillators and the transverse momentum of charged particle tracks in the central fiber tracker are available.

- The second trigger level (L2) acts on all events that have passed the L1 trigger. It is designed to reduce the rate from 1.4 kHz to 700 Hz. The L2 trigger incorporates detector specific pre-processing boards and a global detector board to make trigger decisions. Pre-processors collect data from the L1 trigger as well as readout information from the individual detectors and form physics objects. A global L2 trigger pre-processor uses all the available information to make trigger decisions based on event-wide kinematics.

- Candidates passed by L1 and L2 triggers are sent to the third trigger level (L3) which is a software-based collection of algorithms executed on a collection of computer farm nodes. It reduces the data rate from 700 Hz to 50 Hz and requires the full detector readout to select events. A set of physics tools and filters is used to identify interesting topologies and suppress the accept rate.

3.3.1 Muon Trigger

The events selected for this analysis are triggered by a combination of 23 single muon triggers with an inclusive OR, which are characterized by high efficiency and purity. Muon hits in L1 and L2 are found and a fraction of events also passes the L3 muon track requirement. A more detailed description of this method is given in reference [26].

3.4 Detector simulation

The Monte Carlo event generators as described in Section 2.3.4 can e.g. provide predictions of jet observables such as particle multiplicities and energy spectra. Other properties as the calorimeter jet properties often depend on these quantities in a complex way. Therefore many effects can be studied only by feeding the full Monte Carlo simulation of an event through a detailed detector simulation. This simulation calculates the effects on the particles due to the magnetic fields and the material of the detector with realistic efficiencies, responses and resolutions. These are then digitized and processed through a simulation of the detector electronics. In a last step the events are reconstructed in a process identical to data.

3.4.1 Geant

Geant [34] propagates the stable hadrons (and all other elementary particles) produced e.g. by the former Monte Carlo generators through matter based on the DØ RunII detector simulation. It models the effects on the particles due to the magnetic fields and the dead and active material in the detector. The description includes the productions of secondary particles and a model for the energy deposition and absorption. The output is simulated data as produced by the real detector and is reconstructed into physics objects with the same reconstruction software that is used for real data events.

3.4.2 Zero bias overlay

High luminosity effects (e.g. extra interactions within the same beam crossing) can be described by Monte Carlo underlying event models. But since these simulations are known to be problematic and the DØ detector simulation has suffered from disagreements between data and simulation DØ uses an alternative method to describe these effects. Events that are measured in the detector when no hard collision is triggered are overlayed on top of the simulated events. The properties of these underlying events are luminosity dependend. Therefore the zero bias data set used should resemble the luminosity distribution of the full data set.

4 Event reconstruction and data selection

4.1 Offline event reconstruction

All physics objects in data and Monte Carlo simulation are reconstructed from the raw detector data using the standard DØ event reconstruction software *d0reco* [35]. Computing farms are deployed to analyze the data and reconstruct candidates of physical objects (tracks, muons, jets etc.) that are used in the final analysis.

4.1.1 Muon reconstruction

Muons are reconstructed using the inner tracking detectors, the calorimeter and the muon chambers to identify muons and determine their momentum. A simultaneous global fit through all hits in the three detector components provides the muon track information. The quality criteria of the muon are divided into three categories (loose, medium and tight) with increasing quality. For this analysis all muons are required to have at least *loose* quality. A *loose* muon must fulfill at least two of the following criteria (A,B and C denotes the layers of the muon detector described in section 3.2.4):

- at least one hit in the A-layer scintillators and two hits in the A-layer wires
- at least one hit in the BC-layer scintillators
- at least two hits in the BC-layer wires

In addition a matched muon track is required with distance of closest approach to the reconstructed vertex less than 0.02 cm or 0.2 cm for tracks with and without SMT hits, respectively. This requirement helps to reject cosmic muons. The transverse momentum of tracks where no hits are found in the SMT subdetector is corrected by the beam-spot correction. This correction uses the primary vertex as constraint for a fit and refits the tracks such that the distance of closets approach in x and y retains 0 [36]. The transverse momentum of the muon can be determined from the muon detector information. But due to the better resolution of the central tracking system compared to the muon system, only muons with a matching central track are considered in this analysis. In simulated events the muon transverse momentum is further over-smeared so that the width of the $Z \to \mu^+\mu^-$ peak match the one in data. This is done using the following formula [37]:

$$\frac{q}{p_T} \to \frac{1}{p_T} + A \cdot G_1 + \frac{B\sqrt{\cosh(\eta)}}{p_T} G_2$$

where q is the charge and p_T the transverse momentum of the muon. A and B are numbers depending on the pseudo-rapidity η and the run number and G_1 and G_2 are random numbers distributed according to the normal law.

4.1.2 Jet reconstruction and identification

Interactions with quarks and gluons in the final state occur at a very high rate at the Tevatron. Instead of quarks and gluons which cannot be detected directly due to the color confinement, collimated streams of hadrons (jets) created by the hadronization of quarks and gluons are observed in the detector.

Production of jets

The high energetic collisions of a proton and an antiproton lead to an interaction of a pair of partons. These partons start radiating gluons and quarks which emit further gluons splitting again into pairs of quarks and antiquarks as detailed in Figure 4.1. The induced parton shower forms a bunch of high energetic partons, the parton jets. Due to the confinement colour-neutral stable particles are built which form the particle jets. Calorimeter jets are then made up of objects measured in the calorimeter using a jet reconstruction algorithm which associates the energy depositions in the calorimeter with the initial parton. This analysis deals with particle and calorimeter jets.

Jet cone algorithm

Jets are reconstructed from energy deposits in the calorimeter cells. DØ uses the *RunII Midpoint Jet Cone Algorithm* [38], with a cone radius of $R = \sqrt{(\Delta\phi)^2 + (\Delta y)^2} =$ 0.5 or 0.7. This iterative algorithm can be applied both at particle jet level and at

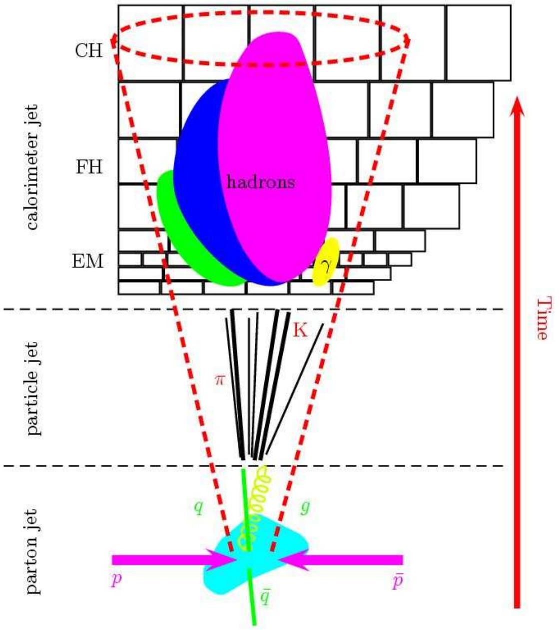

Figure 4.1: Jet production and detection at the level of parton jets, particle jets and calorimeter jets.

level of reconstructed calorimeter towers (calorimeter jets). A cone defined in $\phi \times y$ space associates all particles whose trajectories (or towers whose centers) lie within this cone with radius R together to form proto-jets. Starting with an initial seed axis for the cone, the energy weighted centroid is calculated based on contributions from all particles within the cone. The process is iterated using this new cone axis until a stable position (ϕ, y) is found, where the centroid of the energy depositions within the cone is aligned with the geometric axis of the cone. After the first round of iterations mid-points between pairs of proto-jets are used as additional seeds and the iterative process is repeated. Since the list of stable proto-jets contains many overlapping and identical jet candidates, identical solutions and proto-jets with a transverse momentum less than a given value ($p_{T,proto-jet} < p_{T,min}/2$) are removed from the list. The latter step speeds up the reconstruction and avoids the merging of many noise or minimum bias jets. A split and merge procedure resolves overlapping cones. Two overlapping proto-jets are merged if they contain more than a fraction $f = 50\%$ of $p_{T,proto-jet}$ in the overlap region. Otherwise the jets are split. The particles in the overlap region are assigned to the nearest jet and the axes are recomputed. The algorithm starts with the highest p_T proto-jet and after each step the ordering is recomputed. All remaining candidates with an energy of at least 8 GeV are considered as reconstructed jets.

Jet identification

The jet multiplicities and properties are distorted by the presence of 'fake' jets either created by fake energy in the calorimeter or by real low energy jets which collect sufficient fake energy to pass the energy threshold cuts. Therefore a set of quality cuts has been defined that ensure that the energy distributions in the various layers of the calorimeter are reasonable, and that the jets are not due to spurious energy deposits [39].

A cut on the fraction of jet energy deposited in the coarse hadronic section of the calorimeter removes jets which have been formed mainly from cells in this noisy calorimeter section. Isolated electromagnetic particles are rejected by cuts on the fraction of jet energy deposited in the electromagnetic layers of the calorimeter. Since jets are broad objects it is expected that the energy is found in several calorimeter towers which is ensured by requiring the number of towers containing 90% of the jet energy to be larger than 1. A cut on the ratio of the energy in the highest (hottest) calorimeter cell to that in the second highest calorimeter cell assigned to the jet ensures that the jet is no 'fake' jet due to hot cells, i.e. that the jet is not clustered around a hot cell. Since fake jets surviving the former quality criteria appear mostly at the reconstruction stage, but are not seen in the trigger readout a confirmation of the jet by the Level1 trigger readout chain is required. Only jets passing these quality criteria are selected.

Jet energy scale correction

The energy of the reconstructed jets is given by the sum of energies deposited in the calorimeter cells associated with the jet by the cone algorithm. The jet energy scale (JES) calibrates the reconstructed jet energy to the energy of the jets at particle or hadron level, before interaction with the detector. The measured jet energy needs to be corrected to account for the hadronic response, fragmentation losses outside the cone, calorimeter noise and underlying event energy within the cone, using the jet energy scale correction.

The dominant part of this correction is due to the jet response ($R_{jet} = \frac{E_{meas}}{E_{true}}$) in the calorimeter, which measures the calorimeter response of hadronic particles and the amount of energy within a jet that is lost due to dead material in the calorimeter. The jet energies are studied in $\gamma+$jet events where the high energetic γ is contained in a few calorimeter cells. The γ recoils from a jet and therefore allows a precise calibration of the jets energy. By conservation of transverse energy it is possible to correct the jet energy.

Another contribution to the JES correction is due to energy contributions (offset energy, E_0) that are not related to the physics processes and hence are subtracted from the measured jet energy (E_{jet}^{meas}). This term contains contributions from multiple interactions, underlying event energy, electronic and uranium noise and pile-up energy from previous interactions.

A third parameter, the out of cone showering term (R_{cone}) corrects for energy losses/gains due to calorimeter showering effects from particles located inside/outside of the particle jet.

If E_{jet}^{meas} is the measured jet energy, the particle level jet energy is obtained from the measured jet energy using the following relationship [40]:

$$E_{jet}^{corr} = \frac{E_{jet}^{meas} - E_0}{R_{cone} \cdot R_{jet}}$$

Figure 4.2 displays the overall jet energy scale correction as function of jet energy and η in data.

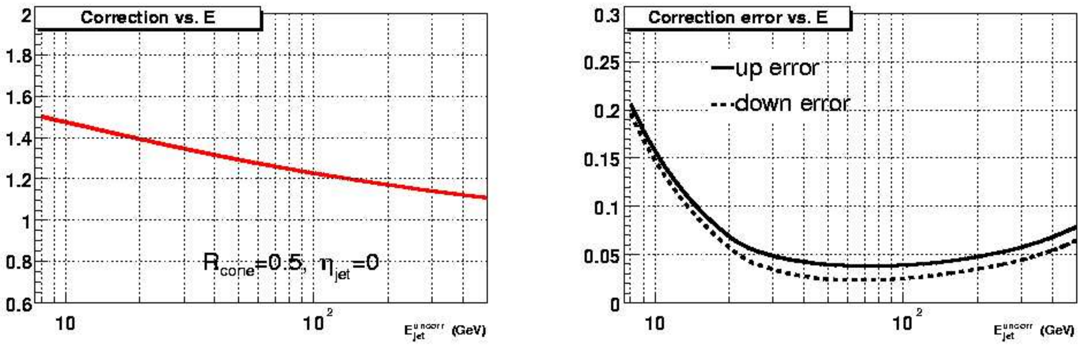

Figure 4.2: The overall jet energy correction factor measured for jets in data as a function of E for $R = 0.5$ and $\eta = 0$.

4.2 Data sample

This measurement is based on the full RunIIa data set collected with the DØ detector from April 2002 to February 2006. Only data taken with all parts of the detector working properly are used. Runs with bad data quality (determined with the run quality database [41]) in the muon system, central tracking system or calorimeter are removed. Luminosity blocks which were flagged as "bad" by the luminosity, jet and missing transverse energy groups were excluded as well. The analysis is performed using the "2MUhighpt" skim created by the Common Samples Group as a preselected subsample, containing only events which have at least two reconstructed muons with transverse momenta greater than 10 GeV [42]. Data events are selected

by an “ORING” of single muon triggers as described in Ref [26]. Trigger weights parameterized in terms of muon ϕ and $\eta_{detector}$ are used to simulate the trigger efficiencies in the Monte Carlo.
In total the sample has an integrated luminosity of $\mathcal{L} \approx 1046\,\mathrm{pb}^{-1}$ (calculated using the `getLuminosity` software package provided by the luminosity ID group [43]).

4.3 Monte Carlo samples

Different Monte Carlo (MC) samples for the signal (listed in Table 4.1) and background processes (listed in Table 4.2 and 4.3) for comparisons with the data are used. All events are processed trough the full DØ detector simulation. Samples of simulated $Z \to \mu^+\mu^-$ +jet events have been generated using ALPGEN (v2.05) in separate parton jet multiplicity bins, with PYTHIA providing the simulation of parton shower and hadronization. The different samples are combined using the MLM [19] matching scheme. All samples have been produced using the `CTEQ6L1` PDF sets. The event distributions are obtained by combining the matched samples with multiplicities up to 5 additional partons scaled to the same luminosity ($1046\,\mathrm{pb}^{-1}$). The corresponding weight factors can be found in Table 4.1. The total ALPGEN cross section of 194 pb is calculated by summing the matching weights. The ALPGEN cross sections are rescaled with a factor 1.29 to match the NNLO prediction 256 pb for the Z cross section [44]. In addition a $Z \to \mu^+\mu^-$ Monte Carlo sample generated using PYTHIA 6.323 [18] with `CTEQ6L1` parton distribution functions (PDF) has been used.

Process		Events	$\sigma \times BR\,[\mathrm{pb}]$	weight
ALPGEN				
$Z/\gamma^* \to \mu\mu + 0lp\,(excl.)$	$(60 < M < 130\,\mathrm{GeV})$	2296346	139.2	1.0
$Z/\gamma^* \to \mu\mu + 1lp\,(excl.)$	$(60 < M < 130\,\mathrm{GeV})$	941862	41.6	0.737
$Z/\gamma^* \to \mu\mu + 2lp\,(excl.)$	$(60 < M < 130\,\mathrm{GeV})$	564733	10.2	0.298
$Z/\gamma^* \to \mu\mu + 3lp\,(excl.)$	$(60 < M < 130\,\mathrm{GeV})$	188284	2.42	0.211
$Z/\gamma^* \to \mu\mu + 4lp\,(excl.)$	$(60 < M < 130\,\mathrm{GeV})$	75411	0.535	0.107
$Z/\gamma^* \to \mu\mu + 5lp\,(incl.)$	$(60 < M < 130\,\mathrm{GeV})$	49245	0.17	0.060
PYTHIA				
$Z/\gamma^* \to \mu\mu$	$(60 < M < 130\,\mathrm{GeV})$	5.3M	256	-

Table 4.1: $Z \to \mu^+\mu^-$ Monte Carlo samples. Given are the number of events, the corresponding cross sections times branching ratio and weights. The cross sections are at leading order. The weights are relative weights scaled to the integrated data luminosity ($1046\,\mathrm{pb}^{-1}$) to combine the different Monte Carlo samples ("lp" stands for light-parton in ALPGEN). The combined ALPGEN sample and the PYTHIA sample are then rescaled to the next to next to leading order cross section of 256 pb [44].

Process		Events	$\sigma \times BR$ [pb]	weight
Alpgen				
$t\bar{t} + 0lp\,(excl.)$		223765	0.45	0.0018
$t\bar{t} + 1lp\,(excl.)$		96381	0.18	0.0017
$t\bar{t} + 2lp\,(incl.)$		148099	0.14	0.0008
Alpgen				
$Z/\gamma^* \to \tau\tau + 0lp\,(excl.)$		890980	139.2	0.2152
$Z/\gamma^* \to \tau\tau + 1lp\,(excl.)$		204423	41.6	0.2804
$Z/\gamma^* \to \tau\tau + 2lp\,(excl.)$		96551	10.3	0.1466
$Z/\gamma^* \to \tau\tau + 3lp\,(incl.)$		93619	3.3	0.0486
Alpgen				
$Z/\gamma^* \to \mu\mu + 0lp\,(excl.)$	$(15 < M < 60\,\mathrm{GeV})$	607072	334.1	0.5788
$Z/\gamma^* \to \mu\mu + 1lp\,(excl.)$	$(15 < M < 60\,\mathrm{GeV})$	475931	38.6	0.0851
$Z/\gamma^* \to \mu\mu + 2lp\,(excl.)$	$(15 < M < 60\,\mathrm{GeV})$	191773	10.15	0.0056
$Z/\gamma^* \to \mu\mu + 3lp\,(incl.)$	$(15 < M < 60\,\mathrm{GeV})$	94436	3.1	0.0463
Alpgen				
$Z/\gamma^* \to \mu\mu + 0lp\,(excl.)$	$(130 < M < 250\,\mathrm{GeV})$	102912	0.900	0.0091
$Z/\gamma^* \to \mu\mu + 1lp\,(excl.)$	$(130 < M < 250\,\mathrm{GeV})$	95836	0.359	0.0038
$Z/\gamma^* \to \mu\mu + 2lp\,(excl.)$	$(130 < M < 250\,\mathrm{GeV})$	96738	0.097	0.0010
$Z/\gamma^* \to \mu\mu + 3lp\,(incl.)$	$(130 < M < 250\,\mathrm{GeV})$	89368	0.053	0.0006

Table 4.2: Background Monte Carlo samples. Given are the number of events and the corresponding leading order cross sections times branching ratio. The weights are relative weights scaled to the integrated data luminosity ($1046\,\mathrm{pb}^{-1}$) to combine the different Monte Carlo samples ("lp" stands for light-parton in Alpgen).

Process		Events	$\sigma \times BR$ [pb]	weight
Alpgen				
$W \to l\nu + 0lp\,(excl.)$	$(60 < M < 60\,\mathrm{GeV})$	2451378	4574.3	0.8874
$W \to l\nu + 1lp\,(excl.)$	$(15 < M < 60\,\mathrm{GeV})$	2983789	1273.9	0.2653
$W \to l\nu + 2lp\,(excl.)$	$(15 < M < 60\,\mathrm{GeV})$	1758849	302.94	0.0816
$W \to l\nu + 3lp\,(excl.)$	$(15 < M < 60\,\mathrm{GeV})$	920108	72.52	0.0375
$W \to l\nu + 4lp\,(excl.)$	$(15 < M < 60\,\mathrm{GeV})$	941495	16.42	0.0083
$W \to l\nu + 5lp\,(incl.)$	$(15 < M < 60\,\mathrm{GeV})$	76670	5.96	0.0370

Table 4.3: Background Monte Carlo samples. Given are the number of events and the corresponding leading order cross sections times branching ratio. The weights are relative weights scaled to the integrated data luminosity ($1046\,\mathrm{pb}^{-1}$) to combine the different Monte Carlo samples ("lp" stands for light-parton in Alpgen).

4.4 Event selection

$Z \to \mu^+\mu^-$ events are selected at reconstruction level and in case of simulated data also at particle level.

4.4.1 Muon selection

Reconstruction level

All muons used in this analysis are identified by requiring a track in the central detector that is matched to a track of at least "loose" quality in the muon chambers. The requirement of two reconstructed high momentum muons ($p_{\mathrm{T}}(\mu_1) > 20\,\mathrm{GeV}$ and $p_{\mathrm{T}}(\mu_2) > 15\,\mathrm{GeV}$) on the transverse momentum of the muon tracks and the tracking isolation criteria ($\sum_{\mathrm{tracks}}^{R<0.5} p_{\mathrm{T}} < 4.0\,\mathrm{GeV}$) rejects the background from multijet production. In order to ensure high trigger and reconstruction efficiencies the muons are required to be within the central region of the detector ($|\eta_{detector}| < 1.7$) excluding the region of the bottom gap ($|\eta| < 1.0$ and $4.25 < |\phi| < 5.15$). The primary vertex of each muon is required to lie within $|z| < 50\,\mathrm{cm}$. Cuts on the timing information of the scintillation detectors and on the distance of closest approach of the muon track to the reconstructed vertex suppress the cosmic-ray muon background.
Real data events are in addition required to have fulfilled one of the triggers in the single muon OR and at least one muon has to be matched to all the required trigger elements.

Truth level

Truth level muons are identified after QED final state radiation as the two particles[1] which have a truth Z boson as mother. The same η cut as at reconstruction level is applied.

4.4.2 Jet selection

Reconstruction level

All selected jets need to pass the standard jet ID quality criteria described in Ref. [39]. The jet energies are corrected to account for fragmentation losses outside the jet cone, calorimeter noise, the underlying event and hadronic response using the

---

[1] with ParticleDataGroup-ID 13 and −13

jet energy scale correction [40]. Only jets with transverse momentum greater than 15 GeV and $|\eta| < 2.5$ are considered.

Truth level

Particle jets are reconstructed applying the `D0RunII` [38] jet finding algorithm (which is identical for thruth level and reconstruction level) with a cone size of 0.5 to all final state Monte Carlo particles except the two muons from the boson decay. The transverse momentum of the particle jets has to be greater than 6 GeV and $|\eta| < 2.5$. In addition also the `pxcone` [46] and the `SISCone` [47] jet finding algorithms are applied.

4.4.3 $Z\ /\gamma^*$-Selection

$Z/\gamma^* \rightarrow \mu^+\mu^-$ events are characterized by two opposite-sign muons with high p_T. Only events with a di-muon mass between 65 GeV and 115 GeV are selected at truth level and at reconstruction level. A muon isolation cut rejects any events that have a jet within $\Delta R < 0.5$ of a muon.

4.5 Corrections and treatment of data and Monte Carlo

Some corrections need to be applied to the simulation to accurately reproduce the data.
In Alpgen (v2.05) the signal distribution of $Z+$ jet events has a depletion of events in the mass range 60 GeV to 80 GeV. As a correction the corresponding Monte Carlo samples are reweighted in the corresponding mass range according to the generated invariant Z mass [48].
In addition the Monte Carlo is reweighted according to the instantaneous luminosity profile in data to match the data. Figure 4.3 compares the default Monte Carlo luminosity profile with the one seen in data and the reweighted Monte Carlo luminosity profile.

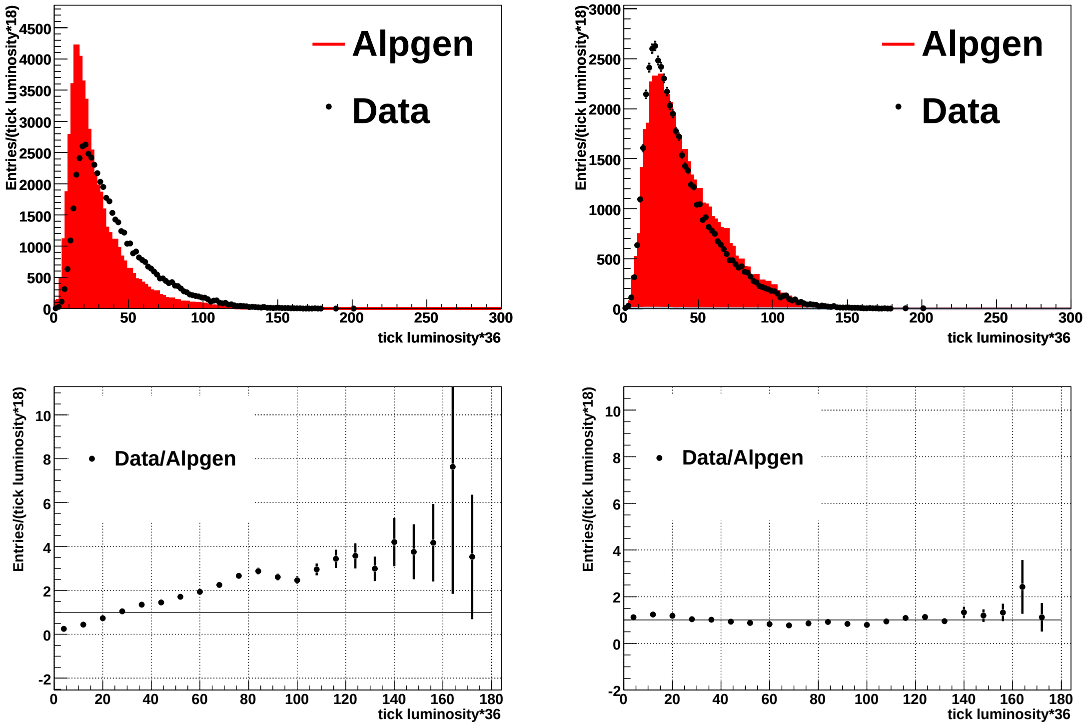

Figure 4.3: Instantaneous Luminosity Profiles; Left side: Default Alpgen compared to data; Right side: Reweighted Alpgen compared to data

Since the trigger is not modeled in the simulation the simulated events are corrected for the trigger efficiency.
Due to the fact that the detector simulation uses an idealized detector geometry

and that some dead material is not implemented in the Monte Carlo simulation the resolution of the transverse momentum of the muons is overestimated in Monte Carlo. The standard prescription described in section 4.1.1 is used to over-smear the resolution in Monte Carlo [37].

Since the track reconstruction and muon identification efficiencies are different in data and event simulation, the ratio of the two efficiencies is used to reweight the simulated events. Both scale factors are standard corrections [36].

Jets in the vicinity of muons potentially reduce the efficiency of the muon isolation cut. Therefore the muon isolation efficiency is determined as a function of the number of jets in the corresponding event. For this purpose events originating from Z boson decays in the reconstructed mass range 60 GeV to 130 GeV are selected. The amount of background events in the data is negligible. Two muons of 'loose' quality matched to central tracks need to be separated by $\Delta\phi > 2$. One of the muons has to be isolated according to the tracking isolation criterion $\sum_{\text{tracks}}^{R<0.5} p_{\text{T}} < 4.0\,\text{GeV}$. The second muon is tested whether it fulfills this isolation criterion. Figures 4.4 and 4.5 show the isolation efficiency for data and simulation as a function of the number of jets with respect to the muon's pseudo rapidity η for jets with transverse momenta greater than 15 GeV and greater than 20 GeV, respectively. The corresponding efficiencies found by averaging over η are listed in Table 4.4.

# of jets	Data efficiency	Monte Carlo efficiency	Ratio
$p_T(\text{jet}) > 15\,\text{GeV}$			
0	9.8962e-01 ± 3.2750e-04	9.8839e-01 ± 9.8921e-05	1.0012e-00 ± 3.4211e-04
1	9.5798e-01 ± 1.2196e-03	9.5951e-01 ± 3.5924e-04	9.9841e-01 ± 1.2714e-03
2	9.0723e-01 ± 3.7110e-03	9.3301e-01 ± 1.0488e-03	9.7237e-01 ± 3.8564e-03
≥ 3	8.5519e-01 ± 8.8918e-03	9.1795e-01 ± 2.6105e-03	9.3163e-01 ± 9.2671e-03
$p_T(\text{jet}) > 20\,\text{GeV}$			
0	9.8962e-01 ± 3.0530e-04	9.8840e-01 ± 9.2867e-05	1.0012e-00 ± 3.1911e-04
1	9.4408e-01 ± 1.7507e-03	9.5261e-01 ± 4.9476e-04	9.9105e-01 ± 1.8193e-03
2	8.6672e-01 ± 6.7999e-03	9.1878e-01 ± 1.8910e-03	9.4334e-01 ± 7.0579e-03
≥ 3	7.7585e-01 ± 2.0441e-02	9.1151e-01 ± 6.2702e-03	8.5117e-01 ± 2.1381e-02

Table 4.4: Isolation efficiencies

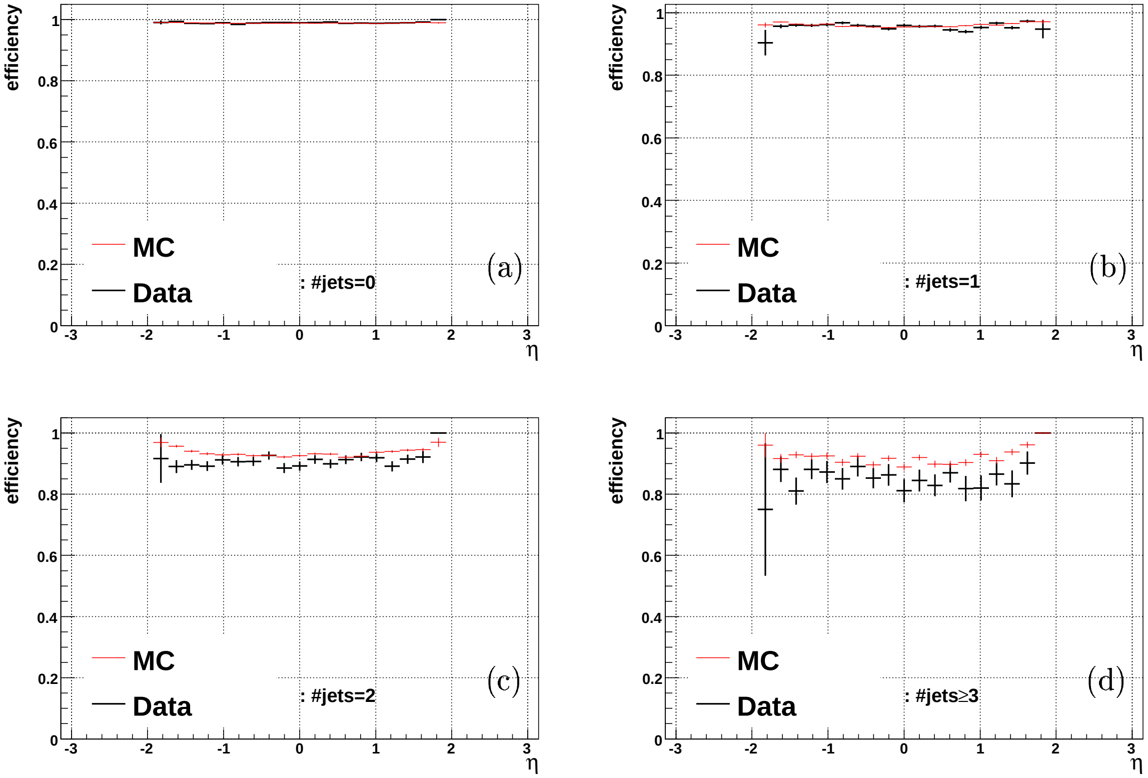

Figure 4.4: Isolation efficiency for (a) events with accurately 0 jets, (b) with 1 jet, (c) with 2 jets and (d) with at least 3 jets with $p_T(\text{jet}) > 15\,\text{GeV}$ as function of muon pseudorapidity η.

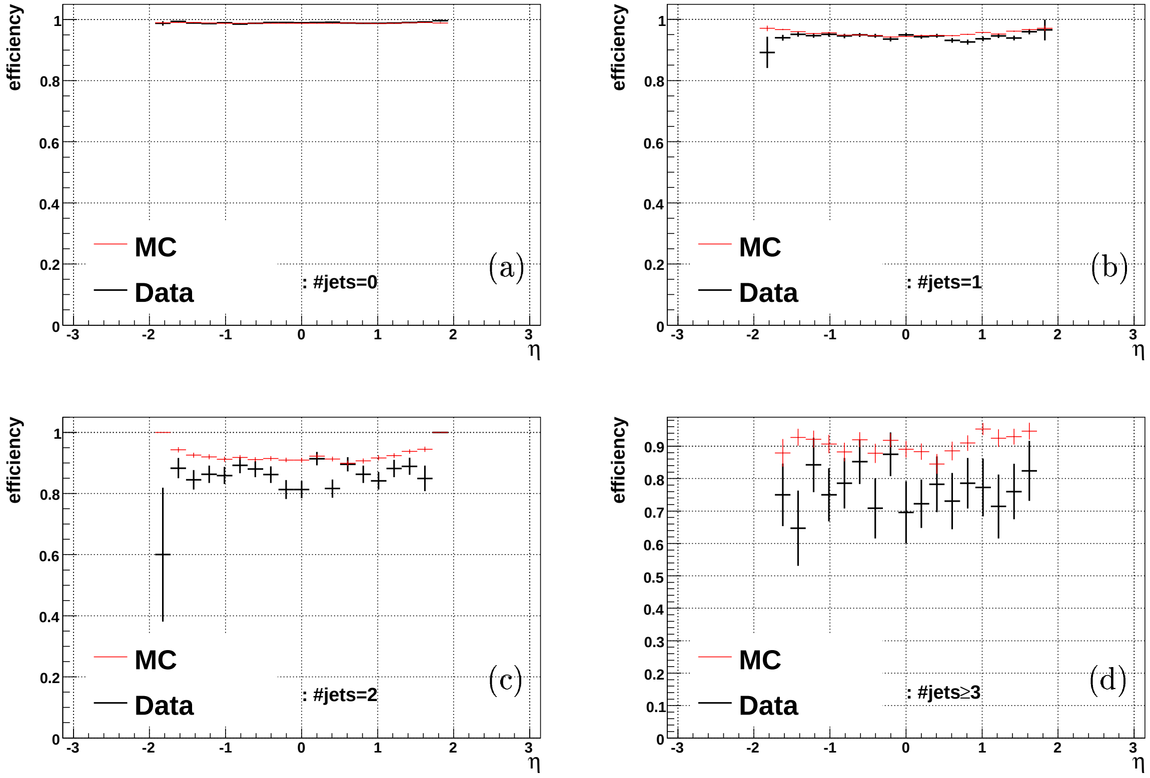

Figure 4.5: Isolation efficiency for (a) events with accurately 0 jets, (b) with 1 jet, (c) with 2 jets and (d) with at least 3 jets with $p_T(\text{jet}) > 20\,\text{GeV}$ as function of muon pseudorapidity η.

To account for the relative difference in the jet energy scale (JES) between data and event simulation the energies of the simulated jets are shifted. An additional over-smearing of the energies corrects for the broader jet energy resolution in data compared to the event simulation. Differences in data and event simulation can also arise from the reconstruction and identification efficiencies. Since both efficiencies have reached their plateau at $p_T(jet) \sim 15\,\text{GeV}$, a jet p_T threshold of 15 GeV is required. A detailed description of this correction method including systematic errors is given in Reference [49].

All Monte Carlo samples are normalized to the integrated luminosity of the data sample. The relation $N_{data} = \mathcal{L}\cdot\sigma\cdot f_{MC}$ (where N_{data} is the number of data events and f_{MC} a scale factor taking into account the acceptance and reconstruction efficiency) should be satisfied for the mass range $60\,\text{GeV} < \text{M}_{\mu\mu} < 130\,\text{GeV}$. To calculate the normalization factor f_{MC}, the $Z \to \mu^+\mu^-$ Monte Carlo with a predicted cross section at NNLO of 256 pb [45] in the mass range $60 < \text{M}_{\mu\mu} < 130\,\text{GeV}$ is fitted to the data. This leads to a Monte Carlo scaling factor $f_{MC} = 0.2$. Figure 4.6 shows the comparison of the data and Monte Carlo events for the mass range 60 GeV to 130 GeV.
The jet multiplicities are underestimated by ALPGEN and PYTHIA as can be seen from Figure 4.7. Therefore distributions of the leading, second leading and third leading p_T(jet) are normalised with respect to the number of events in the corresponding plot to better compare the shapes of the distributions.

4.6 Background

The background contributions are evaluated using the simulated Monte Carlo events listed in Tables 4.2 and 4.3.
The contribution of $W+$ jet events with non-prompt or fake muons is studied using the $W+$ jet samples listed in Table 4.3. The fraction of events in the sample of selected Z events is measured to be 0.08% and thus negligible as well as the background arising from multijet production which requires two fake muons. Also events with di-muon pairs with reconstructed invariant masses between 65 GeV and 115 GeV that originate from Z/γ^* with true invariant masses outside 60 GeV to 130 GeV are treated as background. The fraction of all background events in the sample of selected Z candidate events is found to be less than 0.4% and has a negligible effect on the measurement.

4.7 Comparison of uncorrected data with simulation

Comparisons of data and Monte Carlo at reconstruction level are shown. Since the jet multiplicity is not well modeled in the Monte Carlo, all variables are normalized to the same number of events in each plot. An exception is the jet multiplicity, which is normalized to the same number of inclusive Z events.
The invariant di-muon mass in the range 65 GeV to 115 GeV is displayed in Figure 4.6. Figure 4.7 shows the jet multiplicity for jets with $p_T(\text{jet}) > 15\,\text{GeV}, 20\,\text{GeV}$ and 28 GeV, respectively. It can be seen that the Pythia Monte Carlo produces too few jets and thus underestimates the higher jet multiplicities. This is due to the fact that Pythia only takes into account matrix-element corrections for one additional parton as has been outlined in section 2.3.4. Figures 4.8, 4.9 and 4.10 show the distributions for the leading, trailing and third leading $p_T(\text{jet})$, respectively. Pythia produces a softer spectrum than data and does not describe the hight $p_T(\text{jet})$ regions.

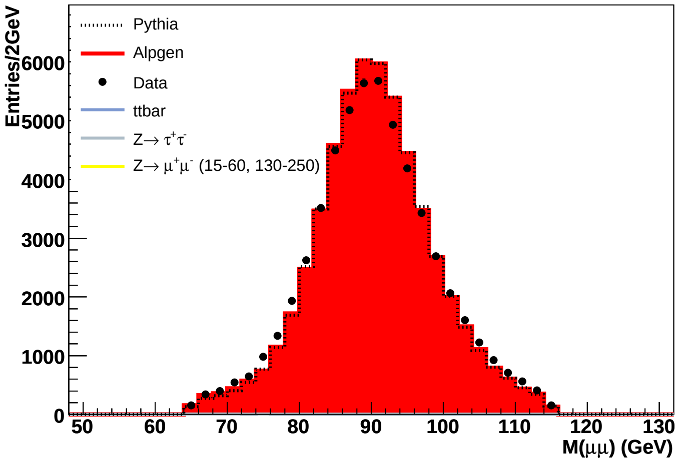

Figure 4.6: Di-muon mass spectrum at reconstruction level for data (black dots) compared to the predictions of Alpgen (red histogram) and Pythia (black histogram).

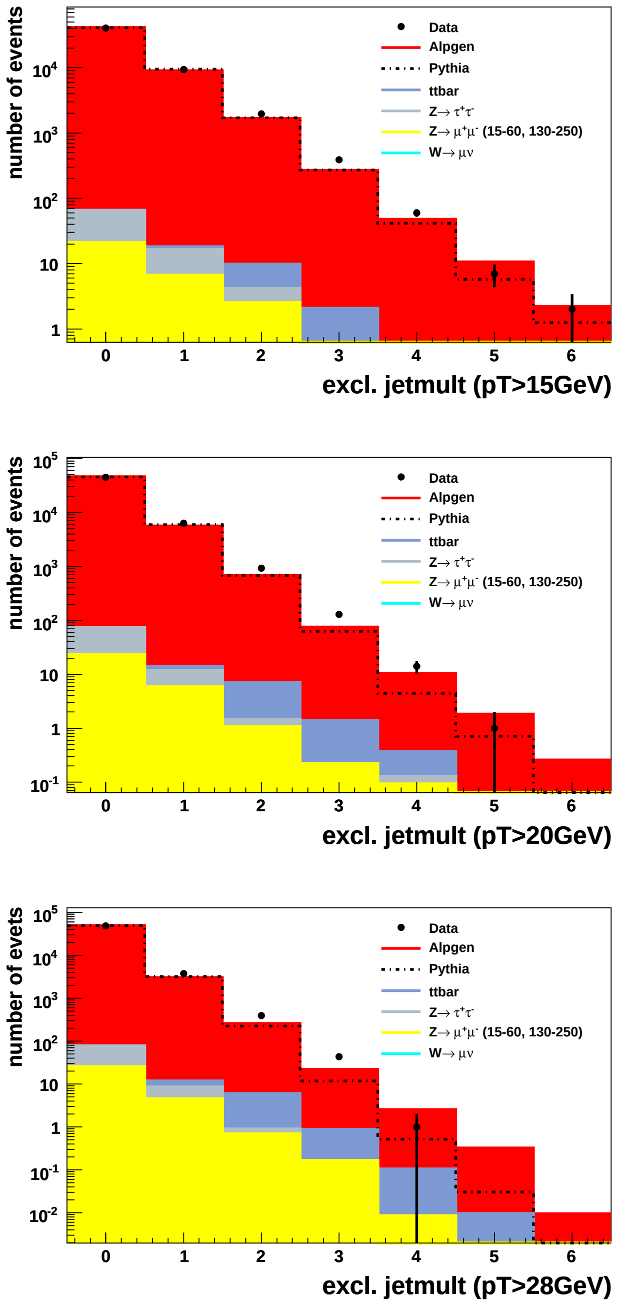

Figure 4.7: Exclusive jet multiplicity at reconstruction level for jets with $p_T(\text{jet}) > 15\,\text{GeV}$, jets with $p_T(\text{jet}) > 20\,\text{GeV}$ and jets with $p_T(\text{jet}) > 28\,\text{GeV}$ compared to the predictions of Alpgen and Pythia.

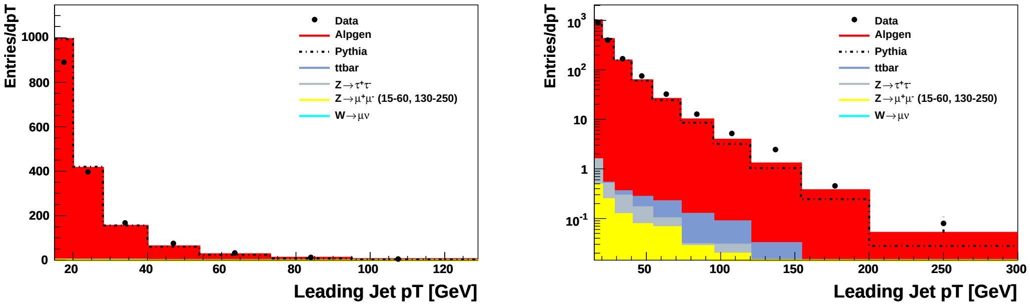

Figure 4.8: p_T spectrum of the leading jet at reconstruction level compared to predictions of ALPGEN and PYTHIA.

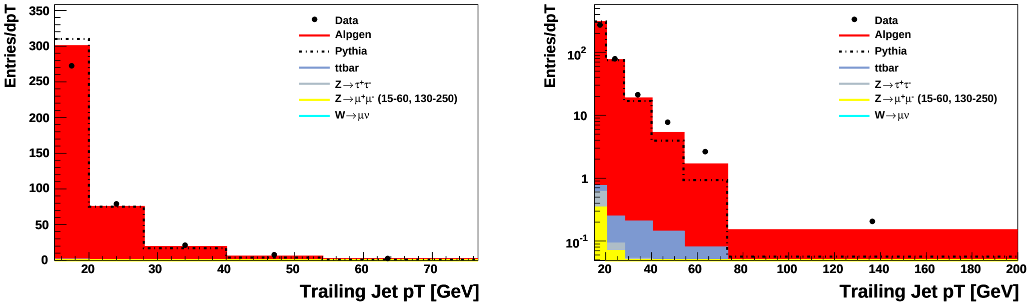

Figure 4.9: p_T spectrum of the trailing jet at reconstruction level compared to predictions of ALPGEN and PYTHIA.

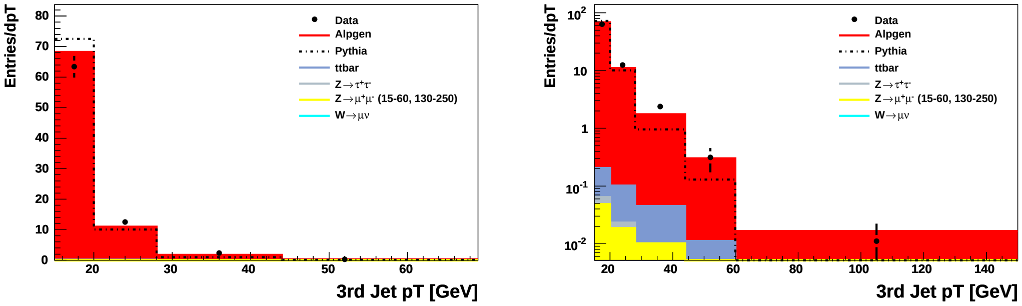

Figure 4.10: p_T spectrum of the third leading p_T(jet) at reconstruction level compared to predictions of ALPGEN and PYTHIA.

5 Measurement of Z Boson+jets differential production cross sections

The differential cross section $d\sigma/dx$ of a variable x is given by a distribution $f(x)$. Integrating over the differential cross section gives the total cross section σ.

$$\sigma = \int \frac{d\sigma}{dx} dx = \int f(x) dx \tag{5.1}$$

The integrated luminosity $\mathcal{L}$ relates the total cross section to the number of events.

$$N = \mathcal{L} \cdot \sigma \tag{5.2}$$

5.1 Determining the inclusive $Z/\gamma^* \rightarrow \mu^+\mu^-$ cross section

The ALPGEN sample (and later as a cross-check also the PYTHIA sample) is used to define the acceptance and efficiency. The inclusive $Z/\gamma^* \rightarrow \mu^+\mu^-$ production cross section times branching fraction into muons in the mass range $65 - 115\,\mathrm{GeV}$ is determined according to Equation 5.2:

$$\sigma \cdot BR(\mathrm{Z}/\gamma^* \rightarrow \mu^+\mu^-) = \frac{\mathrm{N_{obs}} - \mathrm{N_{bgd}}}{\mathrm{A} \cdot \mathcal{L}}$$

where N_{obs} is the number of observed signal events in data and N_{bgd} the number of expected background events which is assumed to be negligible small (see Section 4.6). A includes the detector acceptance and reconstruction efficiency and $\mathcal{L}$ is the integrated luminosity. A total of 52330 candidate events are selected from data, giving a statistical uncertainty of 0.4%. The integrated luminosity is $\mathcal{L} \approx 1046\,\mathrm{pb}^{-1}$. A systematic uncertainty on the integrated luminosity of 6.1% [50] is assumed. The product of detector acceptance and reconstruction efficiency is derived from Monte Carlo given by the ratio of all reconstructed and efficiency corrected events to all generated events inside the particle level mass range $65 - 115\,\mathrm{GeV}$. Calculating this value from the Pythia Monte Carlo samples gives a value of 0.2022 calculating A using the Alpgen samples gives a value of 0.2036. Choosing a value of $0.2029 \pm 1\%$ for the acceptance and reconstruction efficiency and assuming a muon reconstruction, trigger and ID uncertainty of 5% leads to an estimated cross section times branching fraction into muons of about:

$$\sigma_{\mathrm{Z}\rightarrow\mu^+\mu^-} = 246.8 \pm 1(stat.) \pm 12(syst.) \pm 15(lumi)\mathrm{pb} \tag{5.3}$$

As a cross-check this result of 246.8pb is compared with the expected cross section for Z/γ^* in this mass range of $252^{+5}_{-12}\,\mathrm{pb}$ [45]. Both values are in good agreement which demonstrates that the efficiencies (including corrections) are well understood.

The cross section for $Z \rightarrow \mu^+\mu^-$ with mass $65 - 115\,\mathrm{GeV}$ and restricted to muons with $|\eta| < 1.7$ was also estimated and found to be:

$$\sigma_{\mathrm{Z}\rightarrow\mu^+\mu^-} = 120.8 \pm (stat.) \pm 6(syst.) \pm 7(lumi)\mathrm{pb} \tag{5.4}$$

Since the final measurements of the Z boson + jets differential production cross sections will be either normalised to the inclusive cross section or to 1, all effects which are uncorrelated to the jet transverse momenta will cancel.

5.2 Unfolding methods

Given an ideal detector one could measure the quantity x of equation 5.1 in every event. But due to imperfections in the measurement, e.g. smearing effects caused by the limited detector resolution or the limited acceptance, distributions of the reconstructed variables differ from the true distributions. Unfolding the observed distributions from these distortions and exctracting the true distribution requires a knowledge of the overall effect of the distortions on the true quantity x.
The relationship between the measured distribution $g(y)$ of the measured quantity y, the true distribution $f(x)$ of the true variable x and a background contribution $b(y)$ can be expressed in terms of a response (resolution) function $A(x, y)$ which represents the detector effects.

$$g(y) = \int A(x, y) f(x) dx + b(y) \tag{5.5}$$

For a fixed value $x = x_0$ the resolution function $A(x, y)$ describes the response of the detector in the variable y. Determining the distribution $f(x)$ from a measured distribution $g(y)$ is called unfolding. With f, g and b represented by histograms with finite bin size, f having m bins and g and b having n bins, Equation 5.5 can be written as

$$g = Af + b$$

where A is a $n \times m$ matrix, containing values between 0 and 1. The elements of the response matrix A can be interpreted as the probability of an event generated in the i^{th} bin of the true distribution ending up in the j^{th} bin of the reconstructed distribution. In practice, the matrix inversion for given g and A (A can be found from Monte Carlo simulations),

$$f = A^{-1}g - b$$

which gives the solution f, leads to unstable and oscillating solutions.

Two methods, an iterative *bin-by-bin* correction and a method based on regularized unfolding are used to derive the true distribution f and measure the differential cross section for the leading[1], second (trailing) leading and third leading jet as function of transverse momentum and the jet multiplicity. For the stability of both methods and as they neglect the statistics of the simulated samples in the errors given, it is important to have much more Monte Carlo events than data events.

5.2.1 Iterative bin-by-bin correction

The *bin-by-bin* correction method can be applied if the amount of migration from one bin to another bin is not too large and if the bin widths are at least of the size of the resolution. Otherwise the this method should not be applied due to the large off-diagonal elements. The *bin-by-bin* correction method is based on a scale factor ϵ_{i}, calculated from Monte Carlo, which corrects the data in each bin i. The values of ϵ_{i} are given by the ratio:

$$\epsilon_{\mathrm{i}} = \frac{\text{number of reconstructed events in bin i}}{\text{number of generated events in bin i}}$$

In the case of small bin to bin migrations this method resembles the standard matrix unfolding procedure with a diagonal matrix. In this analysis the *bin-by-bin* correction method is applied iteratively, which takes implicitly off-diagonal terms into account. I.e. after obtaining correction factors using the Monte Carlo that describes the data best, the factors are applied to the data and the detector simulation is repeated using the corrected function as new input. This leads to new correction factors for the data. Further iterations are carried out until the additional correction vanishes.

---

[1] in this context leading denotes the jet with the highest transverse momentum

5.2.2 Regularized unfolding

The method of regularized unfolding [51, 52] takes all correlations into account and uses the full migration matrix. It is essential if there are larger effects of transformation and finite resolution. The response function contains all effects of the measurement, including limited acceptance and transformation effects. Regularized unfolding is performed using the program *Run* [52]. The resolution function A is implicitly defined by Monte Carlo data which are given together with data as input to the program. A maximum likelihood fit including a regularization term is used to smooth unwanted oscillations in the unfolding. The result of the unfolding is represented by B-splines[2]. In contrast to the *bin-by-bin* correction method matching between the jets at particle level and at reconstruction level is required to pass the correct detector response function to the unfolding program.

5.3 Unfolding the leading, second leading and third leading p_T(jet)

In order to determine particle level cross sections, the measured data distributions need to be corrected for event migrations due to the finite resolution of the detector. Whereas the *bin-by-bin* correction method is used to derive the final results the regularized unfolding method is only used as a cross-check. The correction factors are determined using the ALPGEN Monte Carlo samples. The PYTHIA Monte Carlo samples are used to cross-check the derived results.
The measured differential cross section $d\sigma/dp_T$ is obtained by calculating the cross section in each bin of p_T(jet) with the following formula:

$$\left(\frac{\Delta\sigma}{\Delta p_T}\right)_i = \frac{N_i}{\Delta_i \cdot A_i \cdot \int L dt} \tag{5.6}$$

N_i denotes the number of measured events in bin i and Δ_i the corresponding width in p_T(jet) . The acceptance correction A_{i} includes the correction for the truth and reco level Z acceptance and the correction for the i^{th} reco level jet to be matched to the i^{th} particle jet. All correction factors are given as event weights to the unfolding programs.

---

[2] B-Spline functions are formed by joining polynomials of degree four together at fixed points called knots. At the breakpoints the polynomials are required to join smoothly.

5.3.1 Matching of reconstructed jets with particle jets

The matching between particle level jets and calorimeter jets is done in the $\eta - \phi$ plane by requiring the distance ΔR between the two objects to be less than 0.5. Figure 5.1 shows the distance between all possible combinations of jets at reconstruction and particle level. The efficiency to associate a reconstructed jet with a particle jet is found to be about $\sim 90\%$. The inefficiency of $\sim 10\%$ can be due to additional jets from minimum bias events not associated to the Z boson. To pass the correct detector response function to the regularized unfolding program, only events where the i^{th} reconstructed jet is matched to the i^{th} particle jet with a transverse momentum greater than 15 GeV are used to describe the detector function. Reconstructed jets with transverse momenta less then 15 GeV are not sufficiently understood. Mismatching between reconstructed jets and jets on particle level can be due to the leading particle jet not being reconstructed, changes in the jet ordering due to resolution effects or the associated particle jet has a transverse momentum less than 15 GeV. Figures 5.2, 5.3 and 5.4 shows the amount of not correctly matched jets for the leading, second leading and third leading p_T(jet) respectively. The fraction of all 'mismatched' jets is dominated by reconstructed jets associated with a particle jet with $p_T\text{(jet)} < 15\,\text{GeV}$ and found to be about 38% for the leading p_T(jet), 67% for the trailing p_T(jet) and about 83% for the third leading p_T(jet).
In contrast to the regularized unfolding the iterative *bin-by-bin* correction method does not require that the i^{th} reconstructed jet is matched to the i^{th} particle jet. Assuming that the detector acceptance and the energy resolution is the same in data and simulation a mismatching between generated and reconstructed jets is not a problem.

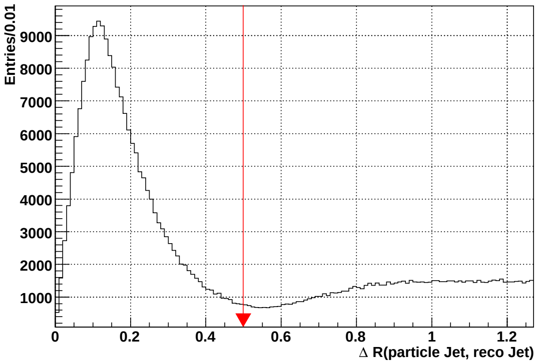

Figure 5.1: Distance ΔR between all possible combinations of particle jets ($p_T > 6\,\text{GeV}$) and reconstructed jets ($p_T > 15\,\text{GeV}$)

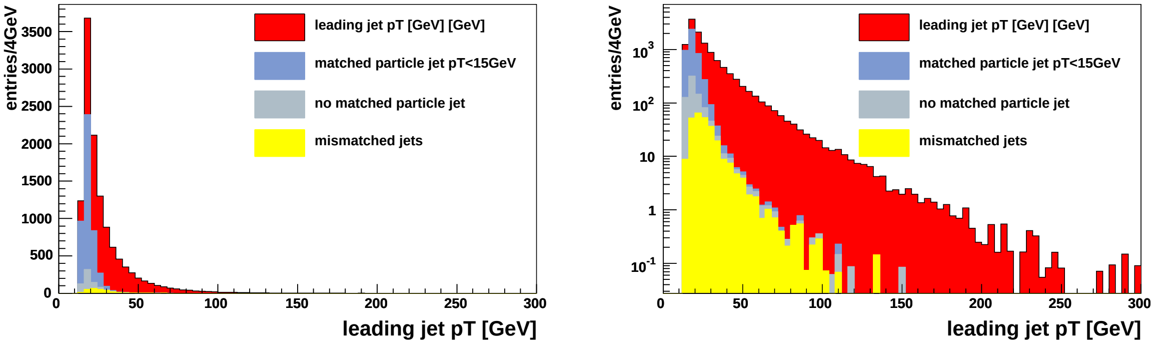

Figure 5.2: p_T spectrum of the leading jet including the different types of incorrectly matched jets. Shown is the contribution of correctly matched jets (red), the contribution of matched particle jets with p_T(jet)$<$ 15 GeV (blue), the contribution of not matched particle jets (light blue) and the contribution of mismatched jets (yellow).

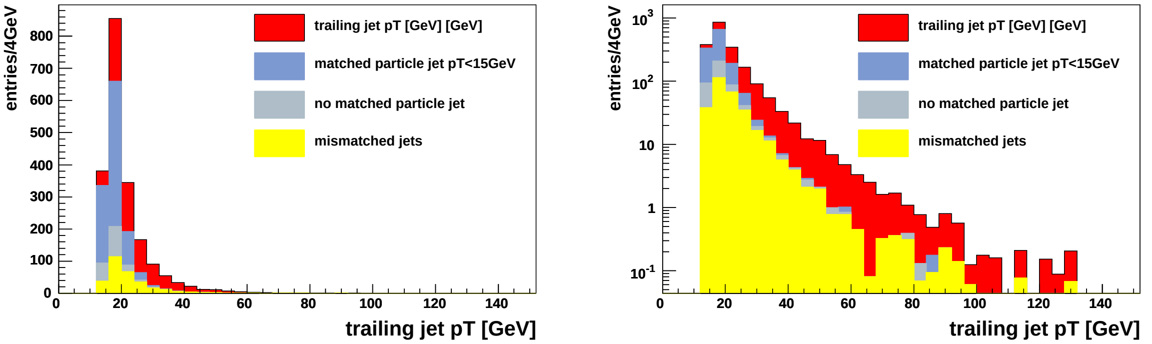

Figure 5.3: p_T spectrum of the trailing jet including the different types of incorrectly matched jets. Shown is the contribution of correctly matched jets (red), the contribution of matched particle jets with p_T(jet)$<$ 15 GeV (blue), the contribution of not matched particle jets (light blue) and the contribution of mismatched jets (yellow).

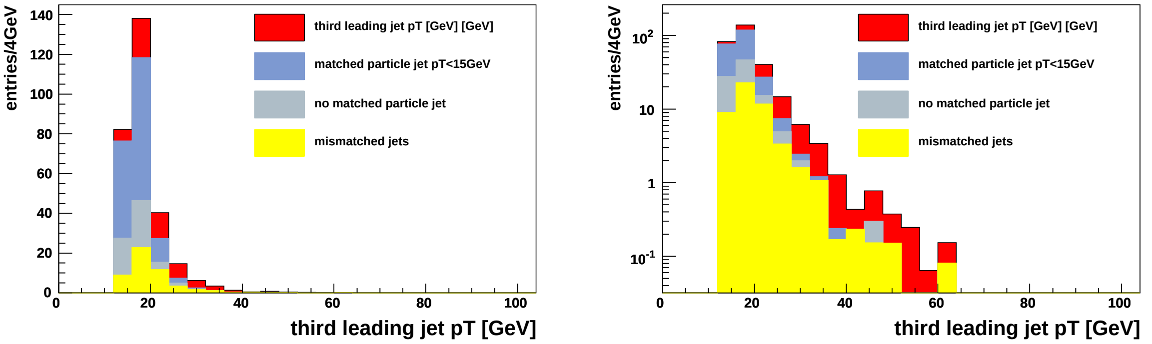

Figure 5.4: p_T spectrum of the third leading jet including the different types of incorrectly matched jets. Shown is the contribution of correctly matched jets (red), the contribution of matched particle jets with p_T(jet)$<$ 15 GeV (blue), the contribution of not matched particle jets (light blue) and the contribution of mismatched jets (yellow).

5.3.2 Choice of binning in p_T(jet)

In order to minimize the errors in the unfolded and *bin-by-bin* corrected results the bin sizes in the true and measured variables are adjusted to match the experimental resolution and statistics. The upper bin limits for p_T(jet) were selected so that all accepted Monte Carlo and data events fit within the range. The lower bin limit is set to 28 GeV. Two additional bins between 15 GeV and 28 GeV are added to control and constrain the migrations from low p_T-jets into the measurement region ($p_T(\text{jet}) > 28\,\text{GeV}$). The unfolded data in these two additional bins are not reported in the final result as the migration into these bins from jets with reconstructed $p_T < 15\,\text{GeV}$ is not constrained. Tables 5.1, 5.2 and 5.3 show the migration matrizes obtained by using ALPGEN Monte Carlo for the leading, second leading and third leading p_T(jet) respectively. The matrix coefficient ij is defined as the fraction of events, that are generated in bin i and reconstructed in bin j. Due to the decreasing spectrum of the jet transverse momenta, the migration from bins with lower p_T(jet) is larger than the migration from bins with higher p_T(jet) . The bin boundaries are selected in such a way that the bin purity defined as the fraction of events, that are generated and reconstructed in the same bin of p_T(jet) is about 50% or larger.
To measure the leading p_T(jet) spectrum the range $28\,\text{GeV} < p_T(\text{jet}) < 300\,\text{GeV}$ is binned in 8 bins of increasing width. The bin boundaries were choosen to be:
$\{28\,\text{GeV}, 40\,\text{GeV}, 54\,\text{GeV}, 73\,\text{GeV}, 95\,\text{GeV}, 120\,\text{GeV}, 154\,\text{GeV}, 184\,\text{GeV}\text{and}\,300\,\text{GeV}\}$.
To unfold the trailing p_T(jet) 4 bins between $28\,\text{GeV} < p_T(\text{jet}) < 200\,\text{GeV}$ with the following bin limits were selected:
$\{28\,\text{GeV}, 40\,\text{GeV}, 54\,\text{GeV}, 73\,\text{GeV}\text{and}\,200\,\text{GeV}\}$.
Three bins between $28\,\text{GeV} < p_T(\text{jet}) < 150\,\text{GeV}$ were selected to measure the third leading p_T(jet) distribution: $\{28\,\text{GeV}, 44\,\text{GeV}, 60, \text{GeV}\text{and}\,150\,\text{GeV}\}$.

		generated									
	Bin [GeV]	15-20	20-28	28-40	40-54	54-73	73-95	95-120	120-154	154-184	184-300
reconstructed	15-20	0.60	0.35	0.05	0.00	0.00	0.00	0.00	0.00	0.00	0.00
	20-28	0.34	0.46	0.19	0.01	0.00	0.00	0.00	0.00	0.00	0.00
	28-40	0.07	0.29	0.49	0.13	0.01	0.00	0.00	0.00	0.00	0.00
	40-54	0.01	0.03	0.32	0.51	0.13	0.00	0.00	0.00	0.00	0.00
	54-73	0.00	0.00	0.03	0.31	0.55	0.11	0.00	0.00	0.00	0.00
	73-95	0.00	0.00	0.00	0.02	0.33	0.53	0.10	0.00	0.00	0.00
	95-120	0.00	0.00	0.00	0.00	0.01	0.35	0.53	0.10	0.00	0.00
	120-154	0.00	0.00	0.00	0.00	0.00	0.02	0.33	0.54	0.10	0.01
	154-184	0.00	0.00	0.00	0.00	0.00	0.00	0.04	0.28	0.50	0.19
	184-300	0.00	0.00	0.00	0.00	0.00	0.00	0.00	0.00	0.14	0.85

Table 5.1: The migration matrix M for the p_T spectrum of the leading jet. The columns j denote the generated bins and the lines i the reconstructed bins. M_{ij} is the fraction of events generated with a true p_T(jet) in bin i which are reconstructed with a p_T(jet) in bin j.

		generated					
	Bin [GeV]	15-20	20-28	28-40	40-54	54-73	73-200
reconstructed	15-20	0.61	0.34	0.05	0.00	0.00	0.00
	20-28	0.33	0.46	0.20	0.01	0.00	0.00
	28-40	0.06	0.26	0.52	0.15	0.01	0.00
	40-54	0.00	0.02	0.28	0.52	0.17	0.01
	54-73	0.00	0.00	0.03	0.29	0.56	0.13
	73-200	0.00	0.00	0.00	0.00	0.19	0.80

Table 5.2: The migration matrix M for the p_T spectrum of the trailing jet. The columns j denote the generated bins and the lines i the reconstructed bins. M_{ij} is the fraction of events generated with a true p_T(jet) in bin i which are reconstructed with a p_T(jet) in bin j.

		generated				
	Bin [GeV]	15-20	20-28	28-44	44-60	60-150
reconstructed	15-20	0.67	0.30	0.03	0.00	0.00
	20-28	0.35	0.48	0.17	0.00	0.00
	28-44	0.06	0.25	0.59	0.09	0.01
	44-60	0.01	0.01	0.29	0.56	0.13
	60-150	0.01	0.00	0.05	0.20	0.74

Table 5.3: The migration matrix M for the p_T spectrum of third leading jet. The columns j denote the generated bins and the lines i the reconstructed bins. M_{ij} is the fraction of events generated with a true p_T(jet) in bin i which are reconstructed with a p_T(jet) in bin j.

5.3.3 Closure tests

Two different closure tests are performed to test the regularized unfolding and the *bin-by-bin* correction method before applying it to data. The first test uses fully simulated PYTHIA samples which were treated as pseudo-data and ALPGEN to define the migration matrix. In the second closure test in addition a reweighted ALPGEN distribution is used as input for the migration matrix while keeping the same PYTHIA sample as pseudo-data. For this purpose the p_T(jet) distribution is shifted by 3 GeV. The corrected distributions obtained with the closure tests are compared to the particle jet spectrum generated with PYTHIA to demonstrate that the original distribution can be recovered and that the result has only a minor dependence on the distribution used to define the migration matrix.

Figures 5.5 and 5.6 show the results of the described closure tests for the leading p_T(jet) distribution using the two different correction methods. The unfolded distributions are in good agreement with the true values within the statistical errors. The shaded region includes the two additional bins between 15 GeV and 28 GeV which are added to control and constrain the migrations from low p_T-jets into the measurement region.

The lower part of the figures displays the ratio between the two unfolding methods and the true spectrum and the ratio between the two unfolding methods themselves. The results of the *bin-by-bin* correction are in good agreement with the true values generated using PYTHIA and with the results obtained by the regularized unfolding method within the statistical errors.

The results of the closure tests for the leading, trailing and third leading p_T(jet) using the *bin-by-bin* correction procedure are displayed in Figure 5.7. Good agreement is achieved for all distributions.

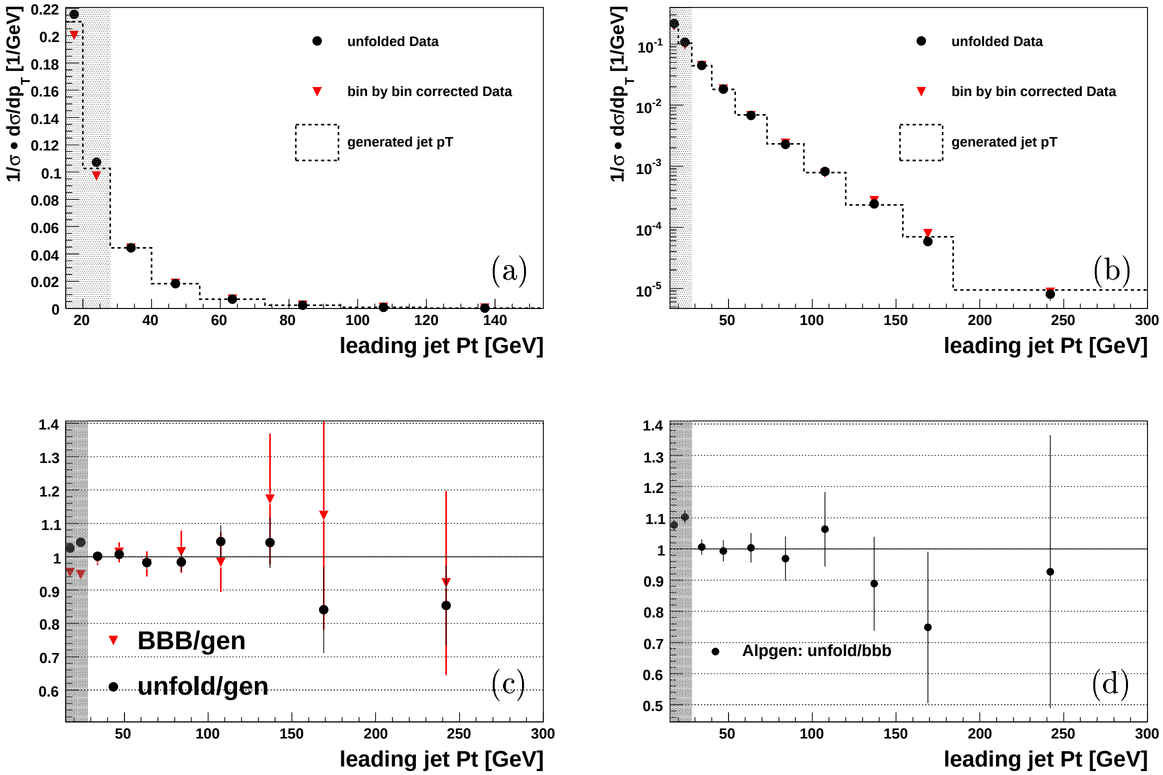

Figure 5.5: Closure test for the p_T spectrum of the leading jet: (a) and (b) Unfolded (black dots) and *bin-by-bin* corrected (red triangles) p_T spectrum of the leading jet using PYTHIA as data and ALPGEN to define the migration matrix compared to the particle jet spectrum (histogram). The results are normalised to the cross section integrated for $p_T(\text{jet}) > 28\,\text{GeV}$. (c) Ratio between the unfolded distribution of the p_T of the leading jet and the generated particle jet spectrum (black dots) and the ratio between the *bin-by-bin* corrected p_T distribution of the leading jet and the particle jet distribution (red triangles). (d) Ratio between the unfolded and *bin-by-bin* corrected p_T spectrum of the leading jet. Errors shown are statistical only. The shaded region includes the two additional bins between 15 GeV and 28 GeV which are not meant as measurement.

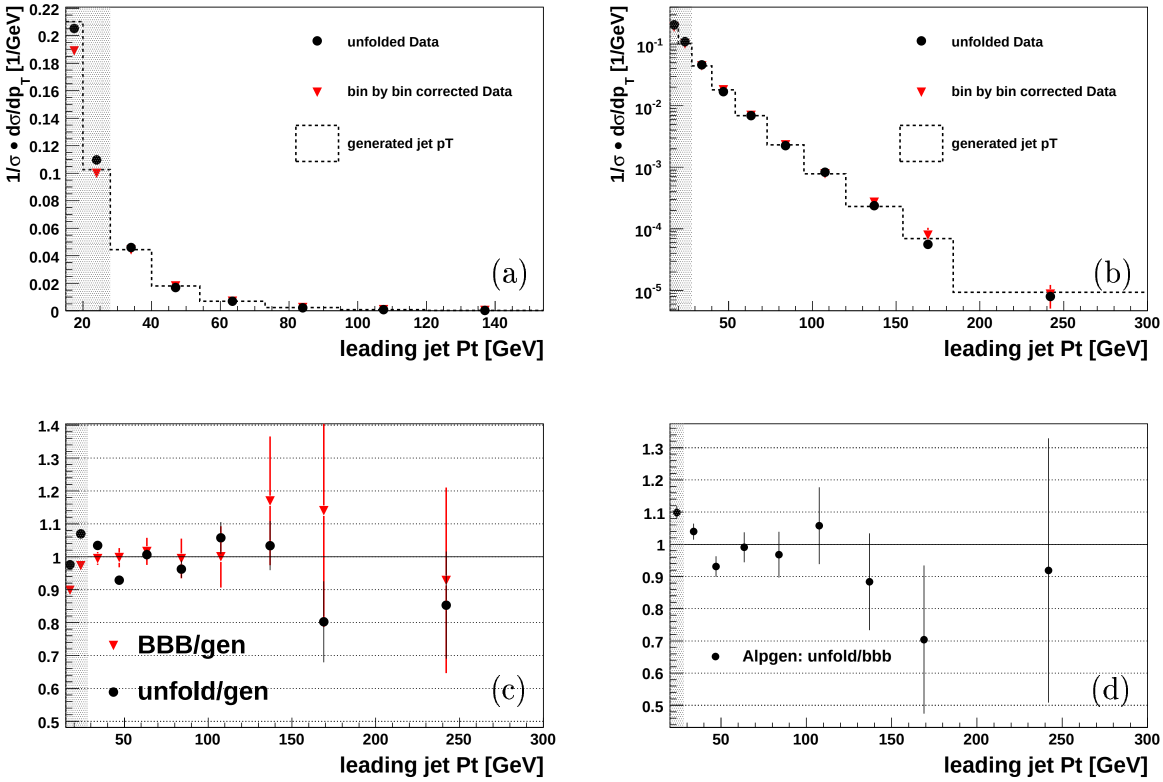

Figure 5.6: Closure test of the unfolding and *bin-by-bin* correction procedure for the p_T spectrum of the leading jet using a reweighted ALPGEN distribution to define the migration matrix. The results are normalised to the cross section integrated for $p_T(\text{jet}) > 28\,\text{GeV}$. (a) and (b) Unfolded (black dots) and *bin-by-bin* corrected (red triangles) p_T spectrum of the leading jet using PYTHIA as data and ALPGEN to define the migration matrix compared to the particle jet spectrum (histogram) generated with PYTHIA. (c) Ratio between the unfolded distribution of the p_T of the leading jet and the generated particle jet spectrum (black dots) and the ratio between the *bin-by-bin* corrected p_T distribution of the leading jet and the particle jet distribution (red triangles). (d) Ratio between the unfolded and *bin-by-bin* corrected p_T spectrum of the leading jet. Errors shown are statistical only. The shaded region includes the two additional bins between 15 GeV and 28 GeV which are not meant as measurement.

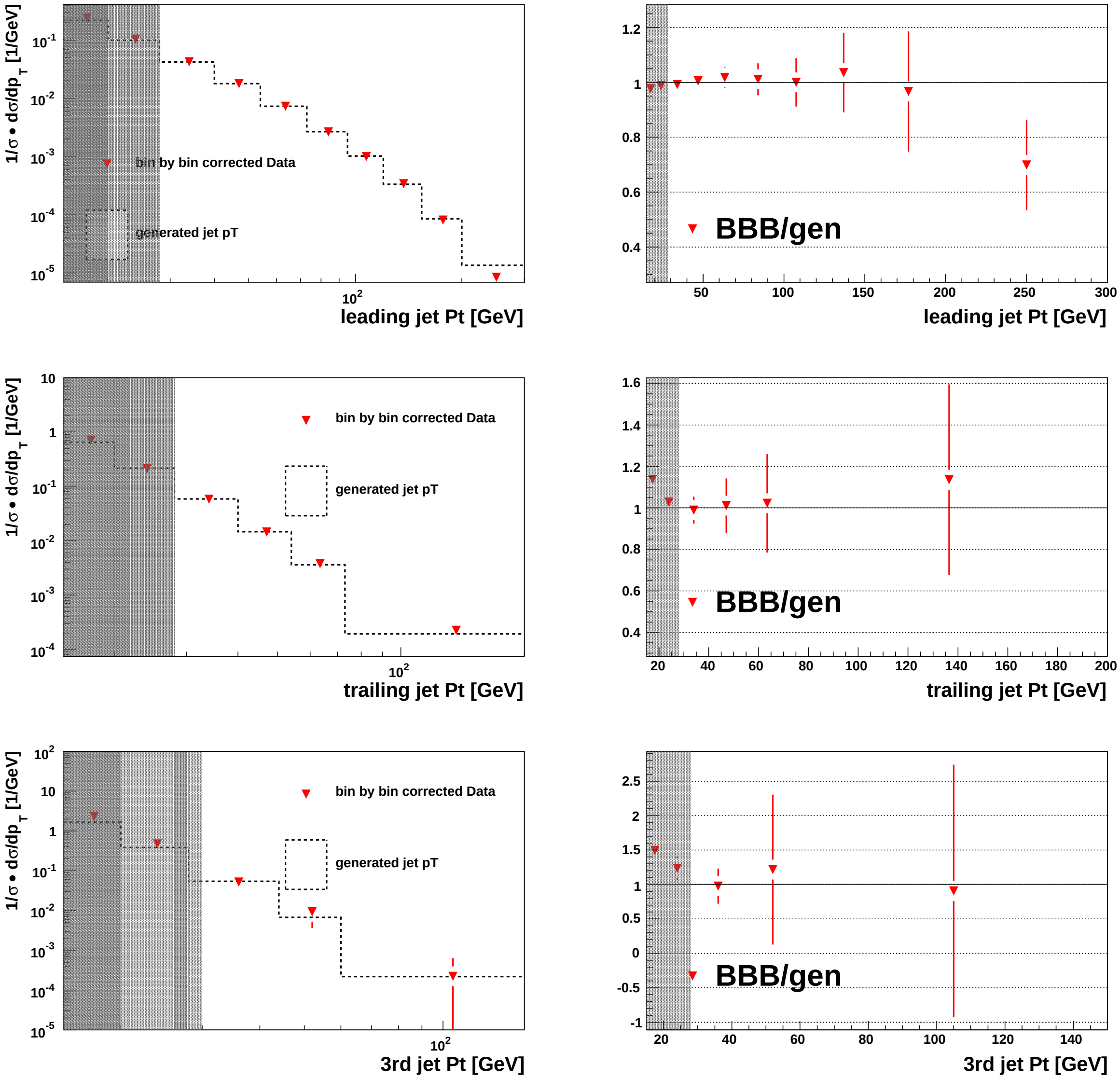

Figure 5.7: Closure tests for the distributions of the leading (top), trailing (middle) and third leading (bottom) p_T jet: Left plots: *bin-by-bin* corrected p_T spectrum of the i^{th} leading jet using Pythia as data and Alpgen to define the migration matrix compared to the particle jet spectrum (histogram). The results are normalised to the cross section integrated for $p_T(\text{jet}) > 28\,\text{GeV}$. Right plots: Ratio between the *bin-by-bin* corrected spectrum of the p_T of the i^{th} leading jet and the particle jet distribution (red triangles) generated using Pythia. Errors shown are statistical only. The shaded region includes the two additional bins between 15 GeV and 28 GeV which are not meant as measurement.

5.3.4 Systematic uncertainties on the cross section measurement

Different systematic uncertainties are taken into account. They are estimated using the simulation by varying a specific uncertainty at a time while keeping the other quantities fixed. The systematic errors are added in quadrature to give the total uncertainty.

Jet uncertainties

Four types of jet systematic errors are taken into account: from the uncertainty on the jet energy scale in data and simulation, on the jet resolution and on the jet efficiency. The error due to the jet energy scale is one of the major uncertainties of the measurement. It is estimated by varying the absolute jet energy scale (described in Section 4.1.2) correction up and down by 1σ in data and Monte Carlo. The jet reconstruction efficiency is varied by one standard deviation in both directions and the jet resolution is shifted by $\pm\sigma$ to account for this uncertainty. A detailed description of these errors can be found in Reference [49]. Figure 5.8 shows a comparison between the different uncertainties due to the jet systematics for the measurement of the leading p_T(jet) . The errors due to the jet energy scale are the dominant errors. The fluctuations for p_T(jet) values larger than 120 GeV can be attributed to the low statistic in this region.

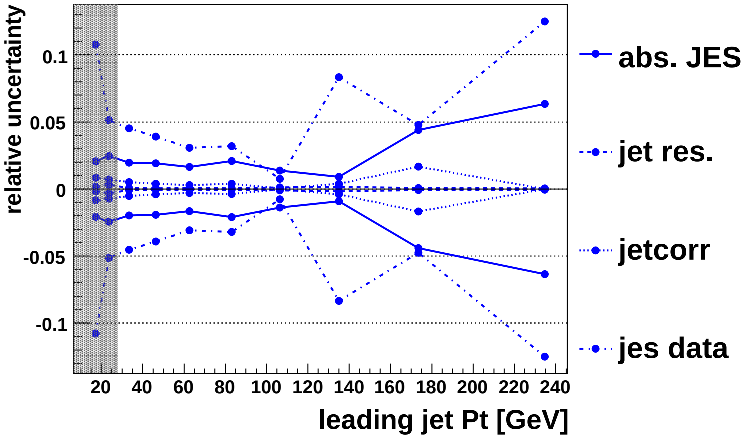

Figure 5.8: Relative uncertainties in the measurement of the leading jet p_T due to jet systematics; abs. JES and jes data show the impact of a 1σ shift of the jet energy scale in Monte Carlo and data, jet res. the impact of the variation of the jet resolution inside its error and jetcorr the impact of a 1σ shift of the jet reconstruction efficiency.

Uncertainty on acceptance due to the precision of the PDFs

The error due to the uncertainty in the parton distribution functions (PDFs) is evaluated using the `CTEQ6.1M` PDF error sets. The uncertainties are estimated from the deviations with respect to the central PDF, by reweighting the Monte Carlo generated using `CTEQ6L1` to each of the $40 + 1$ `CTEQ6.1M` distributions. The *bin-by-bin* correction procedure is than repeated 40 times finding the difference in the result. Positive and negative shifts are added seperately in quadrature to give the total error. The total PDF uncertainty varies from 2% at low p_T(jet) to 4% at high p_T(jet) .

Muon uncertainties

Relative uncertainties due to the error on the muon identification, isolation and tracking efficiencies are estimated by varying each value within its error. Figure 5.9 shows the relative uncertainties due to the muon systematics for the leading jet p_T which are approximately flat over the whole range of jet p_T and thus negligible after normalisation.

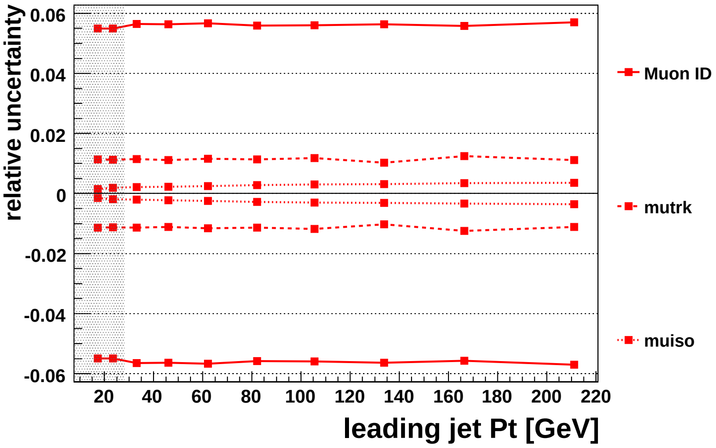

Figure 5.9: Relative uncertainties in the measurement of the leading jet p_T distribution due to muon systematics. Muon ID shows the impact of varying the muon identification efficiency within its error, mutrk shows the effect of varying the muon tracking efficiency within its error and muiso the effect of varying the isolation efficiency determined in Section 4.5 within its error.

Uncertainty due to the luminosity profile reweighting

The measurements depend on the precise determination of the jet multiplicities for each event. Additional jets can be produced in additional minimum bias interactions within the same bunch crossing (see also Section 3.4.2). As the probability for extra jet production depends on the instantaneous luminosity the luminosity profile used in the simulation needs to be reweighted to match the real distributions. This correction affects only the shape of the luminosity profile and not the overall normalisation. A limit for the event weight of 3 is set to limit statistical fluctuations. The error due to the luminosity profile reweighting is estimated by varying the upper limit for the maximal weight applied to an inidividual event from the default value 3.0 to 4.0 and 2.5.

Uncertainties due to the unfolding and the bin-by-bin correction

The uncertainties due to the unfolding method are taken into account by taking the diagonal elements from the covariance matrix of the result provided by RUN which includes also the statistical error. In addition the number of knots of the spline function and the number of degrees of freedom (ndf) which affects the amount of smoothing between the unfolded points have both been varied by ±1.
To estimate the error due to the *bin-by-bin* correction method the input reweighting factor for the first bin has been varied by the difference between the factors of the first and second bin. Also the reweighting factor for events with true $p_T(\text{jet}) < 15\,\text{GeV}$ for which no correction factor is defined has been varied between 1 and the correction factor of the first bin. An additional uncertainty is estimated by taking the difference between the *bin-by-bin* correction result after the last and next to last iteration.

Total systematic uncertainty

The total systematic uncertainty on the measurement of i^{th} jet p_T is given by the quadratic sum of all systematic uncertainties. The errors are symmetrized by taking the maximum shift. The uncertainty on the shape of the distribution is given by normalising all distributions to the cross section integrated for $p_T(\text{jet}) > 28\,\text{GeV}$. This reduces the systematic uncertainties. Figures 5.10, 5.11 and 5.12 summarize all different contributions to the total systematic uncertainty compared to the statistical error for the leading, trailing and third leading $p_T(\text{jet})$ distribution, respectively. The errors are displayed with three different normalisations: without normalisation, normalised to the measured inclusive cross section, as determined in Section 5.1 and normalised to the cross section integrated for $p_T(\text{jet}) > 28\,\text{GeV}$. When normalising the differential cross section to the measured inclusive cross section uncertainties which are independend on p_T(jet) as e.g. the uncertainty on the luminosity in the final measurement cancels. Normalising the result to the cross section integrated for $p_T(\text{jet}) > 28\,\text{GeV}$ corresponds to a measurement of the shape of the jet p_T distribution.

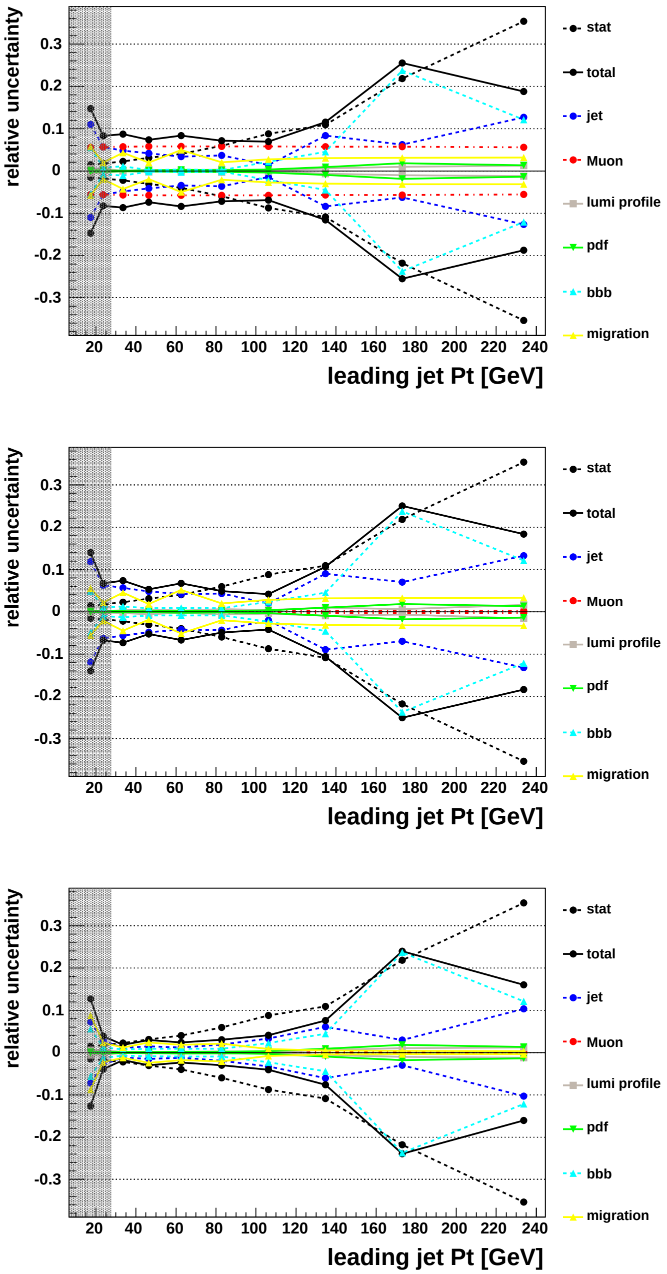

Figure 5.10: Combination of all relative uncertainties in the *bin-by-bin* corrected data for the differential cross section of the leading jet p_T: top: total uncertainties; middle: uncertainties after normalising the *bin-by-bin* corrected data to the measured inclusive cross section as determined in Section 5.1; bottom: uncertainties after normalising the data distribution to the cross section integrated for $p_T(\text{jet}) > 28\,\text{GeV}$. Shown are the statistical error (stat), the total uncertainty (total) and the individual sources to the total uncertainty: the error resulting from the jet uncertainties (jet), the error resulting from the muon uncertainties (Muon), the uncertainties resulting from the luminosity profile reweighting (lumi profile) and the PDF reweighting (pdf), respectively and the uncertainties due to the *bin-by-bin* correction procedure (bbb and migration). The fluctuations for $p_T(\text{jet})$ values larger than 120 GeV can be attributed to the low statistic in this region.

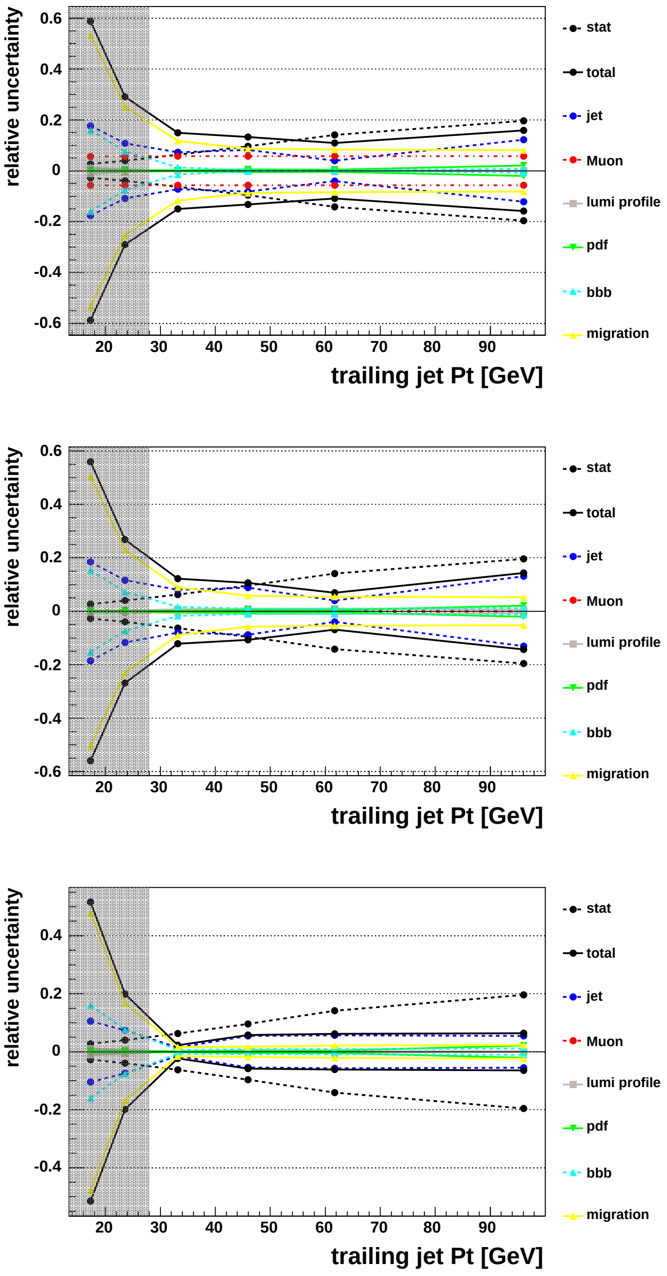

Figure 5.11: Combination of all relative uncertainties in the *bin-by-bin* corrected data for the differential cross section of the second leading jet p_T: top: total uncertainties; middle: uncertainties after normalising the *bin-by-bin* corrected data to the measured inclusive cross section as determined in Section 5.1; bottom: uncertainties after normalising the data distribution to the cross section integrated for $p_T(\text{jet}) > 28\,\text{GeV}$. Shown are the statistical error (stat), the total uncertainty (total) and the individual sources to the total uncertainty: the error resulting from the jet uncertainties (jet), the error resulting from the muon uncertainties (Muon), the uncertainties resulting from the luminosity profile reweighting (lumi profile) and the PDF reweighting (pdf), respectively and the uncertainties due to the *bin-by-bin* correction procedure (bbb and migration).

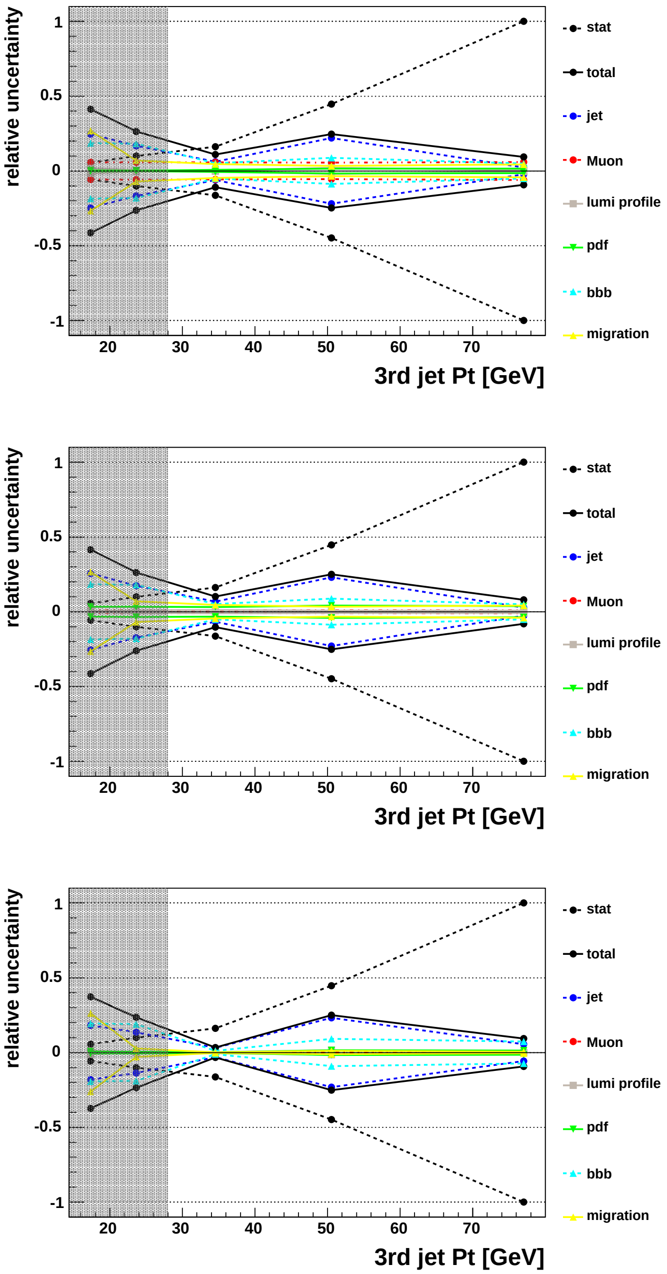

Figure 5.12: Combination of all relative uncertainties in the *bin-by-bin* corrected data for the differential cross section of the third leading jet p_T: top: total uncertainties; middle: uncertainties after normalising the *bin-by-bin* corrected data to the measured inclusive cross section as determined in Section 5.1; bottom: uncertainties after normalising the data distribution to the cross section integrated for $p_T(\text{jet}) > 28\,\text{GeV}$. Shown are the statistical error (stat), the total uncertainty (total) and the individual sources to the total uncertainty: the error resulting from the jet uncertainties (jet), the error resulting from the muon uncertainties (Muon), the uncertainties resulting from the luminosity profile reweighting (lumi profile) and the PDF reweighting (pdf), respectively and the uncertainties due to the *bin-by-bin* correction procedure (bbb and migration).

5.3.5 Choice of the bin centers

For the differential cross section measurement the central value of the bins in jet p_T are choosen following the prescription of Lafferty and Wyatt [53]. The center of the bin is converted to the value of p_T(jet) at which the value of the predicted function $g(x)$ is equal to its mean value g_{meas} over the bin. This value of p_T(jet) is defined by:

$$g(x_{\text{lw}}) = \frac{1}{\Delta x} \int_{x_2}^{x_1} g(x)dx \tag{5.7}$$

The unknown function $g(x)$ is predicted by a function $f(x)$ that gives a reasonable approximation in shape to the true function $g(x)$.

5.3.6 Measurement of the differential production cross section $\frac{\mathrm{d}\sigma}{\mathrm{d}p_\mathrm{T}(\mathrm{jet}_1)}$ as function of the leading jet p_T

Three iterations are carried out to correct the p_T spectrum of the leading jet using the *bin-by-bin* correction method. The ratios between the corrected spectra at iteration i and at iteration $i-1$ which show the convergence of the method are displayed in Figure 5.13. For $p_T(\mathrm{jet}) > 130\,\mathrm{GeV}$ the iteration is not converging due to an excess in data which can be seen in Figure 4.8. This discrepancy from 1 for the 3^{rd} iteration is covered by the systematic uncertainty. The result of the fully unfolded leading jet p_T spectrum compared to the *bin-by-bin* correction result is displayed in Figure 5.14. Statistical and systematic errors are included. The result is normalised to the measured inclusive cross section and normalised to the cross section integrated for $p_T(\mathrm{jet}) > 28\,\mathrm{GeV}$. This cancels uncertainties which do not correlate with this observable. The cross section is given w.r.t. to the limited muon acceptance (muon $|\eta| < 1.7$ and no cut on the muon transverse momentum) as determined in section 5.1. The jets at hadron level are defined using the `D0RunIICone` algorithm with a cone size of $R = 0.5$. For comparison the predictions of ALPGEN and PYTHIA are included. A summary of the values and errors is also given in Table 5.4. The result for the p_T range between 20 and 28 GeV are shown in the table, although they are not included in the final measurement as the migration from particle jets with $p_T < 15\,\mathrm{GeV}$ into this region is is not sufficiently constrained (see section 5.3.2).

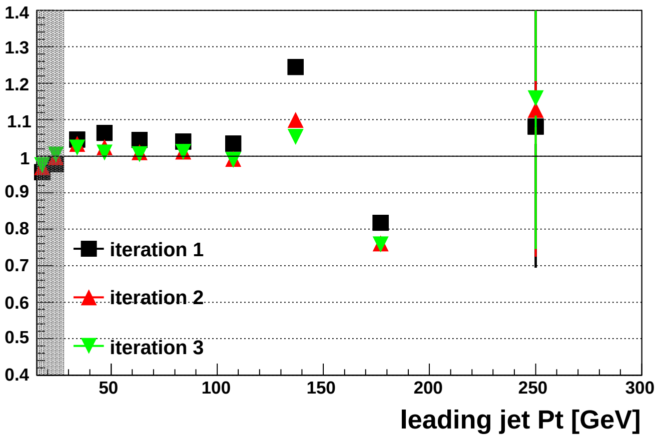

Figure 5.13: Ratio between the *bin-by-bin* corrected spectrum at iteration i and the *bin-by-bin* corrected distribution at iteration $i-1$.

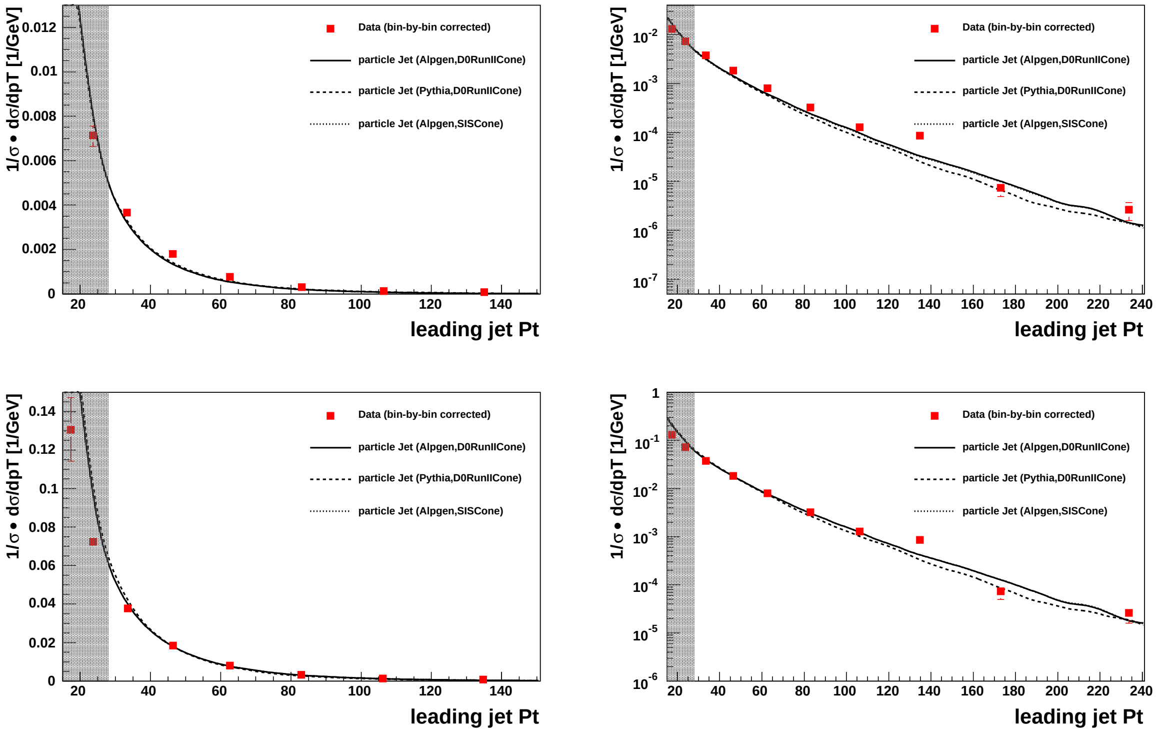

Figure 5.14: *Bin − by − bin* corrected (red quadrats) p_T distribution of the leading jet compared to the particle jet spectrum of ALPGEN (solid line) and PYTHIA (dotted line). The errors represent the combined statistical and systematic uncertainties. Top: the result is normalised to the measured inclusive cross section ($\sigma_{\text{incl}} = 120.8\,\text{pb}$) for muons with $|\eta| < 1.7$ as determined in Section 5.1; bottom: the result is normalised to the cross section integrated for $p_T(\text{jet}) > 28\,\text{GeV}$.

p_T jet range [GeV]	mean p_T [GeV]	# of events	#of bgd. events	$N \cdot \frac{d\sigma}{dpT(jet)}$ [1/GeV]	err_{stat} [%]	err_{sys} [%]
				$N = 1 \cdot fb^{-1}$		
20 - 28	23.7	3175	4.5	$8.70e+02$	1.8	8.3
28 - 40	33.5	2013	4.4	$4.54e+02$	2.2	8.7
40 - 54	46.4	1048	3.9	$2.22e+02$	3.1	7.4
54 - 73	62.6	617	4.3	$9.64e+01$	4.0	8.4
73 - 95	82.9	282	2.7	$3.87e+01$	6.0	7.2
95 - 120	106.2	130	2.2	$1.53e+01$	8.8	6.9
120 - 154	134.7	84	1.1	$1.03e+01$	10.9	11.6
154 - 200	173.0	21	0.3	$8.82e-01$	21.8	25.5
200 - 300	233.7	8	0.1	$3.15e-01$	35.4	18.8
				$N = \frac{1}{\sigma_{incl,\lvert\eta\rvert<1.7}}$		
20 - 28	23.7	3175	4.5	$7.25e-03$	1.8	6.7
28 - 40	33.5	2013	4.4	$3.78e-03$	2.2	7.3
40 - 54	46.4	1048	3.9	$1.85e-03$	3.1	5.3
54 - 73	62.6	617	4.3	$8.03e-04$	4.0	6.7
73 - 95	82.9	282	2.7	$3.23e-04$	6.0	4.9
95 - 120	106.2	130	2.2	$1.28e-04$	8.8	4.2
120 - 154	134.7	84	1.1	$8.56e-05$	10.9	10.6
154 - 200	173.0	21	0.3	$7.35e-06$	21.8	25.0
200 - 300	233.7	8	0.1	$2.62e-06$	35.4	18.4
				$N = \frac{1}{\sigma_{jet_{pt}>28\,\mathrm{GeV}}}$		
20 - 28	23.7	3175	4.5	$7.23e-02$	1.8	3.9
28 - 40	33.5	2013	4.4	$3.77e-02$	2.2	1.8
40 - 54	46.4	1048	3.9	$1.84e-02$	3.1	3.0
54 - 73	62.6	617	4.3	$8.01e-03$	4.0	2.4
73 - 95	82.9	282	2.7	$3.22e-03$	6.0	3.0
95 - 120	106.2	130	2.2	$1.27e-03$	8.8	4.1
120 - 154	134.7	84	1.1	$8.53e-04$	10.9	7.6
154 - 200	173.0	21	0.3	$7.33e-05$	21.8	23.9
200 - 300	233.7	8	0.1	$2.61e-05$	35.4	16.0

Table 5.4: Measurement of $\frac{d\sigma}{dpt_{jet}}$ for the leading jet in $Z + jet$ events. The range of p_T(jet) corresponds to the intervals used for binning the data (the range 20 to 28 GeV is not considered as measurement). The number of background events is estimated from Monte Carlo. The measurement is presented with three different normalisations (from top to bottom): without normalisation, normalised to the measured inclusive cross section ($\sigma_{\mathrm{incl}} = 120.8\,\mathrm{pb}$) for muons with $|\eta| < 1.7$ and normalised to the integral of Z+jet events with p_T(jet)$>$ 28 GeV. The errors given are relative errors. For $N = 1$ the uncertainty due to the luminosity measurement which is 6.1% is not included.

5.3.7 Measurement of the differential production cross section $\frac{\mathrm{d}\sigma}{\mathrm{d}p_{\mathrm{T}}(\mathrm{jet}_2)}$ as function of the second leading jet p_T

The method used to derive the differenitial production cross section of the trailing and third leading p_T(jet) is analogous to Section 5.3.6. Three iterations are carried out to correct the p_T spectrum of the trailing jet using the *bin-by-bin* correction method. The ratios between the corrected spectra at iteration i and at iteration $i-1$ are shown in Figure 5.15. The result of the fully unfolded leading jet p_T spectrum compared to the *bin-by-bin* correction result including statistical and systematic errors and normalised to the measured inclusive cross section and normalised to the cross section integrated for $p_T(\mathrm{jet}) > 28\,\mathrm{GeV}$ is shown in Figure 5.16. The predictions of Alpgen and Pythia are included. Analogous to the measurement of the leading p_T(jet) the cross section is given w.r.t. to the limited muon acceptance (muon $|\eta| < 1.7$ and no cut on the muon transverse momentum) for 0.5 cone jets (`D0RunIICone` algorithm) as calculated in section 5.1. A summary of the values and errors is also given in Table 5.5. The included bin between 20 and 28 GeV is not meant to be a measurement.

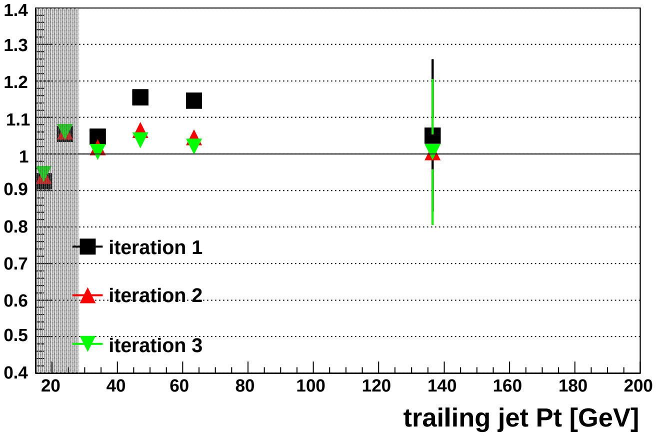

Figure 5.15: Ratio between the *bin-by-bin* corrected spectrum at iteration i and the *bin-by-bin* corrected distribution at iteration $i-1$.

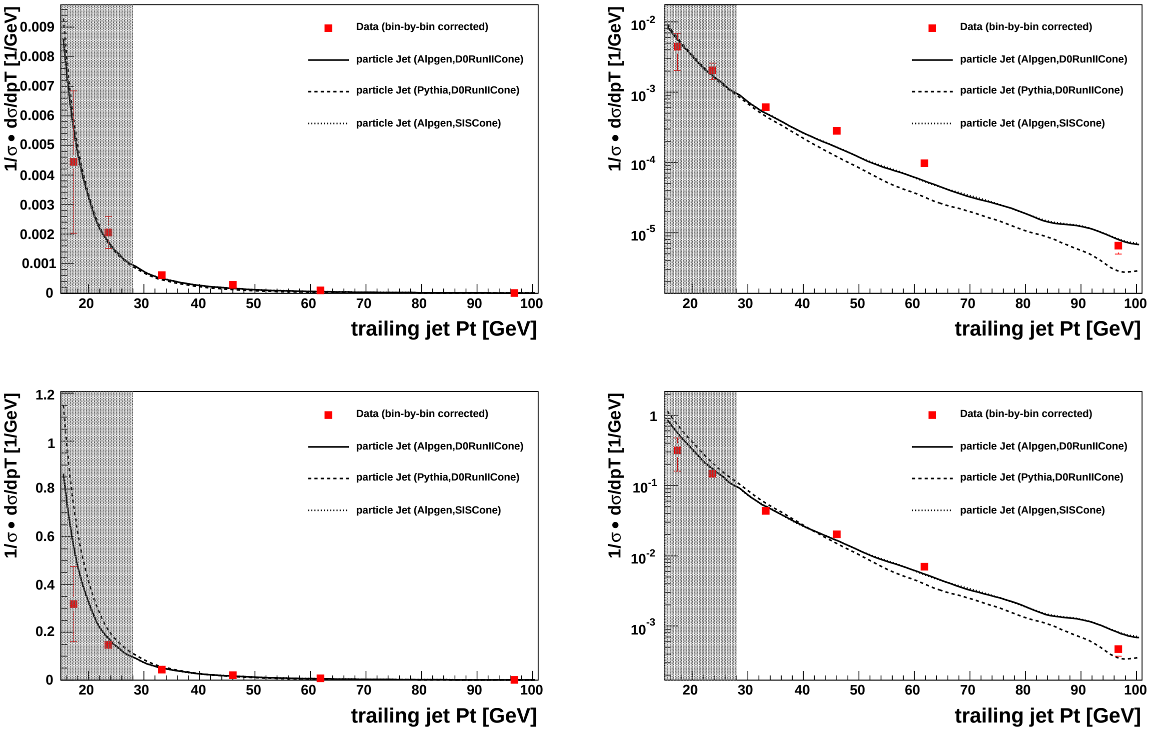

Figure 5.16: *Bin − by − bin* corrected (red quadrats) p_T distribution of the trailing jet compared to the particle jet spectrum of ALPGEN (solid line) and PYTHIA (dotted line). The errors represent the combined statistical and systematic uncertainties. Top: the result is normalised to the measured inclusive cross section ($\sigma_{\text{incl}} = 120.8\,\text{pb}$) for muons with $|\eta| < 1.7$ as determined in Section 5.1; bottom: the result is normalised to the cross section integrated for $p_T(\text{jet}) > 28\,\text{GeV}$.

jet p_T range [GeV]	mean p_T [GeV]	# of events	#of bgd. events	$N \cdot \frac{d\sigma}{dpT(jet)}$ [1/GeV]	err_{stat} [%]	err_{sys} [%]
				$N = 1 \cdot fb^{-1}$		
20 - 28	23.6	632	1.9	$2.47e+02$	4.0	28.2
28 - 40	33.2	253	2.5	$7.32e+01$	6.3	14.9
40 - 54	46.0	108	2.0	$3.39e+01$	9.6	13.3
54 - 73	61.8	50	1.5	$1.17e+01$	14.1	10.7
73 - 200	96.7	26	1.0	$7.88e-01$	19.6	15.8
				$N = \frac{1}{\sigma_{incl,\lvert\eta\rvert<1.7}}$		
20 - 28	23.6	632	1.9	$2.05e-03$	4.0	25.9
28 - 40	33.2	253	2.5	$6.10e-04$	6.3	12.0
40 - 54	46.0	108	2.0	$2.82e-04$	9.6	10.6
54 - 73	61.8	50	1.5	$9.75e-05$	14.1	6.5
73 - 200	96.7	26	1.0	$6.57e-06$	19.6	14.1
				$N = \frac{1}{\sigma_{jet_{pt}>28\,\mathrm{GeV}}}$		
20 - 28	23.6	632	1.9	$1.47e-01$	4.0	18.9
28 - 40	33.2	253	2.5	$4.37e-02$	6.3	2.3
40 - 54	46.0	108	2.0	$2.02e-02$	9.6	5.8
54 - 73	61.8	50	1.5	$6.98e-03$	14.1	6.2
73 - 200	96.7	26	1.0	$4.70e-04$	19.6	6.5

Table 5.5: Measurement of $\frac{d\sigma}{dpt_{jet}}$ for the second leading jet in $Z + jet$ events. The range of p_T(jet) corresponds to the intervals used for binning the data (the range 20 to 28 GeV is not considered as measurement). The number of background events is estimated from Monte Carlo. The measurement is presented with three different normalisations (from top to bottom): without normalisation, normalised to the measured inclusive cross section ($\sigma_{\mathrm{incl}} = 120.8\,\mathrm{pb}$) for muons with $|\eta| < 1.7$ and normalised to the integral of Z+jet events with $p_T(\mathrm{jet}) > 28\,\mathrm{GeV}$. The errors given are relative errors. For $N = 1$ the uncertainty due to the luminosity measurement which is 6.1% is not included.

5.3.8 Measurement of the differential production cross section $\frac{\mathrm{d}\sigma}{\mathrm{d}p_\mathrm{T}(\mathrm{jet}_3)}$ as function of the third leading jet p_T

The same method as for the leading and second leading p_T(jet) was repeated for the third leading p_T(jet) leading to the following results. Three iterations are carried out to correct the p_T spectrum of the third leading jet using the *bin-by-bin* correction method. The ratios between the corrected spectra at iteration i and at iteration $i-1$ which show the convergence of the method are shown in Figure 5.17. The result of the corrected p_T distribution including statistical and systematic errors is shown in Figure 5.18. The result is normalised to the measured inclusive cross section and normalised to the cross section integrated for $p_T(\mathrm{jet}) > 28\,\mathrm{GeV}$. Comparisons to the predicitons of ALPGEN and PYTHIA are included. The cross section is given w.r.t. to the limited muon acceptance (muon $|\eta| < 1.7$ and no cut on the muon transverse momentum) for 0.5 cone jets (`D0`RunIICone algorithm) as calculated in section 5.1. Table 5.6 gives a summary of the values and derived errors. Analogous to the results for the leading and second leading p_T(jet) the included bin between 20 and 28 GeV is not meant to be a measurement.

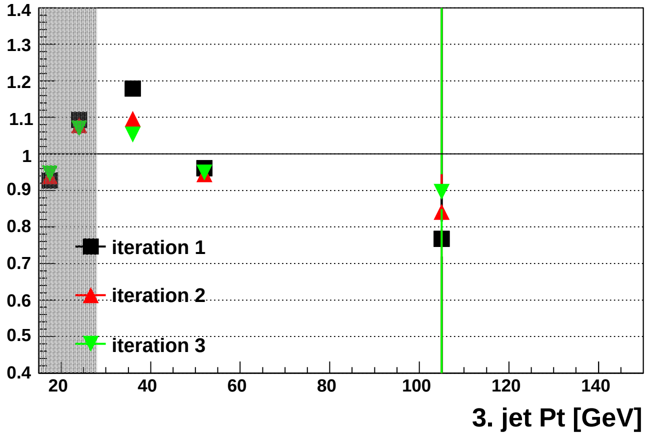

Figure 5.17: Ratio between the *bin-by-bin* corrected spectrum at iteration i and the *bin-by-bin* corrected distribution at iteration $i-1$

.

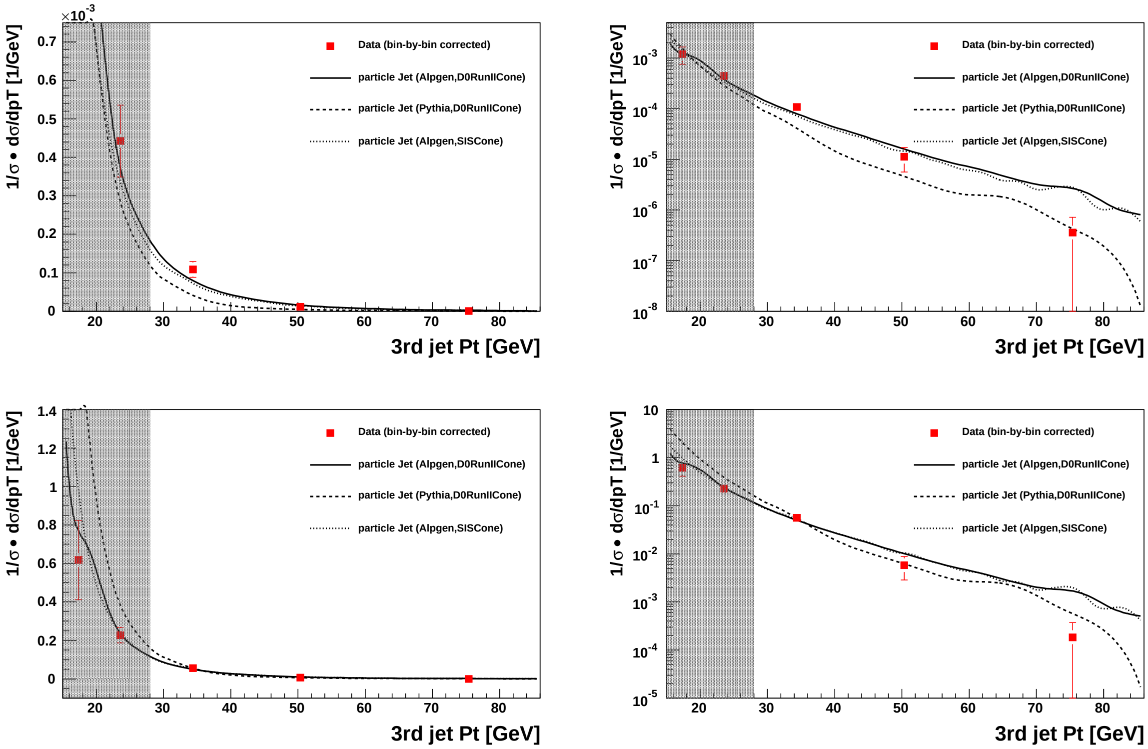

Figure 5.18: *Bin − by − bin* corrected (red quadrats) p_T distribution of the third leading jet compared to the particle jet spectrum of Alpgen (solid line) and Pythia (dotted line). The errors represent the combined statistical and systematic uncertainties. Top: the result is normalised to the measured inclusive cross section ($\sigma_{\text{incl}} = 120.8\,\text{pb}$) for muons with $|\eta| < 1.7$ as determined in Section 5.1; bottom: the result is normalised to the cross section integrated for $p_T(\text{jet}) > 28\,\text{GeV}$.

jet p_T range [GeV]	mean p_T [GeV]	# of events	#of bgd. events	$N \cdot \frac{d\sigma}{dpT(jet)}$ [1/GeV]	err_{stat} [%]	err_{sys} [%]
				$N = 1 \cdot fb^{-1}$		
20 - 28	23.6	100	0.8	$5.31e+01$	10.0	18.7
28 - 44	34.4	38	0.7	$1.30e+01$	16.2	10.4
44 - 60	50.3	5	0.2	$1.36e+00$	44.7	23.0
60 - 150	75.4	1	0.1	$4.30e-02$	100.0	13.9
				$N = \frac{1}{\sigma_{incl,\lvert\eta\rvert<1.7}}$		
20 - 28	23.6	100	0.8	$4.42e-04$	10.0	18.6
28 - 44	34.4	38	0.7	$1.08e-04$	16.2	9.7
44 - 60	50.3	5	0.2	$1.13e-05$	44.7	23.4
60 - 150	75.4	1	0.1	$3.58e-07$	100.0	13.1
				$N = \frac{1}{\sigma_{jet_{pt}>28\,\mathrm{GeV}}}$		
20 - 28	23.6	100	0.8	$2.27e-01$	10.0	14.7
28 - 44	34.4	38	0.7	$5.57e-02$	16.2	3.2
44 - 60	50.3	5	0.2	$5.80e-03$	44.7	24.1
60 - 150	75.4	1	0.1	$1.84e-04$	100.0	13.2

Table 5.6: Measurement of $\frac{d\sigma}{dpt_{jet}}$ for the third leading jet in $Z + jet$ events. The range of p_T(jet) corresponds to the intervals used for binning the data (the range 20 to 28 GeV is not considered as measurement). The number of background events is estimated from Monte Carlo. The measurement is presented with three different normalisations (from top to bottom): without normalisation, normalised to the measured inclusive cross section ($\sigma_{\text{incl}} = 120.8\,\text{pb}$) for muons with $|\eta| < 1.7$ and normalised to the integral of Z+jet events with $p_T(\text{jet}) > 28\,\text{GeV}$. The errors given are relative errors. For $N = 1$ the uncertainty due to the luminosity measurement which is 6.1% is not included.

5.3.9 Validation of the correction procedure using Pythia

As a cross-check the *bin-by-bin* correction procedure is repeated with Pythia instead of using Alpgen as input for the migration matrix. The results for the leading, trailing and third leading p_T jet are shown in Figure 5.19 which gives consistent results.

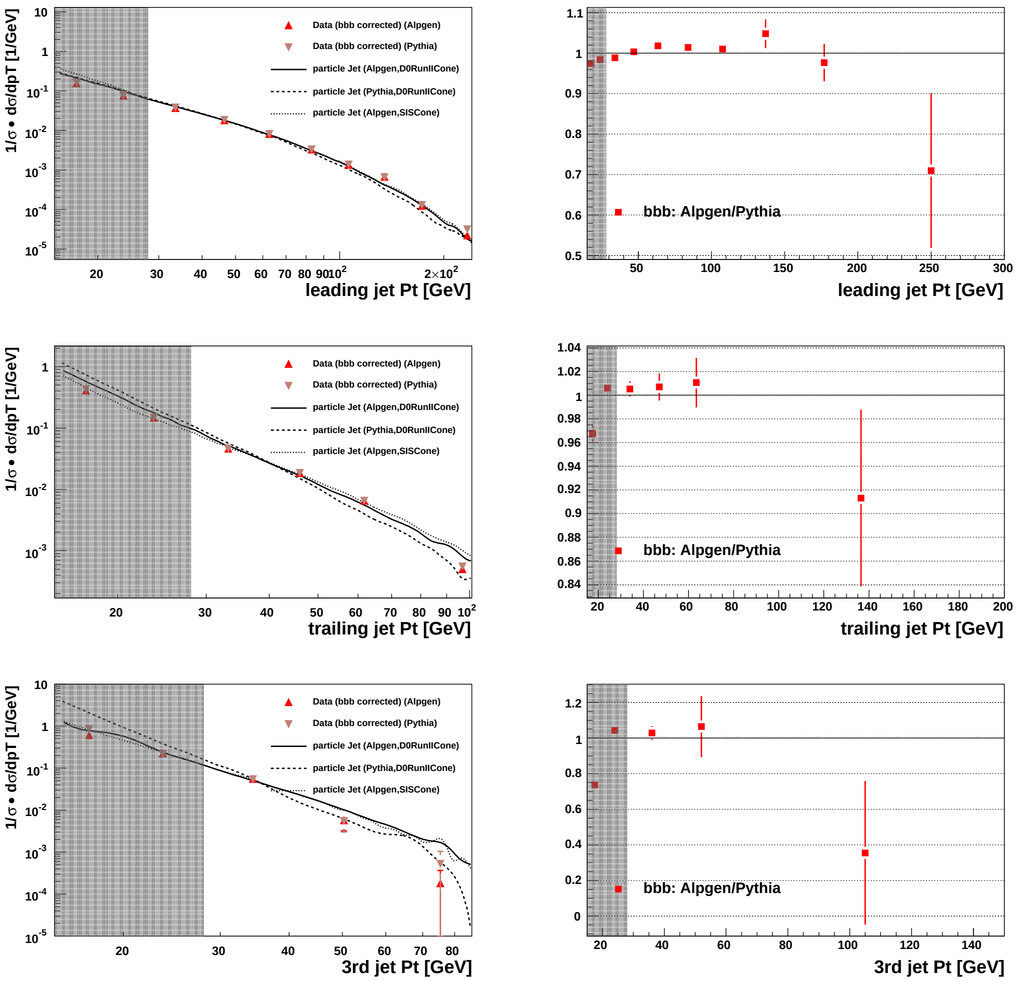

Figure 5.19: $Bin - by - bin$ corrected p_T spectra using Pythia (light red triangles) and the *bin-by-bin* corrected spectra using Alpgen (red triangles) of the i^{th} leading jet. Right plots: Ratios between *bin-by-bin* corrected spectra of the p_T of the i^{th} leading jet using Alpgen and using Pythia to define the migration matrix. The results are normalised to the cross section integrated for $p_T(\text{jet}) > 28\,\text{GeV}$. Errors shown are statistical only.

5.3.10 Unfolding the jet multiplicity for jets with p_T(jet) > 28 GeV

The distribution of the jet multiplicity is a distribution of a discrete variable. Since the method used in the program *RUN* assumes continuous variables, only the *bin-by-bin* correction can be applied to measure this distribution.

Figure 5.21 shows the result of the closure test. The result of the fully corrected and unsmeared jet multiplicity including systematic and statistical uncertainties compared to the particle jet distributions predicted by ALGPEN and PYTHIA is shown in Figure 5.23 and the corresponding fractional uncertainties in Figure 5.24. Figure 5.22 shows the distribution of the jet multiplicity as result of the *bin-by-bin* correction using ALPGEN compared to the result of the *bin-by-bin* correction using PYTHIA as an additional cross-check.

jet mult. (excl.)	number of events	number of bgd. events	$\frac{1}{\sigma_{incl}} \frac{\sigma}{N(jets)}$	err_{stat}	err_{sys}	err_{stat} [%]	err_{sys} [%]
0	48176	79.9	$9.05e-01$	$4.12e-03$	$4.11e-03$	0.5	0.5
1	3767	12.3	$8.05e-02$	$1.31e-03$	$4.02e-03$	1.6	5.0
2	393	6.1	$1.29e-02$	$6.49e-04$	$1.12e-03$	5.0	8.7
3	43	0.9	$2.07e-03$	$3.16e-04$	$3.31e-04$	15.2	16.0
4	1	0.1	$2.25e-05$	$2.25e-05$	$2.40e-05$	100.0	106.4

Table 5.7: Exclusive jet multiplicity distribution for jets with p_T(jet)$>$ 28 GeV. The result is normalised to the measured inclusive cross section. The number of background events is estimated from Monte Carlo. Relative and absolute errors are given.

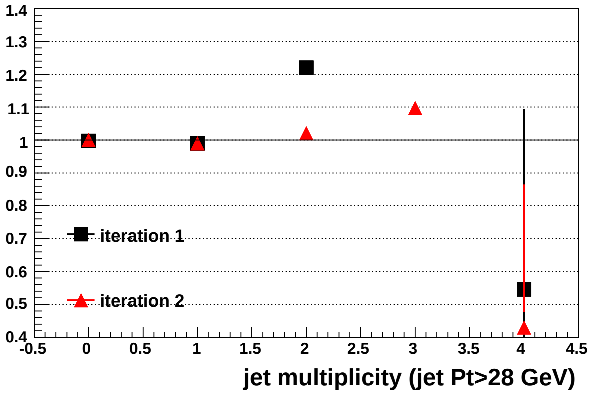

Figure 5.20: Ratio between the *bin-by-bin* corrected spectrum at iteration i and the *bin-by-bin* corrected distribution at iteration $i-1$.

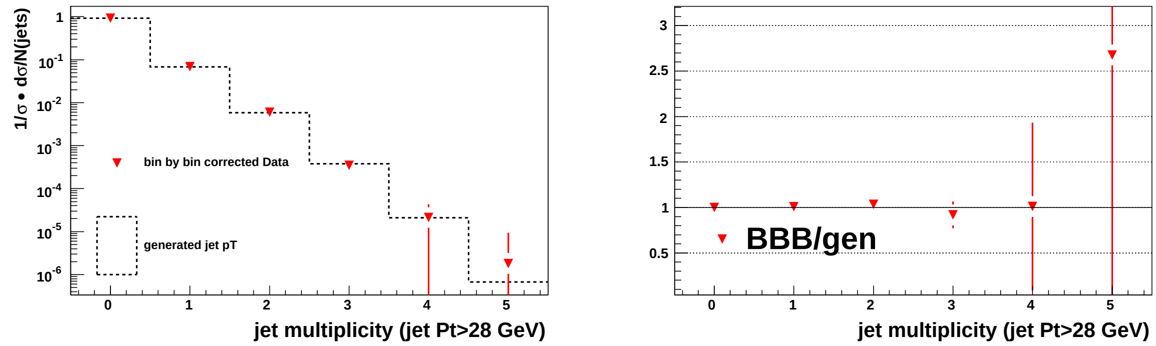

Figure 5.21: Closure test for the jet multiplicity for jets with $p_T(\text{jet}) > 28\,\text{GeV}$. The results are normalised to the measured inclusive cross section. Left plot: *bin-by-bin* corrected (red triangles) jet multiplicity using Pythia as data and Algpen to define the migration matrix compared to the particle jet multiplicity (histogram) generated with Pythia. Right plot: Ratio between the *bin-by-bin* corrected jet multiplicity and the particle jet multiplicity (red triangles) generated with Pythia. Errors shown are statistical only.

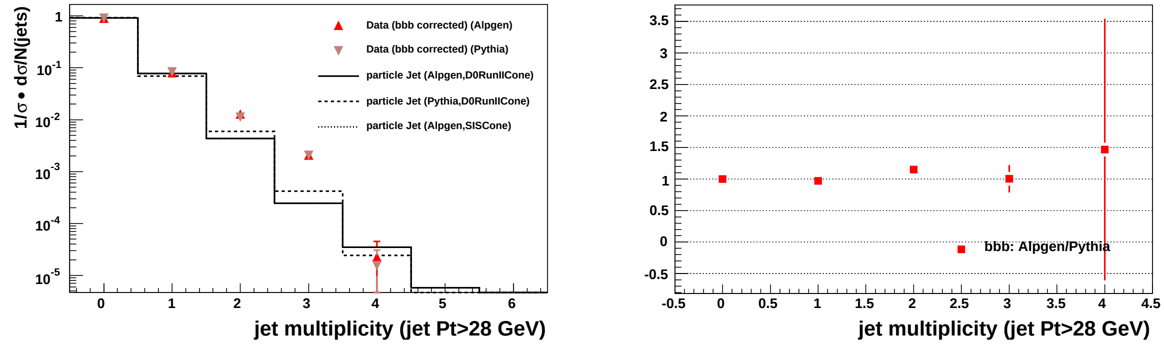

Figure 5.22: Left plot: *bin-by-bin* corrected jet multiplicity for jets with $p_T(\text{jet}) > 28\,\text{GeV}$ using Pythia (light red triangles) and using Alpgen (red triangles) compared to the particle jet multiplicity generated with Alpgen (solid line) and Pythia (dashed line). The results are normalised to the measured inclusive cross section. Right plot: Ratio between the result of *bin-by-bin* corrected jet multiplicity for jets with $p_T(\text{jet}) > 28\,\text{GeV}$ using Alpgen and using Pythia. Errors shown are statistical only.

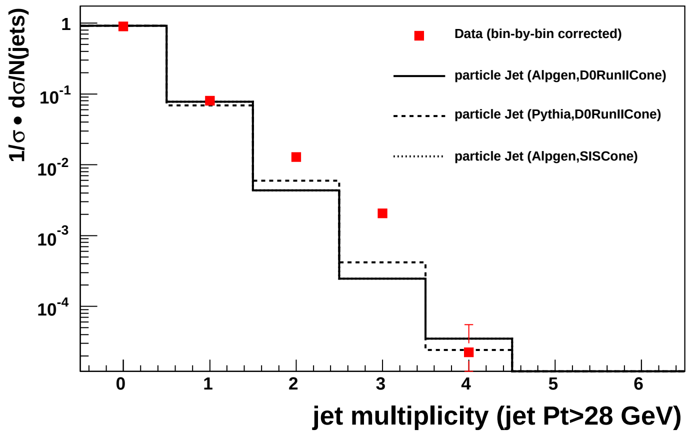

Figure 5.23: *Bin − by − bin* corrected jet multiplicity for jets with $p_T(\text{jet}) > 28\,\text{GeV}$ compared to the particle jet multiplicity generated using ALPGEN (solid line) and PYTHIA (dotted line). The result is normalised to the measured inclusive cross section. The errors contain systematic and statistical errors.

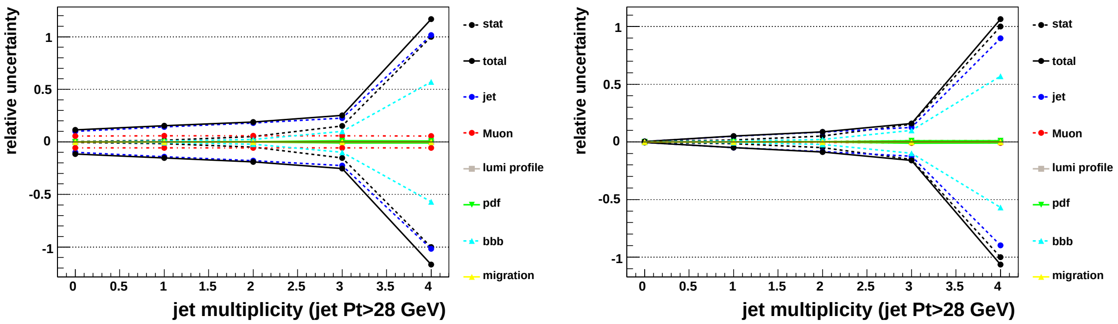

Figure 5.24: Combination of all relative uncertainties in the *bin-by-bin* corrected data for the jet multiplicity for jets with $p_T(\text{jet}) > 28\,\text{GeV}$. Left plot: Total uncertainties. Right plot: Uncertainties after normalising the data distribution to the measured inclusive cross section. Shown are the statistical error (stat), the total uncertainty (total) and the individual sources to the total uncertainty: the error resulting from the jet uncertainties (jet), the error resulting from the muon uncertainties (Muon), the uncertainties resulting from the luminosity profile reweighting (lumi profile) and the PDF reweighting (pdf), respectively and the uncertainties due to the *bin-by-bin* correction procedure (bbb and migration).

5.3.11 Unfolding the jet multiplicity for jets with p_T(jet) > 20 GeV

Below the exclusive jet multiplicity for jet with $p_T(jet) > 20$ GeV is reported. Similar figures as for the multiplicity for $p_T(jet) > 20$ GeV are shown. Figure 5.26 shows the result of the closure test. The result of the *bin-by-bin* corrected jet multiplicity including sytematic and statistical uncertainties compared to the particle jet distribution predicted by ALGPEN and PYTHIA is shown in Figure 5.28, the corresponding fractional uncertainties in Figure 5.29. Figure 5.27 shows the distribution of the jet multiplicity as result of the *bin-by-bin* correction using ALPGEN compared to the result of the *bin-by-bin* correction using PYTHIA.

jet mult. (excl.)	number of events	number of bgd. events	$\frac{1}{\sigma_{incl}} \frac{\sigma}{N(jets)}$	err_{stat}	err_{sys}	err_{stat} [%]	err_{sys} [%]
0	45001	75.3	$8.47e-01$	$3.99e-03$	$7.66e-03$	0.5	1.1
1	6310	14.9	$1.18e-01$	$1.49e-03$	$5.51e-03$	1.3	6.7
2	925	7.2	$2.79e-02$	$9.16e-04$	$3.26e-03$	3.3	12.1
3	129	1.4	$5.99e-03$	$5.27e-04$	$9.41e-04$	8.8	15.8
4	14	0.4	$4.97e-04$	$1.33e-04$	$1.49e-04$	26.7	29.9
5	1	0.0	$1.95e-05$	$1.95e-05$	$2.06e-05$	100.0	105.8

Table 5.8: Measurement of the jet multiplicity distribution for jets with p_T(jet) > 20 GeV. The result is normalised to the measured inclusive cross section. The number of background events is estimated from Monte Carlo. Absolute and relative errors are given.

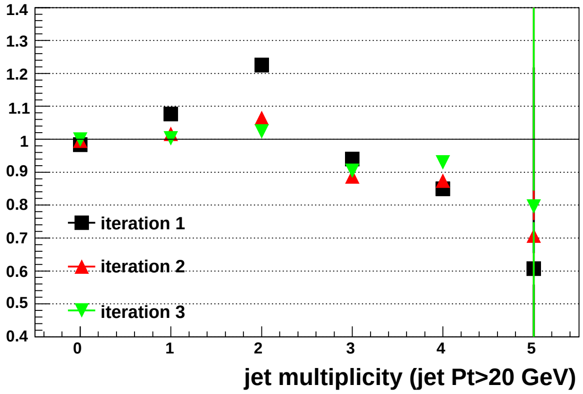

Figure 5.25: Ratio between the *bin-by-bin* corrected spectrum at iteration i and the *bin-by-bin* corrected distribution at iteration $i-1$.

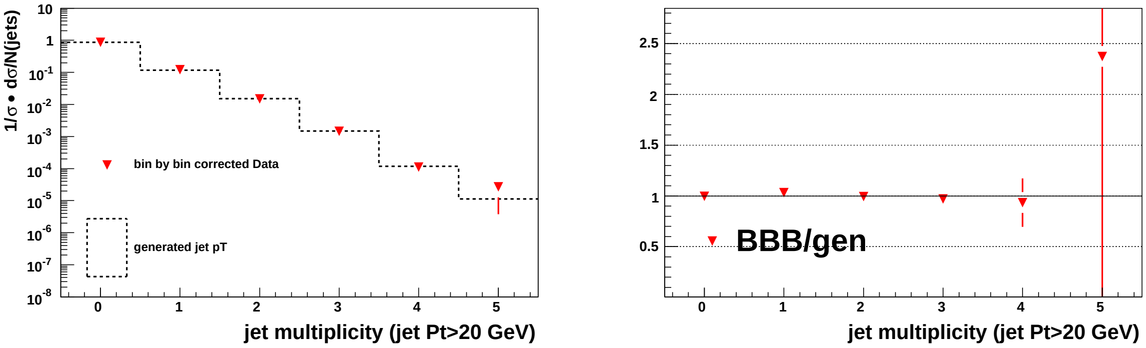

Figure 5.26: Closure test for the jet multiplicity for jets with $p_T(\text{jet}) > 20\,\text{GeV}$. The results are normalised to the measured inclusive cross section. Left plot: *bin-by-bin* corrected (red triangles) jet multiplicity using PYTHIA as data and Algpen to define the migration matrix compared to the particle jet multiplicity (histogram) generated with PYTHIA. Right plot: Ratio between the *bin-by-bin* corrected jet multiplicity and the particle jet multiplicity (red triangles) generated using PYTHIA. Errors shown are statistical only.

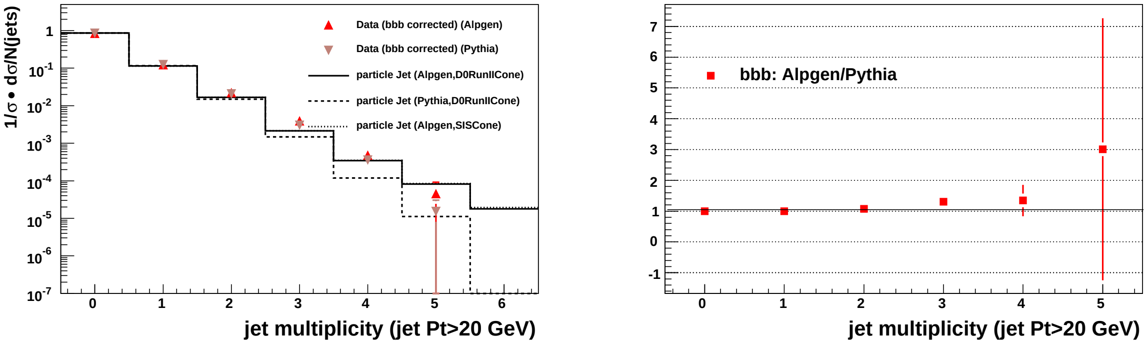

Figure 5.27: Left plot: *bin-by-bin* corrected jet multiplicity for jets with $p_T(\text{jet}) > 20\,\text{GeV}$ using PYTHIA (light red triangles) and using ALPGEN (red triangles) compared to the particle jet multiplicity generated with ALPGEN (solid line) and PYTHIA (dashed line). The results are normalised to the measured inclusive cross section. Right plot: Ratio between the result of *bin-by-bin* corrected jet multiplicity for jets with $p_T(\text{jet}) > 20\,\text{GeV}$ using ALPGEN and using PYTHIA. Errors shown are statistical only.

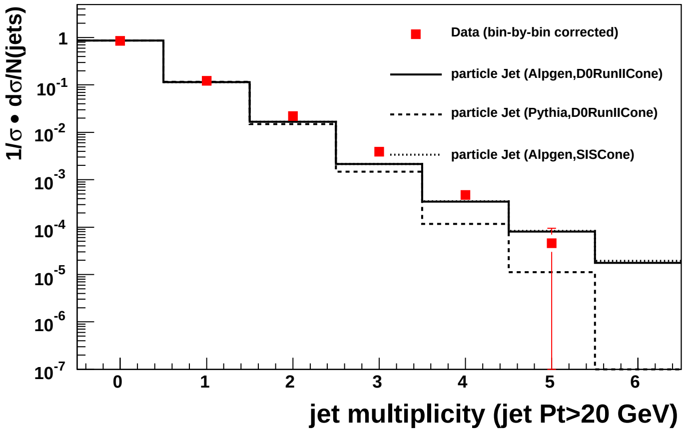

Figure 5.28: *Bin − by − bin* corrected jet multiplicity for jets with $p_T(\text{jet}) > 20\,\text{GeV}$ compared to the particle jet multiplicity generated using ALPGEN (solid line) and PYTHIA (dotted line). The result is normalised to the measured inclusive cross section. The errors contain systematic and statistical errors.

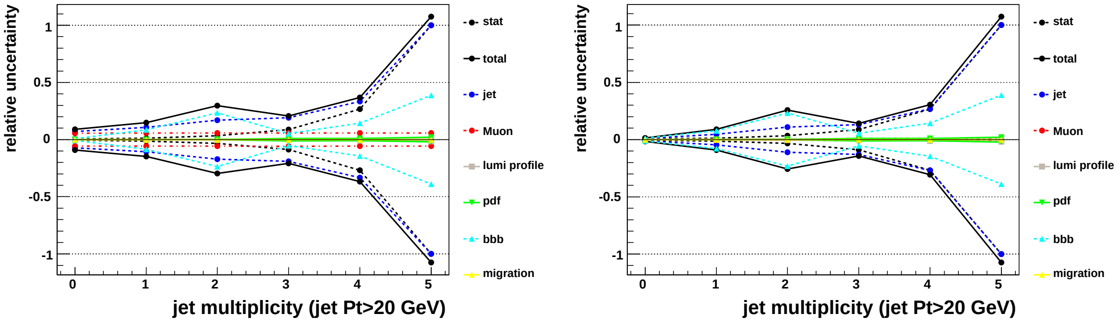

Figure 5.29: Combination of all relative uncertainties for jets with $p_T(\text{jet}) > 20\,\text{GeV}$ in the *bin-by-bin* corrected data for the jet multiplicity. Left plot: Total uncertainties. Right plot: Uncertainties after normalising the data distribution to the measured inclusive cross section. Shown are the statistical error (stat), the total uncertainty (total) and the individual sources to the total uncertainty: the error resulting from the jet uncertainties (jet), the error resulting from the muon uncertainties (Muon), the uncertainties resulting from the luminosity profile reweighting (lumi profile) and the PDF reweighting (pdf), respectively and the uncertainties due to the *bin-by-bin* correction procedure (bbb and migration).

5.3.12 Acceptance correction to the full phase space

To correct from hadron level with muon $|\eta_\mu| < 1.7$ to the 4π inclusive phase space the ratio

$$\frac{\sigma_{\rm i}(|\eta_\mu| < 1.7)}{\sigma_{\rm i}}$$

is taken from Monte Carlo. The systematic uncertainty to this correction factors is evaluated by determing the ratio using the Alpgen and Pythia event generators, respectively:

$$\frac{\sigma_{\rm i}(|\eta_\mu| < 1.7, \text{Pythia})}{\sigma_{\rm i}(\text{Pythia})} / \frac{\sigma_{\rm i}(|\eta_\mu| < 1.7, \text{Alpgen})}{\sigma_{\rm i}(\text{Alpgen})}$$

Figures 5.30 and 5.31 show the ratio for the leading, second and third leading p_T(jet) and the jet multiplicity, respectively. Tables 5.9 and 5.10 summarize the cross sections corrected to hadron level with muon $|\eta_\mu| < 1.7$ and to the full phase space, respectively.

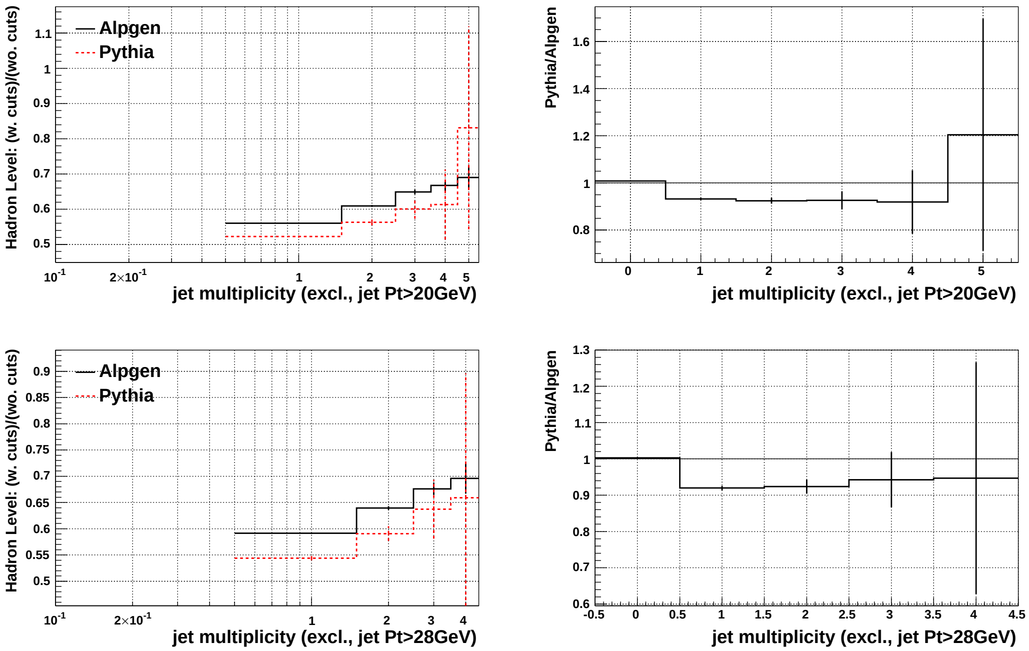

Figure 5.30: The ratio $\frac{N(jets),|\eta_\mu|<1.7)}{N(jets))}$ as predicted by Alpgen and Pythia. Top: Exclusive jet mulitplicity for jets with $p_T(\text{jet}) > 20\,\text{GeV}$. Bottom: Exclusive jet mulitplicity for jets with $p_T(\text{jet}) > 28\,\text{GeV}$.

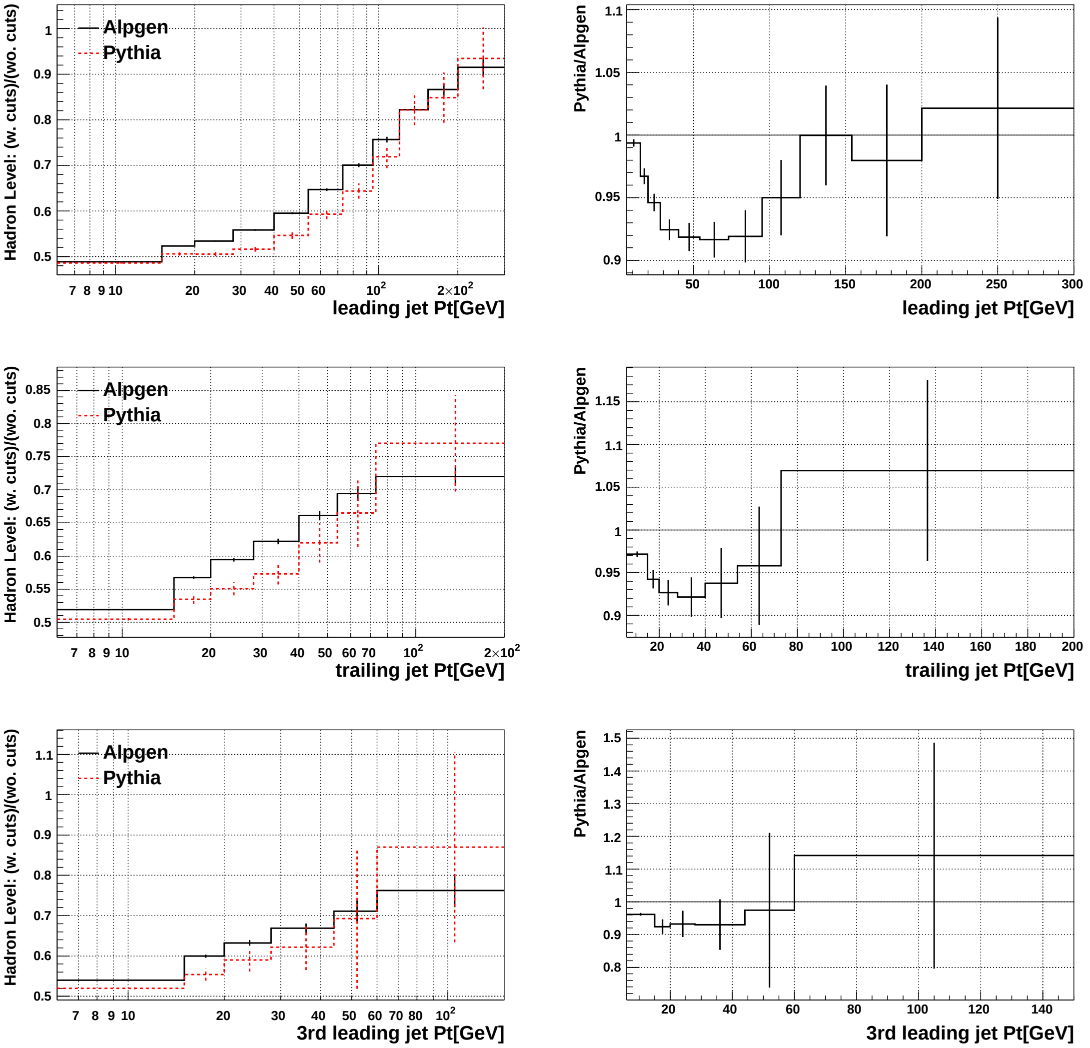

Figure 5.31: The ratio $\frac{p_{\mathrm{T}}(i^{\mathrm{th}}(jet),|\eta_\mu|<1.7)}{p_{\mathrm{T}}(i^{\mathrm{th}}(jet))}$ as predicted by ALPGEN and PYTHIA. Top: leading p_T(jet) ; middle: trailing p_T(jet) ; bottom: third leading p_T(jet) .

mean p_T [GeV]	$\frac{1}{\sigma_{incl,\|\eta_\mu\|<1.7}}\frac{d\sigma}{dp_T(jet)}$ [1/GeV]	err_{stat} [%]	err_{sys} [%]	acc_{corr}	$\frac{1}{\sigma_{incl}\cdot acc_{corr}}\frac{d\sigma}{dp_T(jet)}$ [1/GeV]	err_{acc} [%]
Leading jet						
23.7	$7.25e-03$	1.8	6.7	0.53	$6.61e-03$	5.0
33.5	$3.78e-03$	2.2	7.3	0.55	$3.32e-03$	7.0
46.4	$1.85e-03$	3.1	5.3	0.59	$1.51e-03$	7.7
62.6	$8.03e-04$	4.0	6.7	0.65	$5.97e-04$	8.1
82.9	$3.23e-04$	6.0	4.9	0.69	$2.26e-04$	7.3
106.2	$1.28e-04$	8.8	4.2	0.76	$8.12e-05$	4.9
134.7	$8.56e-05$	10.9	10.6	0.82	$5.04e-05$	0.2
173.0	$7.35e-06$	21.8	25.0	0.86	$4.13e-06$	1.8
233.7	$2.62e-06$	35.4	18.4	0.90	$1.41e-06$	3.4
Second leading jet						
23.6	$2.05e-03$	4.0	25.9	0.60	$1.65e-03$	7.7
33.2	$6.10e-04$	6.3	12.0	0.63	$4.68e-04$	8.8
46.0	$2.82e-04$	9.6	10.6	0.66	$2.07e-04$	6.2
61.8	$9.75e-05$	14.1	6.5	0.69	$6.83e-05$	3.8
96.7	$6.57e-06$	19.6	14.1	0.72	$4.41e-06$	6.5
Third leading jet						
23.6	$4.42e-04$	10.0	18.6	0.63	$3.39e-04$	6.7
34.4	$1.08e-04$	16.2	9.7	0.67	$7.81e-05$	6.7
50.3	$1.13e-05$	44.7	23.4	0.71	$7.69e-06$	1.9
75.4	$3.58e-07$	100.0	13.1	0.76	$2.28e-07$	15.2

Table 5.9: Summary of the results of the measurement of $\frac{d\sigma}{dp_T(jet)}$ for the i^{th} jet in $Z+$ jet events. The results are normalised to the inclusive cross section for muons with $|\eta_\mu| < 1.7$ and the 4π inclusive phase space, respectively. acc_{corr} denotes the factor to correct the cross sections from hadron level with muon $|\eta_\mu| < 1.7$ to the 4π inclusive phase space. All errors given are relative errors.

jet mult. (excl.)	$\frac{1}{\sigma_{incl,\lvert\eta_\mu\rvert<1.7}}\frac{\sigma}{N(jets)}$	err_{stat} [%]	err_{sys} [%]	acc_{corr}	$\frac{1}{\sigma_{incl}\cdot acc_{corr}}\frac{\sigma}{N(jets)}$	err_{acc} [%]
p_T(jet) > 20 GeV						
0	$8.50e-01$	0.5	1.5	0.47	$8.70e-01$	0.8
1	$1.24e-01$	1.3	9.0	0.56	$1.06e-01$	6.8
2	$2.23e-02$	3.3	25.7	0.61	$1.76e-02$	7.6
3	$3.94e-03$	8.8	14.2	0.65	$2.92e-03$	7.4
4	$4.81e-04$	26.7	30.6	0.67	$3.45e-04$	8.1
5	$4.58e-05$	100.0	107.3	0.69	$3.19e-05$	20.4
p_T(jet) > 28 GeV						
0	$8.97e-01$	0.5	0.5	0.48	$9.03e-01$	0.3
1	$8.87e-02$	1.6	5.2	0.59	$7.27e-02$	8.0
2	$1.29e-02$	5.0	8.6	0.64	$9.76e-03$	7.6
3	$1.40e-03$	15.2	11.5	0.68	$9.97e-04$	5.7
4	$1.81e-05$	100.0	105.2	0.70	$1.25e-05$	5.3

Table 5.10: Summary of the results of the measurement of the jet multiplicity for jets with p_T(jet) > 20 GeV and p_T(jet) > 28 GeV. The results are normalised to the measured inclusive cross sections for muons with $|\eta_\mu| < 1.7$ and the 4π inclusive cross section, respectively. acc_{corr} denotes the factor to correct the cross sections from hadron level with muon $|\eta_\mu| < 1.7$ to the 4π inclusive phase space. All errors given are relative errors.

5.3.13 Correction to the SISCone jet algorithm at particle level

The measurement is corrected to an alternative jet cone algorithm the `SISCone` algorithm, which is included in the public libary. This is an infrared safe cone jet algorithm. Assuming that the shapes of the distributions between a bin are identical between data and simulation the measurement can be corrected to different jet algorithms based on the particle level correction. The correction factors are given by the cross section ratios:

$$\frac{\sigma_{\mathrm{i}}(\texttt{SISCone})}{\sigma_{\mathrm{i}}(\texttt{D0RunIICone})}$$

The systematic uncertainty to this correction factors is given by the double ratio:

$$\frac{\sigma_{\mathrm{i}}(\texttt{SISCone}, \textsc{Pythia})}{\sigma_{\mathrm{i}}(\texttt{D0RunIICone}, \textsc{Pythia})} \Big/ \frac{\sigma_{\mathrm{i}}(\texttt{SISCone}, \textsc{Alpgen})}{\sigma_{\mathrm{i}}(\texttt{D0RunIICone}, \textsc{Alpgen})}$$

The corrections turn out to be tiny and everywhere consistent to 1. Tables 5.11 and 5.12 summarize the measured cross sections, together with uncertainties due to statistics and systematics for the i^{th} $p_T(\mathrm{jet})$ and the exclusive jet multiplicities. The results are normalised to the measured cross section for $Z \rightarrow \mu^+\mu^-$ events with mass $65 - 115\,\mathrm{GeV}$ and $|\mu(\eta)| < 1.7$ of $120.8\,\mathrm{pb}$ as calculated in Section 5.1. The cross sections obtained using the `D0RunII` jet finding algorithm are compared to the cross sections obtained using the `SISCone` jet finding algorithm.

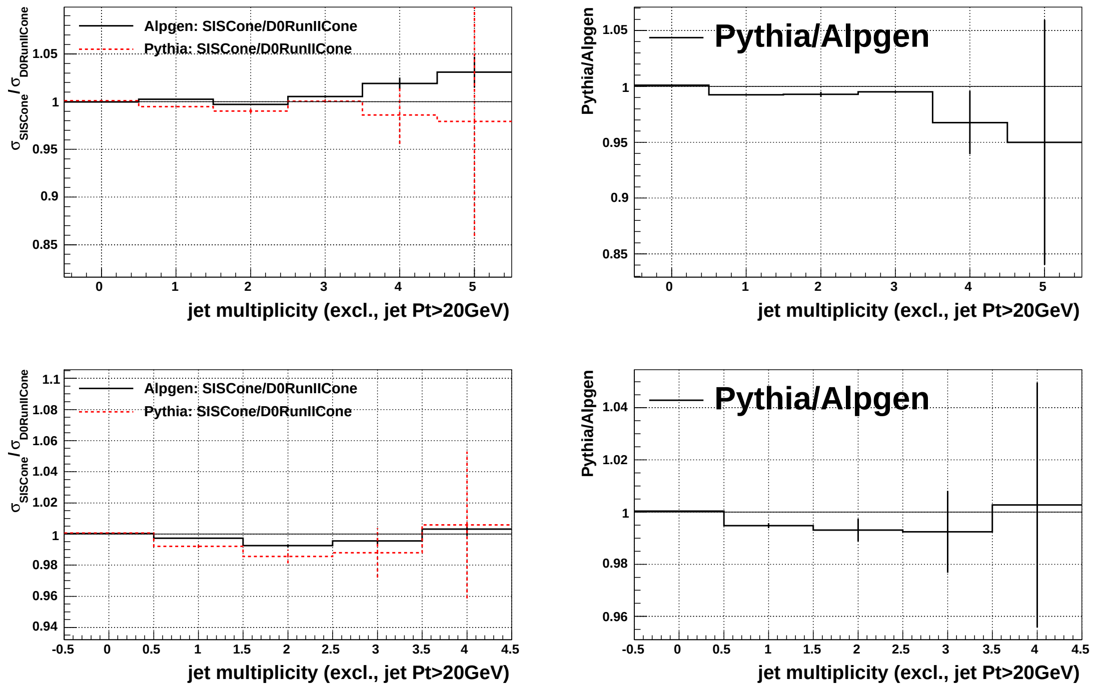

Figure 5.32: Left plots: The cross section ratios $\frac{\sigma_i(\texttt{SISCone})}{\sigma_i(\texttt{D0RunIICone})}$ as predicted by ALPGEN and PYTHIA. Right plots: The double ratios. Top: Exclusive jet multiplicity for jets with $p_T(\text{jet}) > 20\,\text{GeV}$. $p_T(\text{jet})$. Bottom: Exclusive jet multiplicity for jets with $p_T(\text{jet}) > 28\,\text{GeV}$.

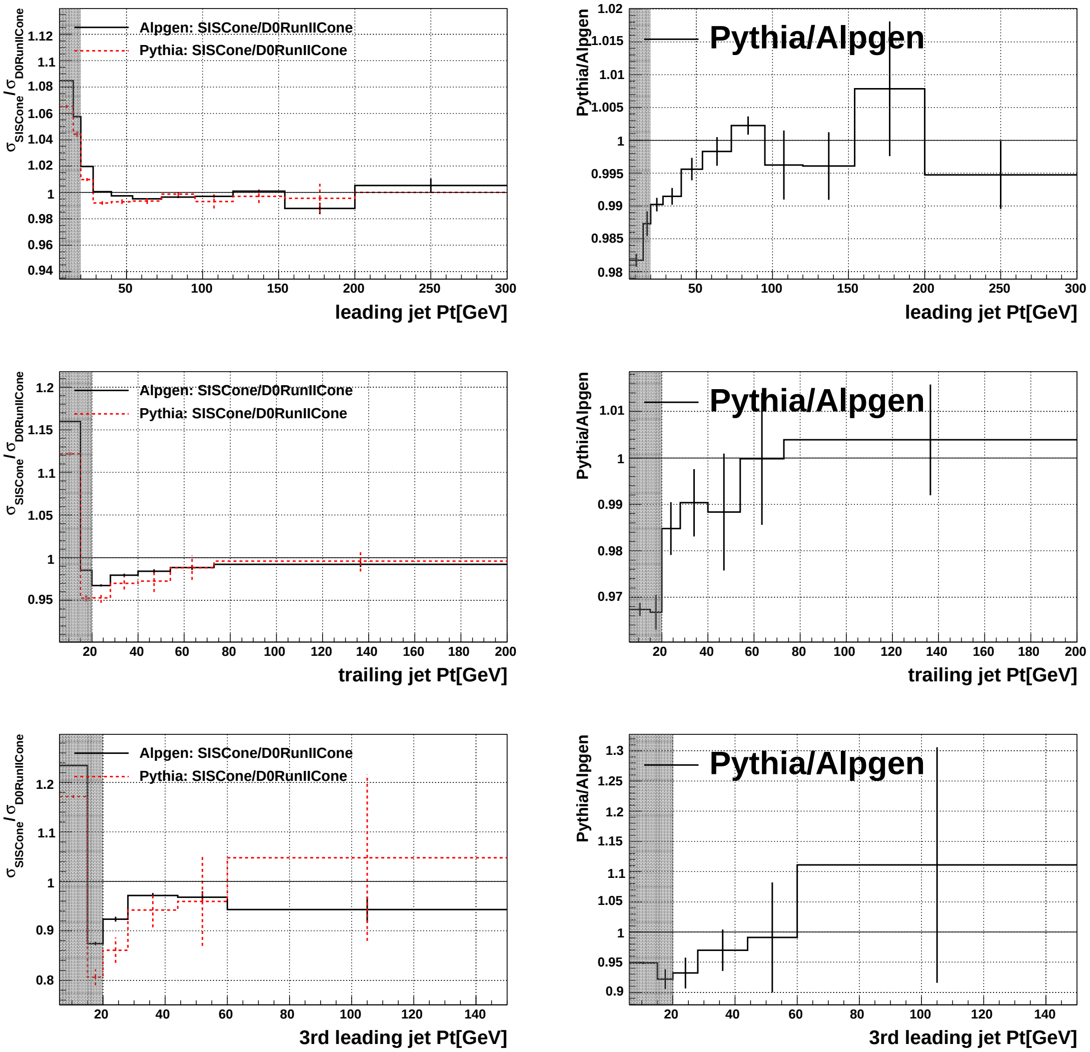

Figure 5.33: Left plots: The cross section ratios $\frac{\sigma_i(\texttt{SISCone})}{\sigma_i(\texttt{D0RunIICone})}$ as predicted by Alpgen and Pythia. Right plots: The double ratios. Top: leading p_T(jet) ; middle: trailing p_T(jet) ; bottom: third leading p_T(jet) .

mean p_T [GeV]	`D0RunII` $\frac{1}{\sigma_{incl,\lvert\eta\rvert<1.7}} \frac{d\sigma}{dpT(jet)}$ [1/GeV]	err_{stat} [%]	err_{sys} [%]	acc_{corr}	`SISCone` $\frac{1}{\sigma_{incl,\lvert\eta\rvert<1.7} \cdot acc_{corr}} \frac{d\sigma}{dpT(jet)}$ [1/GeV]	err_{acc} [%]
Leading jet						
23.7	$7.25e-03$	1.8	6.7	1.02	$7.11e-03$	1.0
33.5	$3.78e-03$	2.2	7.3	1.00	$3.78e-03$	0.9
46.4	$1.85e-03$	3.1	5.3	1.00	$1.85e-03$	0.4
62.6	$8.03e-04$	4.0	6.7	1.00	$8.03e-04$	0.2
82.9	$3.23e-04$	6.0	4.9	1.00	$3.23e-04$	0.2
106.2	$1.28e-04$	8.8	4.2	1.00	$1.28e-04$	0.4
134.7	$8.56e-05$	10.9	10.6	1.00	$8.56e-05$	0.4
173.0	$7.35e-06$	21.8	25.0	0.99	$7.42e-06$	0.8
233.7	$2.62e-06$	35.4	18.4	1.01	$2.60e-06$	0.5
Second leading jet						
23.6	$2.05e-03$	4.0	25.9	0.97	$2.12e-03$	1.5
33.2	$6.10e-04$	6.3	12.0	0.98	$6.22e-04$	1.0
46.0	$2.82e-04$	9.6	10.6	0.98	$2.88e-04$	1.2
61.8	$9.75e-05$	14.1	6.5	0.99	$9.85e-05$	0.0
96.7	$6.57e-06$	19.6	14.1	0.99	$6.63e-06$	0.4
Third leading jet						
23.6	$4.42e-04$	10.0	18.6	0.92	$4.81e-04$	6.8
34.4	$1.08e-04$	16.2	9.7	0.97	$1.12e-04$	3.0
50.3	$1.13e-05$	44.7	23.4	0.97	$1.16e-05$	0.9
75.4	$3.58e-07$	100.0	13.1	0.94	$3.81e-07$	11.1

Table 5.11: Summary of the results of the measurement of $\frac{d\sigma}{dpt_{jet}}$ for the i^{th} jet in $Z+$ jet events using the `D0RunII` jet finding algorithm and the `SISCone` jet finding algorithm. acc_{corr} denotes the correction factor to correct the result obtained using the `D0RunII` jet finding algorithm to the `SISCone` jet finding algorithm. The results are normalised to the inclusive cross section for muons with $|\eta| < 1.7$. All errors given are relative errors.

jet mult. (excl.)	`D0RunII` $\frac{1}{\sigma_{incl,\lvert\eta\rvert<1.7}} \frac{\sigma}{N(jets)}$	err_{stat} [%]	err_{sys} [%]	acc_{corr}	`SISCone` $\frac{1}{\sigma_{incl,\lvert\eta\rvert<1.7} \cdot acc_{corr}} \frac{\sigma}{N(jets)}$	err_{acc} [%]
p_T(jet) $> 20\,\text{GeV}$						
0	$8.50e-01$	0.5	1.5	1.00	$8.46e-01$	0.1
1	$1.24e-01$	1.3	9.0	1.00	$1.23e-01$	0.8
2	$2.23e-02$	3.3	25.7	1.00	$2.22e-02$	0.7
3	$3.94e-03$	8.8	14.2	1.01	$3.89e-03$	0.5
4	$4.81e-04$	26.7	30.6	1.02	$4.70e-04$	3.2
5	$4.58e-05$	100.0	107.3	1.03	$4.43e-05$	5.0
p_T(jet) $> 28\,\text{GeV}$						
0	$8.97e-01$	0.5	0.5	1.00	$8.97e-01$	0.5
1	$8.87e-02$	1.6	5.2	0.99	$8.97e-02$	0.7
2	$1.29e-02$	5.0	8.6	1.00	$1.29e-02$	0.8
3	$1.40e-03$	15.2	11.5	1.00	$1.40e-03$	0.3
4	$1.81e-05$	100.0	105.2	1.00	$1.81e-05$	0.3

Table 5.12: Summary of the results of the measurement of the exclusive jet multiplicity for jets with $p_T(\text{jet}) > 20\,\text{GeV}$ and $p_T(\text{jet}) > 28\,\text{GeV}$ in $Z+$ jet events using the `D0RunII` jet finding algorithm and the `SISCone` jet finding algorithm. acc_{corr} denotes the correction factor to correct the result obtained using the `D0RunII` jet finding algorithm to the `SISCone` jet finding algorithm. The results are normalised to the measured inclusive cross section for muons with $|\eta| < 1.7$. The errors given are relative errors.

6 Results

This chapter summarizes the results of the measured inclusive Z cross section in association with jets. The measurements are compared to the predictions from the ALPGEN and PYTHIA event generators.

The measured cross sections are corrected for acceptance and migration effects back to the hadron level using ALPGEN events. The cross sections are derived using the *bin-by-bin* unfolding method that also accounts for the efficiency of the $Z/\gamma^* \rightarrow \mu^+\mu^-$ selection criteria. The final results refer to hadron-level jets with $p_T(\text{jet}) > 28\,\text{GeV}$ and $|y(\text{jet})| < 2.5$ in a limited and well defined kinematic range for the Z/γ^* decay products. To validate the unfolding method the correction procedure has been repeated with PYTHIA instead of using ALPGEN to define the migration matrix. This cross check gives consistent results. In addition an alternative unfolding method has been applied to correct the leading $p_T(\text{jet})$. Again, consistent results could be achieved.

The cross section is first derived with respect to the limited acceptance for the muons from the Z boson decay, corresponding to $|\eta_\mu| < 1.7$ (and no requirement on muon p_T) and then corrected to the full phase space of the produced di-muon pair. The hadron level jets are defined by the `D0RunIICone` algorithm with a cone size of $R = 0.5$. A correction to match the cross sections w.r.t. the `SISCone` algorithm is presented in addition. Tables 6.1, 6.2 and 6.3 give a summary of the measured cross sections corrected to the full acceptance and normalised to the inclusive cross section. This cancels the uncertainty on the luminosity measurement.

Since the measured cross sections are fully corrected with respect to the mentioned kinematic acceptance they can be directly compared to the theoretical predictions of event generators. Figures 6.1, 6.2 and 6.3 compare the i^{th} $p_T(\text{jet})$ in data at hadron level for jets with $p_T(\text{jet}) > 28\,\text{GeV}$ and $|y(\text{jet})| < 2.5$ with the predictions of ALPGEN and PYTHIA. Statistical and systematical uncertainties are combined in quadrature and displayed as yellow bands. In addition the data points are given with error bars representing the statistical uncertainties only.

In the ALPGEN sample as described in Section 4.3 exclusive $Z/\gamma^* \rightarrow \mu^+\mu^- + n$ partons final states have been produced for $n = 0, 1, 2, 3, 4$. Leading order matrix elements interfaced with PYTHIA for parton shower evolution are used and PYTHIA is also employed for the hadronization process. The multi-parton samples are matched using the MLM matching scheme and are combined using the relative cross sections provided by ALPGEN. The final sample is normalised to the inclusive cross section. PYTHIA uses the $2 \rightarrow 2$ matrix-element with a Q^2 ordered parton shower correction to match the matrix-element prediction for Z+jets.

Figure 6.1 shows the measurement of the leading jet. The theoretical prediction given by ALPGEN predicts $\sim 30\%$ less jets than seen in data but reproduces the shape measured in data while PYTHIA gives a softer p_T spectrum. This is disfavored by the data. The ratio data/ALPGEN is approximately independent of p_T(jet) .

The discrepancy at $\sim 135\,\mathrm{GeV}$ can be attributed to a fluctuation in the data that is already present at reconstruction level (see Figure 4.8). Due to the steeply falling distribution of the leading jet p_T spectrum the detector resolution leads to a net migration from lower p_T's to higher jet p_T's. This together with the iterative correction procedure in which the simulated hadron-level distribution is reweighted until the simulation at detector level is in agreement with data leads to an increase of this fluctuation.

ALPGEN gives a fair description for the slope of the trailing jet. The prediction underestimates the measured cross section by a factor of about ~ 1.2 to ~ 1.8. Similar to the leading jet PYTHIA predicts a softer p_T spectrum.

The measurement of the third leading jet shown in Figure 5.18 is limited by the statistics, but the jet p_T distribution appears to prefer a softer spectrum as predicted by ALPGEN.

Not included in the Figures are uncertainties due to the renormalisation and factorization scales on the predicted cross sections. These uncertainties have been studied in detail in Reference [58] for $Z/\gamma^* \rightarrow e^+e^-$ events. Changing the factorization scale and the renormalisation scale pairwise by a factor of 2 up and down from the nominal values leads to variations in the predicted cross sections of $\sim 20\%$ for the leading jet p_T, $\sim 30\%$ for the second leading jet p_T and $\sim 50\%$ for the third leading jet p_T.

A direct comparison to the prediction of fixed-order matrix-element calculations is not possible as these parton-level prediction need to be corrected to hadron level first. Furthermore, at low jet p_T leading logarithms from the perturbative expansion (which are not included in the fixed-order calculation) and non-perturbative effects (e.g. underlying event) are important and significantly change the p_T distribution.

Figures 5.23 and 5.28 show that ALPGEN and PYTHIA underestimate the jet rate at large jet multiplicities. But as the cross section is dominated at low jet p_T, the interpretation of the jet multiplicity distributions is less conclusive.

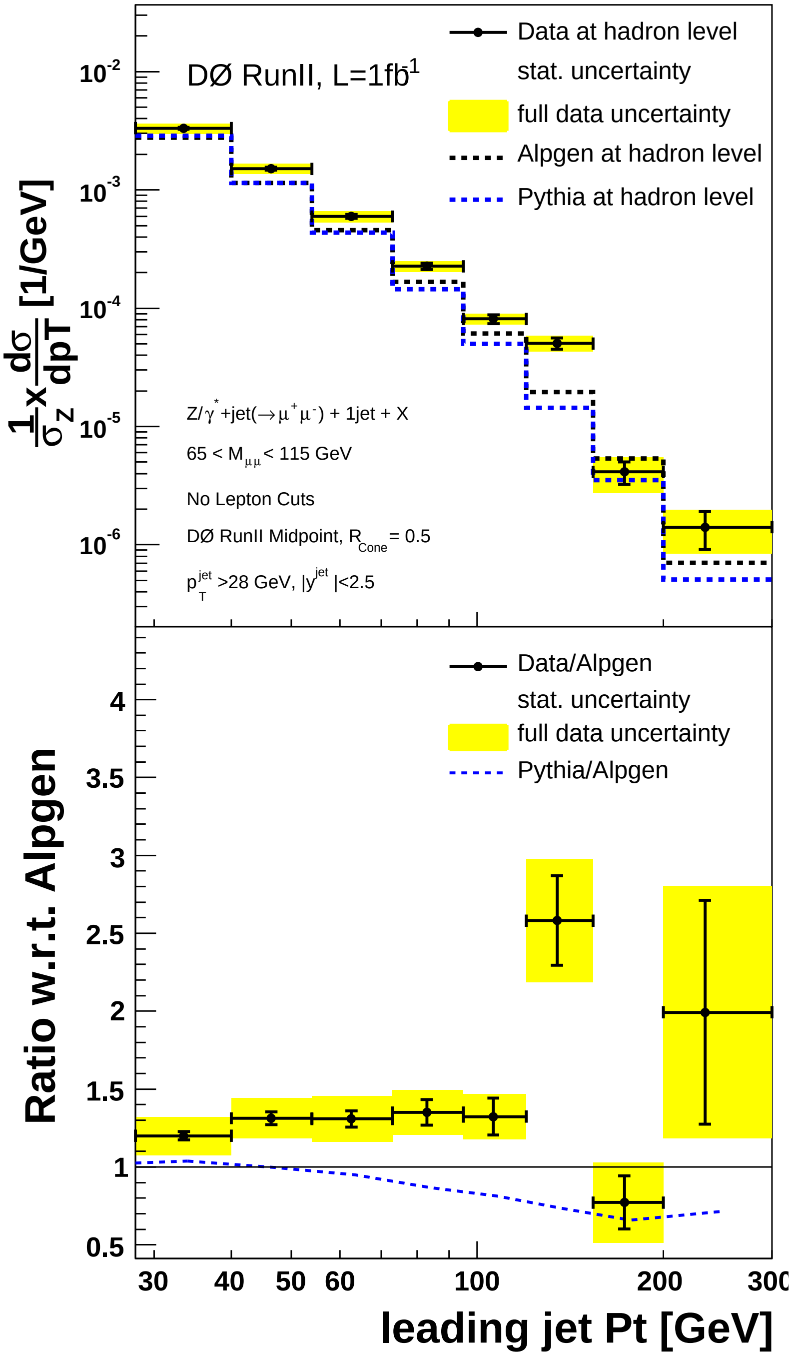

Figure 6.1: Differential cross section $\frac{1}{\sigma_Z}\frac{d\sigma}{dp_T}$ for the p_T of the leading jet in $Z+\geq$ 1jet events in data at hadron level compared with the predictions of Alpgen v2.05 and Pythia. The Alpgen MC is used as reference MC, data and the other MCs are shown relative to Alpgen (below).

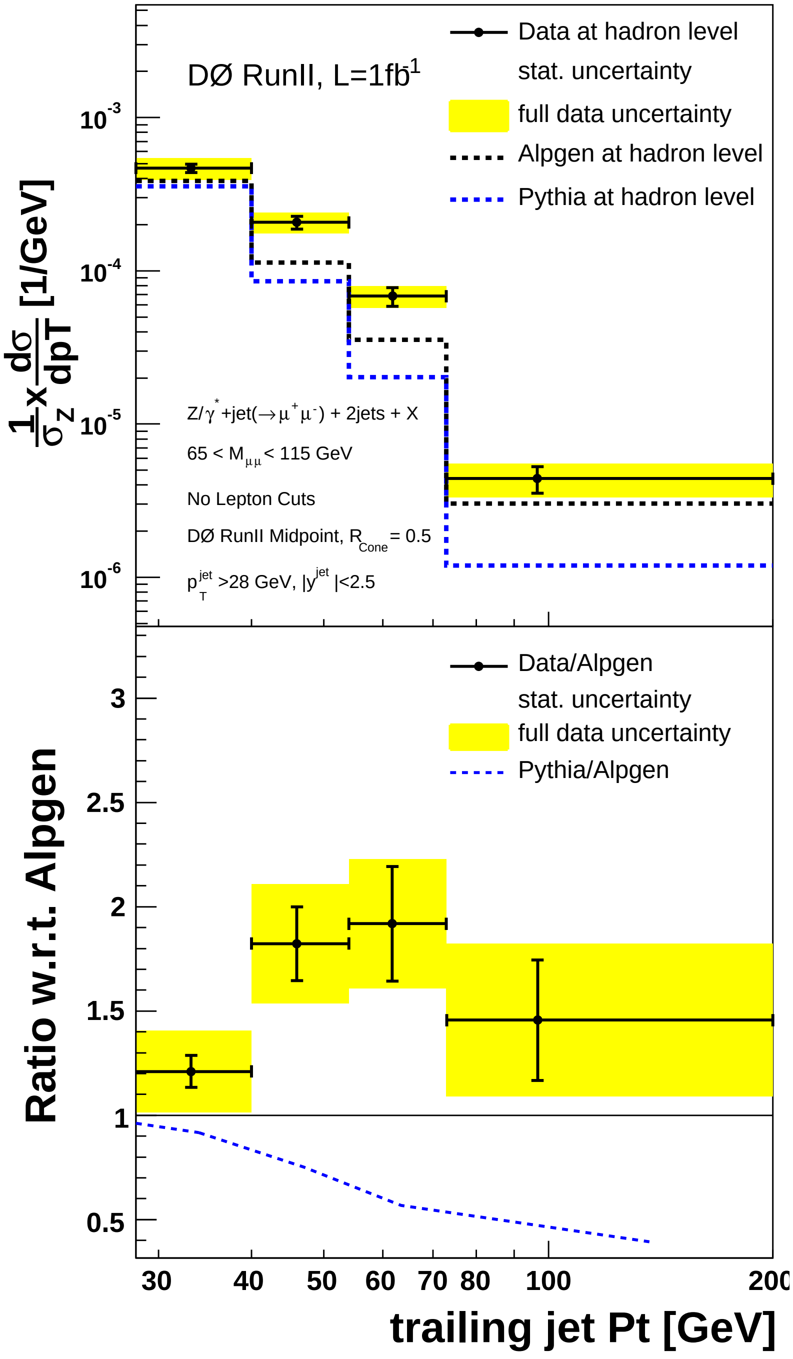

Figure 6.2: Differential cross section $\frac{1}{\sigma_Z}\frac{d\sigma}{dp_T}$ for the p_T of the trailing jet in $Z+ \geq$ 2jet events in data at hadron level compared with the predictions of Alpgen v2.05 and Pythia. The Alpgen MC is used as reference MC, data and the other MCs are shown relative to Alpgen (below).
]

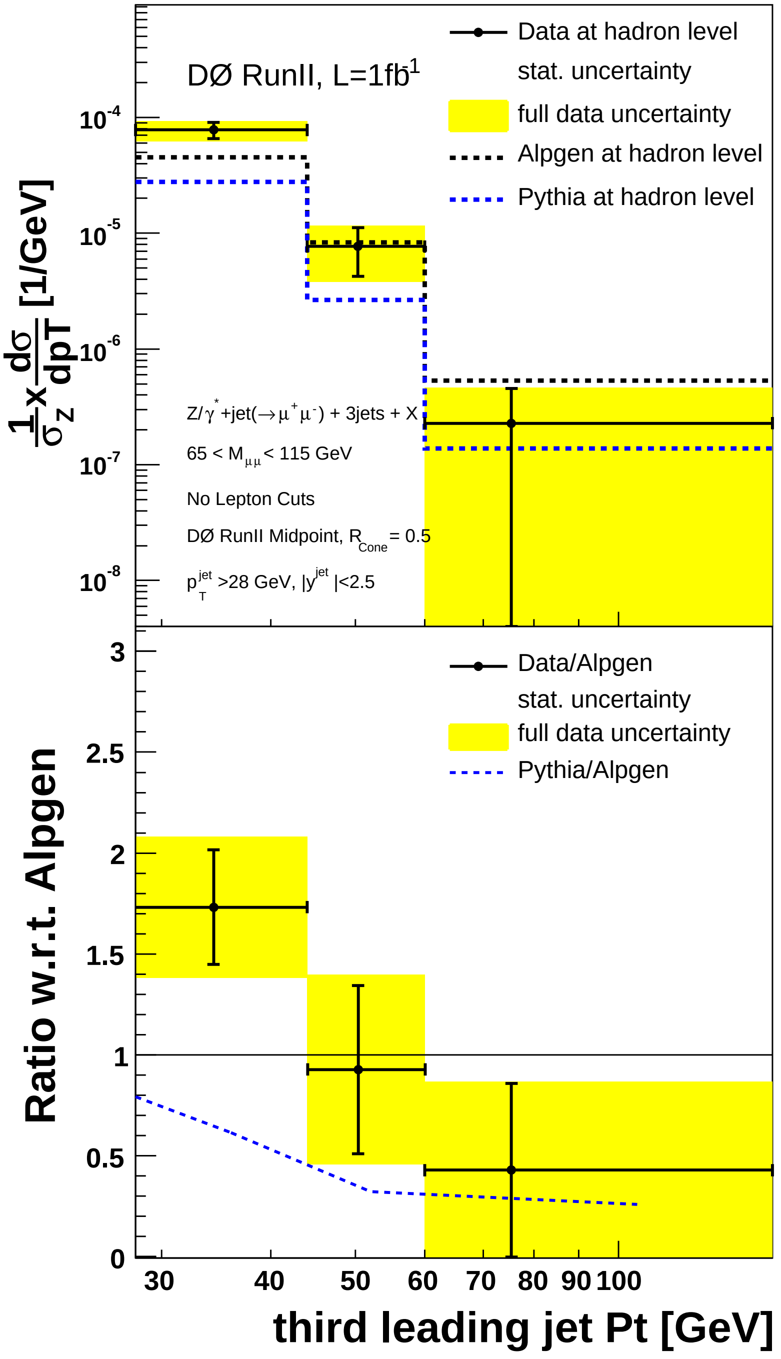

Figure 6.3: Differential cross section $\frac{1}{\sigma_Z}\frac{d\sigma}{dp_T}$ for the p_T of the third leading jet in $Z+\geq$ 3jet events in data at hadron level compared with the predictions of ALPGEN v2.05 and PYTHIA. The ALPGEN MC is used as reference MC, data and the other MCs are shown relative to ALPGEN (below).

$p_T(jet)$ $[GeV]$	mean p_T $[GeV]$	$\frac{1}{\sigma_{incl}} \frac{d\sigma}{dpT(jet)}$ $[1/GeV]$	err_{stat} [%]	err_{sys} [%]	$err_{jetalgo}$ [%]	err_{acc} [%]
28 - 40	33.5	$3.32e-03$	2.2	7.3	0.9	7.0
40 - 54	46.4	$1.51e-03$	3.1	5.3	0.4	7.7
54 - 73	62.6	$5.97e-04$	4.0	6.7	0.2	8.1
73 - 95	82.9	$2.26e-04$	6.0	4.9	0.2	7.3
95 - 120	106.2	$8.12e-05$	8.8	4.2	0.4	4.9
120 - 154	134.7	$5.04e-05$	10.9	10.6	0.4	0.2
154 - 200	173.0	$4.13e-06$	21.8	25.0	0.8	1.8
200 - 300	233.7	$1.41e-06$	35.4	18.4	0.5	3.4

Table 6.1: Measurement of $\frac{1}{\sigma_{incl}} \cdot \frac{d\sigma}{dpt_{jet}}$ for the leading jet in $Z+$ jet events. The result is normalised to the inclusive cross section. The errors given are relative errors.

$p_T(jet)$ $[GeV]$	mean p_T $[GeV]$	$\frac{1}{\sigma_{incl}} \frac{d\sigma}{dpT(jet)}$ $[1/GeV]$	err_{stat} [%]	err_{sys} [%]	$err_{jetalgo}$ [%]	err_{acc} [%]
28 - 40	33.2	$4.68e-04$	6.3	12.0	1.0	8.8
40 - 54	46.0	$2.07e-04$	9.6	10.6	1.2	6.2
54 - 73	61.8	$6.83e-05$	14.1	6.5	0	3.8
73 - 200	96.7	$4.41e-06$	19.6	14.1	0.4	6.5

Table 6.2: Measurement of $\frac{1}{\sigma_{incl}} \cdot \frac{d\sigma}{dpt_{jet}}$ for the second leading jet in $Z+$ jet events. The result is normalised to the inclusive cross section. The errors given are relative errors.

$p_T(jet)$ $[GeV]$	mean p_T $[GeV]$	$\frac{1}{\sigma_{incl}} \frac{d\sigma}{dpT(jet)}$ $[1/GeV]$	err_{stat} [%]	err_{sys} [%]	$err_{jetalgo}$ [%]	err_{acc} [%]
28 - 44	34.4	$7.81e-05$	16.2	9.7	3.0	6.7
44 - 60	50.3	$7.69e-06$	44.7	23.4	0.9	1.9
60 - 150	75.4	$2.28e-07$	100.0	13.1	11.1	15.2

Table 6.3: Measurement of $\frac{1}{\sigma_{incl}} \cdot \frac{d\sigma}{dpt_{jet}}$ for the third leading jet in $Z+$ jet events. The result is normalised to the inclusive cross section. The errors given are relative errors.

7 Summary and Conclusion

The study of the inclusive production of jets in association with a weak vector boson in proton-antiproton collisions provides a good opportunity to test perturbative quantum chromodynamics. Nowadays theoretical predictions at next-to-leading order are only available for jet multiplicities up to 2. Therefore the understanding of $Z/\gamma^* \to \mu^+\mu^- +$ jets final states from data is important since this signal is an important irreducible background in many searches for new physics. Studying these processes helps also to constrain a major background to many Standard Model signals, e.g. top pair and single top production, which is one of the main physics programs at the Tevatron.
Existent event generators rely on mixed leading-order matrix element calculations with parton showers, where the different programs use different internal parameters. Comparisons show that the relating uncertainties are significant and that different kinematics are predicted [59]. These uncertainties become more significant if one extrapolates the theoretical predictions to LHC energies. Data corrected for detector effects to hadron level which can be directly compared to the event generators can be used as input for the tuning of these generators at the Tevatron and LHC.

In this thesis production cross sections for the associated production of Z bosons with jets have been derived using $\mathcal{L} \approx 1\,\mathrm{fb}^{-1}$ of data collected by the DØ experiment in RunIIa. The decay of the Z bosons into pairs of muons and antimuons provides an efficient way to identify the final state with low background contamination. Differential cross sections as function of the transverse momentum of the first, second, and third leading jet in $Z/\gamma^* \to \mu^+\mu^- + n$ jets events with $n \geq 1$, 2, or 3, respectively, have been measured. In addition the $Z/\gamma^* \to \mu^+\mu^- + n$ jets production cross sections have been derived for jet multiplicities of 0 to 4. The measured cross sections have been corrected for acceptance and migration effects back to hadron level using an unfolding method which also accounts for the efficiency of the signal selection criteria. The cross sections have been corrected to hadron level for jets with $p_T > 28\,(20)\,\mathrm{GeV}$ and rapidity $|y| < 2.5$ using the `D0`RunIICone algorithm with a cone size of 0.5. An additional correction to match the alternative SISCone algorithm has been presented as well. The cross sections have been first derived with respect to the limited acceptance for the muons from the Z boson decay,

corresponding to $|\eta_\mu| < 1.7$ (and no requirement on muon p_T), and subsequently corrected to the full phase space of the Z boson.
The fully corrected cross sections with respect to the mentioned kinematic acceptance have been compared to the predictions of the ALPGEN and PYTHIA event generators. ALPGEN which uses a mixed leading-order matrix element calculation with parton showering gives a good description of the shapes of the data distributions for the leading p_T(jet) and a fair description for the second leading p_T(jet), but underestimates the rate by about a third. Comparisons to PYTHIA which is based on a Q^2 ordered parton shower model show that this event generator predicts a softer p_T spectrum which is disfavored by the data. The measurement of the third jet p_T distribution is limited by statistics but appears to prefer a softer spectrum as predicted by ALPGEN.

At present about twice of the integrated luminosity is available compared to this analysis. Furthermore an integrated luminosity of about $15\,\mathrm{fb}^{-1}$ is expected for entire RunII. This larger dataset will allow to reduce both statistical and systematic uncertainties that arise from limited statistics.
In addition the present analysis can be used for future studies at the LHC. $Z/\gamma^* \rightarrow \mu^+\mu^- +$ jets final states will be used to understand Standard Model processes as well as to search for phenomena beyond the Standard Model.

Bibliography

[1] UA1 Collaboration, G. Arnison *et al.*, *Experimental Observation of Lepton Pairs of Invariant Mass Around 95-GeV/c**2 at the CERN SPS Collider*, Phys. Lett. B **126**, (1983) 398.

[2] UA2 Collaboration, P. Bagnaia *et al.*, *Evidence for* $Z^0 \rightarrow e^+e^-$ *at the CERN anti-p p Collider*, Phys. Lett. B **129**, (1983) 130.

[3] J. Goldstone, A. Salam, S. Weinberg, *Broken Symmetries*, Phys. Rev. **127**, (1962) 965.

[4] The Particle Data Group (and references therein), K. Hagiwara *et al.*, *The Review of Particle Physics*, Phys. Rev. D **66** (2002) 010001.

[5] UA1 Collaboration, G. Arnison *et al.*, *Experimental Observation of Isolated Large Transverse Energy Electrons with Associated Missing Energy at s**(1/2) = 540-GeV*, Phys. Lett. B **122**, (1983) 103.

[6] UA2 Collaboration, P. Bagnaia *et al.*, Phys. Lett. B **122**, (1983) 476.

[7] D. Griffiths, *Intodruction to Elementary Particles* New York Wiley (1987).

[8] M. K. Gaillard, P. D. Grannis and F. J. Sciulli, *The Standard model of particle physics*, Rev. Mod. Phys. **71**, (1999) 96.

[9] R. Barate *et al.*, *Search for the Standard Model Higgs Boson at LEP*, Phys. Lett.**B565**, **61** (2003), [hep-ex/0306033].

[10] S. Drell, T. Yan, *Partons and their Applications at High-Energies*, Ann. Phys. **66**, (1971) 578.

[11] Yu. L. Dokshitzer, D. I. Dyakonov and S. I. Troyan, *Hard Processes in Quantum Chromodynamics*, Phys. Rept. **58** (1980) 269.

[12] J. C. Collins, D. E. Soper, Nucl. Phys. **B193**, (1981) 381; **B213**, (1983) 545E; J. C. Collins, D. E. Soper, G. Sterman, *ibid.* **B250**, (1985) 199.

[13] G. A. Ladinsky, C. -P. Yuan, *The Nonperturbative regime in QCD resummation for gauge boson production at hadron colliders*, Phys. Rev. D **50**, (1994) 4239.

[14] V. Barger and R. Phillips, *Collider Physics*, updated edition (Perseus Books, 1996).

[15] R. K. Ellis, W. J. Stirling and B. R. Webber *QCD and Collider Physics*, Cambridge Monographs on Particle Physics, Nuclear Physics and Cosmology: 8, Cambridge University Press (1996).

[16] A. Buijs, *A fragmentation model applied to exclusive final states in photon-photon collisions*, 1986, SLAC-PUB-4037.

[17] B.R. Webber, *Fragmentation and hadronization*, Theory Division, CERN, 1211 Geneva 23, Switzerland.

[18] T. Sjostrand *et al.*, *High-energy-physics event generation with PYTHIA 6.1*, A.D. Polosa, JHEP **07** 001 (2001), [hep-ph/0206293].

[19] M.L. Mangano, M. Moretti, F. Piccinini, R. Pittau and A.D. Polosa, JHEP **07** 001 (2001), [hep-ph/0206293].

[20] The CDF Collaboration, F. Abe *et al.*, *Observation of Top Quark Production in p anti-p Collisions with the Collider Detector at Fermilab*, Phys. Rev. Lett. **74** (1995) 2626.

[21] The DØ Collaboration, S. Abachi *et al.*, *Observation of the Top Quark*, Phys. Rev. Lett. **74** (1995) 2632.

[22] G. Jackson (editor), *The Fermilab Recycler Ring Technical Design Report*, Technical Design Report, FERMILAB-TM-1991;
J. Thompson, *Introduction to Colliding Beams at Fermilab*, FERMILAB-TM-1909 (1994).

[23] The DØ Collaboration, S. Abachi *et al.*, *The DØ Upgrade: The Detector and its Physics*, Fermilab Pub-96/357-E (1996).

[24] J. Kotcher, *Design, Performance and Upgrade of the DØ Calorimeter* FERMILAB-Conf-95/007-E, (1995).

[25] T. Diehl *et al*, *Technical Design of the Central Muon System*, DØ Note 3365, (1998).

[26] P. Calfayan, *Oring single muon triggers in p17 data*, DØ Note **3925** (unpublished) (2008).

[27] D. Lincoln, *New Technologies in the DØ Central Tracker Upgrade* FERMILAB-Conf-96/137, VIth International Conference of Nuclear Physics on Instrumentation for Experiments at e^+e^- Colliders, Budker Institute of Nuclear Physics, Novosibirsk, Russia (March 1996).

[28] The DØ Collaboration, *The DØ Silicon Tracker Technical Design Report*, DØ Note **2169**, `http://d0server1.fnal.gov/projects/silicon/www/tdr_final.ps` (1994).

[29] D. Adams *et al* *The D0 Upgrade: Central Fiber Tracker, Technical Design Report*, DØ Note **4164**, (unpublished) (2003).

[30] L. Groer, *DØ Calorimeter Upgrades for the TeVatron Run II*, IXth International Conference on Calorimetry in Particle Physics, Annecy, France, (Oct 9-14, 2000).

[31] S. Hagopian, *The Run 2 DØ Muon System at the Fermilab TeVatron*, 7th International Conference on Advanced Technology and Particle Physics, Como, Italy, submitted to World Scientific (2002).

[32] The DØ Collaboration, S. Abachi *et al.*, *The DØ Upgrade: Forward Preshower, Muon System and Level 2 Trigger*, Fermilab-FN-641 DØ(1996).

[33] J. Butler, *Local Muon Momentum Resolution*, DØ Note **4002** (unpublished) (2002).

[34] R. Brun, *GEANT 3 Users Guide*, Technical Report CERN/DD/EE/84-1, CERN (1984);
The DØ Collaboration, *D0GSTAR - DØ GEANT Simulation of the Total Apparatus Response*, internes DØ Dokument, derzeit zu finden unter `http://www-d0.fnal.gov/computing/MonteCarlo/simulation/d0gstar.html` (2001).

[35] G. Grenier, *Z mass reweighting for Alpgen p17 production*, DØ Note **5410**, (unpublished) (2007).

[36] Muon-ID certification v3.0 `http://www-d0.fnal.gov/phys_id/muon_id/d0_private/muon_id.html`.

[37] M. Arthaud, F. Deliot, B. Tuchming, V. Sharvy and D. Vilnova, *Muon momentum oversmearing for p17 data*, DØ Note **5444** (unpublished) (2007).

[38] G. C. Blazey *et al.*, *Run II jet physics*, [hep-ex/0005012].

[39] A. Harel, *Jet Id Optimization*, DØ Note **4919**, (unpublished) (2005).

[40] JES Group, *p17 Jet Energy Scale*, DØ Note **5382**, (unpublished) (2007).

[41] Offline Run Quality Database
`http://d0db.fnal.gov/qualitygrabber/qualQueries.html`.

[42] Common sample group - What Data to use for Analysis
`http://www-d0.fnal.gov/Run2Physics/cs/index.html`
`http://www-d0.fnal.gov/Run2Physics/cs/skimming/fixPass2p170903.html`.

[43] Luminosity-ID, *How to lumi*,
`http://plone4.fnal.gov/P1/D0Wiki/physics/top/howto-lumi`.

[44] J. D. Hobbs, T. Nunnemann, R. Van Kooten *Study of pp(bar)→ Y/gam* →ee and mumu event yields as a luminosity cross check*, DØ Note **5268**, (unpublished) (2006).

[45] T. Nunnemann, *NNLO Cross-Sections for Drell-Yan, Z and W Production using Modern Parton Distribution Functions*, DØ Note **4476**, (unpublished) (2004).

[46] R. Akers *et al.* [OPAL Collaboration], *QCD studies using a cone based jet finding algorithm for e+ e- collisions at LEP*, Z. Phys. C **63** (1994) 197.

[47] G.P. Salam and G. Soyez, *A practical Seedless Infrared-Safe Cone jet algorithm*, JHEP **07** 086 (2007), [arXiv:0704.0292 [hep-ph]].

[48] G. Grenier, *Z mass Reweighting for* ALPGEN *p17 production*, DØ Note **5410**, (unpublished) (2007).

[49] N. Makovec and J.-F. Grivaz, *Shifting, Smearing and Removing Simulated Jets*, DØ Note **4914** (unpublished) (2005).

[50] B. Casey *et al.*, *The updated DØ Luminosity Determination*, DØ Note **4328**, (unpublished), (2004).

[51] V. Blobel und E. Lohrmann, *Statistische und numerische Methoden der Datenanalyse* Stuttgart, Teubner (1998).

[52] V. Blobel, *The RUN manual, Regularized Unfolding for High-Energy Physics Experiments*, OPAL Technical Note TN361 (1996).

[53] G. Lafferty, T. Wyatt *Treatment of Measurements Within Wide Bins* Nucl. Instrum. Meth. A **355**, 541, (1995).

[54] G. Hesketh, *A Measurement of the Z^0 Boson Production Cross Section Times Muon Branching Fraction in $p\bar{p}$ Collisions at 1.96 TeV*, Ph. D. thesis, University of Manchester, (2003).

[55] Luminosity-ID, *Accessing Luminosity Information*, `http://www-d0.fnal.gov/phys_id/luminosity/data_access/`.

[56] F. James, *MINUIT-Function Minimization and Error Analysis* CERN Program Library entry **D506**, (1994-1998).

[57] G. Blazey *et al.*, *Run II Jet Physics*, DØ Note **3750**, (unpublished) (2000).

[58] H. Nilsen, *$Z/\gamma^*(\rightarrow ee)+$ Jets-Measuring $\frac{d\sigma}{dp_T(Jet)}$ for the three Leading Jets*, DØ Note, (unpublished), (2008).

[59] S. Hoeche *et al.*, *Matching Parton Showers and Matrix Elements*, (2006), [hep-ph/0602031].

Danke

Ich möchte allen danken, die mich bei der Anfertigung dieser Arbeit unterstützt haben.

Ich danke Prof. Dr. Dorothee Schaile, die mir diese Arbeit ermöglicht und mich immer wieder dabei unterstützt hat. Ich danke Thomas Nunnemann, der sie betreut und vorangetrieben hat und den ich immer wieder mit meinen Fragen löchern konnte. Ich möchte Prof. Dr. Otmar Biebel für die Klärung vieler Fragen das Graduiertenkolleg betreffend danken. Danke an Raimund Ströhmer, der mir viele Dinge anschaulich erklärt hat, an Johannes Elmsheuser, den ich immer mal wieder stören durfte und danke an viele andere des Lehrstuhles Schaile.

Nicht vergessen möchte ich Philippe, Alexander, Meta, Marion und Frau Franz.

Ganz besonders danke ich meinen Geschwistern, Eltern und Schwiegereltern, die mir den Freiraum für diese Arbeit geschaffen haben und natürlich Konstantin, Helena, Sophia und Max.